# Experimental studies of the non-equilibrium dynamics and complex flows in dense suspensions

A thesis submitted for the degree of

***Doctor of Philosophy***

in the

Jawaharlal Nehru University

*by*

*Palak*



Soft Condensed Matter Group
Raman Research Institute
Bangalore, INDIA

October 2022

© Palak, 2022.

*Dedicated to*

My Parents

# Certificate

This is to certify that the work contained in the thesis entitled **''Experimental studies of the non-equilibrium dynamics and complex flows in dense suspensions''**, submitted by **Palak** (Enrollment No.-RRI/2016/012) to **Jawaharlal Nehru University** for the award of the degree of **Doctor of Philosophy** in Physical Sciences, is the bonafide record of original research work carried out by the candidate from July 2016 - October 2022, under my guidance and supervision at **Raman Research Institute (RRI)**, Bengaluru, India. The results embodied in the thesis have not been submitted to any other University or Institute for the award of any degree or diploma.

**Prof. Tarun Souradeep**
Director
Raman Research Institute
Bengaluru-560080, India

**Prof. Ranjini Bandyopadhyay**
(Thesis Supervisor)

# Declaration

I hereby declare that the work presented in this thesis titled **''Experimental studies of the non-equilibrium dynamics and complex flows in dense suspensions''** is completely original. This research work is carried out under the supervision of **Prof. Ranjini Bandyopadhyay** at **Raman Research Institute, Bengaluru, India**. This dissertation is the result of my own work unless otherwise stated. No part of this thesis has been submitted elsewhere for the award of any degree, diploma, membership, fellowship or any other similar title of any university or institution. I also declare that this thesis has been passed through the **Turnitin** software to check for plagiarism.

**Prof. Ranjini Bandyopadhyay**
(Thesis Supervisor)
Soft Condensed Matter Group
Raman Research Institute
Bengaluru-560080, India
Date:
Place:

**Palak**
(Student's name)

# Acknowledgements

I express my sincere gratitude to my thesis supervisor Prof. Ranjini Bandyopadhyay for her guidance, support and encouragement throughout my thesis work. Prof. Ranjini has been an ideal mentor, offering advice and encouragement with a perfect blend of insight and humor. I am grateful to her for believing in me, encouraging independent thinking and guiding me the different phases of my journey here. I would like to convey many thanks to my advisory committee members, Prof. V. A. Raghunathan (RRI) and Dr. Sayantan Majumdar (RRI), for useful discussions, valuable suggestions and help with many academic issues. I am thankful to Prof. Yashodhan Hatwalne, Prof. Pramod A Pullarkat, Dr. Gautam Vivek Soni, Prof. Arun Roy and other faculty members of Soft Condensed Matter Group for teaching me during my coursework and their constant encouragement. I would like to especially thank my collaborators, Dr. Sreeram K. Kalpathy (IIT Madras), Rahul Sathyanath (IIT Madras), Dr. Debasish Saha (Dusseldorf), Vaibhav Raj Singh Parmar (RRI) and Anson Thambi (RRI). It was a wonderful experience working with them and I look forward to potential collaborations in the future also.

My sincerest thanks and regards to my seniors Dr. Paramesh Gadige, Dr. Sanjay and Dr. A. W. Zaibudeen, for helping me on countless occasions, with experiments and useful discussions. I would like to convey many thanks to my labmates Chandeshwar, Rajkumar, Vaibhav, Yogesh, Anson, Sonali, Jasim, and Sayantan for their help with experiments and useful discussions. I want to thank my past labmates Riddhika, Tonmoy, Ganesh, Venketesh, and Vipin for their company in RRI. I want to take a moment to express my heartfelt gratitude to Arsalan for helping me out

with coding of the image analysis done for Chapter 3 in this thesis. I express my sincere gratitude to Mr. Yatheendran K. M. for his help with SEM, cryo-SEM imaging and for teaching me confocal microscope. I would like to thank Mr. Mani for his help with the experimental setup. Many thanks to all members of RRI workshop for their help and support.

I express my gratitude to the director, Prof. Tarun Souradeep, for his help regarding various academic issues. I would like to thank the administrative officer, Mr. Naresh V. S., for his assistance with countless administrative issues. I express my sincere gratitude to the administration department, especially Mrs. Shailaja, Mrs. Marisa, Mrs. K. Radha, Mrs. Vidya, Mrs. Harini Kumari S and all other staff members of the administration for their help and support. I would like to express my gratitude to Mr. K. Radhakrishna for his assistance in many official things in the early years of my Ph.D. I would like to extend my thanks to SCM group secretary Mrs. Chaithanya M. S. for her help with purchasing chemicals and laboratory components, arranging transport, travel claims and support. My sincere thanks to Raja and Murali for their help on a daily basis.

I want to thank all the library staff members for their help and support. I am thankful to all staff members in the purchase and account departments for their help with purchasing laboratory equipment, travel claims and foreign exchange. I would like to thank all the staff members of the computer section for their time-to-time assistance in resolving countless issues regarding software installation and internet connectivity. I would like to thank Uma ji, Sharada ji, Padma ji, Munirathna ji, Mangala ji and Rekha ji for providing me with good food in the hostel canteen. I acknowledge all the canteen staff members, hostel staff members, and everyone at RRI for their cooperation and encouragement.

I am thankful to every student at RRI for their encouraging company, entertainment, support and discussions on various academic and nonacademic topics. A special note of thanks to my best friend, Miss Pooja Setia, for always being there. I would like to thank my batchmates Chandeshwar, Anand, Arsalan, Vishnu, Ra-

jkumar, Ashish, Dipak, Ranita, Swarnak, Sanchari, Rishab, Bapan, Pradosh, Avik, Saikat and Abhishek for providing me amicable environment in RRI. A special note of thanks to Raj Prince, Anand, Chandehswar, Saurabh, Sukhveer, Nancy, Nomaan, Arsalan, Vishnu, Sebanti, Sanhita, Varun, Rajkumar, Hari, Adwaith, Vipin, Vaibhav, Manish, Rupak, Shashank, Kinjal, Mukesh for being amazing friends during my stay and doing fun activities like watching movies, playing carom, cooking, birthday parties, celebrating festivals, etc. I would like to thank my seniors Raj Prince, Nomaan, Sushil, Irla, Nancy, Sreeja, Anindya, Meera, Anna, Janki, Nazma, Niranjan, Anirudh, Priyanka for their valuable suggestions and discussions. I am thankful to Sachi, Abhishek, Makarant, Alka, Vani, Vasudha, Serene, Gunjan, Manami, Pooja, Deepak, Saumya, Mari, etc, for the discussions over tea and lunch.

Last but not the least, I express my deepest gratitude, love and respect for my grandparents, Late Sh. Mahender Pal (Baba ji) and Smt. Darshana Devi (Badi mumma); Late Sh. Ved Prakash Gupta (Nana ji) and Late Smt. Vidya Devi (Nani ji) and my lovely parents, Sh. Sanjay Chaudhary and Smt. Asha Rani; my brother Pranav; the love of my life Kushal Goyal and other family members for their constant support, motivation and help in every ups and downs in my life.

# Synopsis

Dense colloidal suspensions show complex flow behavior such as shear-thinning, shear thickening and thixotropy. These suspensions exhibit distinct phases depending on the colloidal volume fraction, interparticle electrostatic interactions and temperature. This thesis studies the non-equilibrium flows of soft materials under confinement and in the presence of activity. When a less viscous fluid displaces a more viscous fluid, the fluid-fluid interface becomes unstable, resulting in complex interfacial patterns known as viscous fingers. In this thesis, we investigate the onset and development of instabilities at the interface between colloidal suspensions and Newtonian fluids in confined geometries. We report that the shear-dependent viscosities and aging dynamics of colloidal suspensions strongly affect the interfacial dynamics. We also study changes in the dynamics of dense passive colloids in the presence of active particles.

Chapter 1 discusses the background information needed to understand the thesis work. This chapter includes an overview of different colloidal systems, interparticle interactions in the context of colloidal suspensions, and the dynamics of chemically active particles. The flow behavior of dense cornstarch suspensions is described. This is followed by a discussion on the aging dynamics and phase behavior of aging suspensions of colloidal Laponite clay particles. The dynamics of interfaces involving different fluid pairs are discussed in detail. This chapter concludes with a brief discussion on the colloidal glass transition and the effects of activity on the dynamics of dense colloidal suspensions.

Chapter 2 describes sample preparation protocols and experimental techniques

employed in this thesis. The experimental techniques employed in our studies: rheological measurements, imaging using a DSLR camera, bright field microscope and confocal microscopy, are discussed. The design of our custom-made radial Hele-Shaw cell setup is described.

Chapter 3 describes the dynamics at the interface of a Newtonian fluid (glycerol-water mixtures of different viscosities, displacing fluid) and a shear-thinning viscoelastic fluid (aqueous cornstarch suspensions of varying concentrations, displaced fluid) in a radial Hele-Shaw cell geometry. With increasing viscosity ratio of the fluid pair, a transition from radial branching patterns to more stable interfaces, displaying finger coalescence and proportionate growth features, is reported. This research indicates that increasing the viscosity of the displacing fluid and the concentration-dependent elasticity of the outer viscoelastic fluid can significantly suppress interfacial instabilities. Linear stability analysis of the interface, using the viscosity ratio as the only control parameter, is employed to estimate the dominant wavelength of interfacial perturbations. The experimentally determined spacing between fingers at the onset of interfacial instability agrees well with the perturbation wavelength predicted numerically.

In chapter 4, we investigate the displacement of a shear thickening aqueous cornstarch suspension by a Newtonian fluid (water). The Hele-Shaw cell used in this study is identical to the one used in the studies reported in chapter 3. We study the growth kinetics of the emergent interfacial patterns that result from the radial displacement of aqueous cornstarch suspensions by water at various flow rates. The shear rates exerted by water while displacing the cornstarch suspensions are in the shear thickening regime of the rheological flow curves of the dense cornstarch suspensions. Water not only displaces the cornstarch suspension but also pulls it inwards at high flow rates, resulting in the formation of reverse fingers at the outermost cornstarch suspension-air interface. The reverse fingering phenomenon is understood in terms of the normal stresses in the colloidal cornstarch suspension generated at the high experimental shear rates. Reverse finger formation is substantially enhanced

by increasing the concentration-dependent elasticity of the cornstarch suspension.

In chapter 5, we report the emergence of a wide range of interfacial patterns in miscible and immiscible displacements of aqueous suspensions of a soft glassy colloidal Laponite clay by a Newtonian fluid in a quasi-two-dimensional radial Hele-Shaw cell. We report the emergence of distinct interfacial patterns due to the combined effects of the spontaneous aging of a displaced Laponite suspension and its shear-thinning due to injection of the displacing Newtonian fluid at high driving pressures. We observe three different morphologies: dense viscous patterns (DVP), dendritic patterns (DP) and viscoelastic fractures (VEF) during the miscible displacement of aqueous Laponite suspensions of different ages (or different waiting times since loading in the Hele-Shaw cell) by water. In contrast, immiscible displacements of Laponite suspension with mineral oil lead to a transition from flower patterns (FP) to jagged patterns (JP). We distinguish each pattern morphology by its areal ratio: the area of the fully developed pattern normalized by the area of the smallest circle enclosing it. We summarize our observations in a three-dimensional non-equilibrium phase diagram with the waiting time of the displaced fluid, flow rate of the displacing fluid and interfacial tension as the three axes.

Chapter 6 reports the temporal growth of the large-scale fingering patterns reported in chapter 5. All the distinct morphologies appear to have distinct growth kinetics. The evolution of the interfacial patterns is examined by calculating the pattern perimeters and the propagation velocities of the longest finger-tips. While the finger-tip velocity for dense viscous patterns (DVP) does not change with time, dendritic patterns (DP) and viscoelastic fractures (VEF) initially grow fast, followed by slow growths at later times. On the other hand, the tip velocity of immiscible displacement patterns decreases with time, displaying stick-slip motion. Because of their different growth mechanisms, we can segregate the distinct morphologies by computing their perimeter lengths.

In chapter 7, we explore the influence of activity in dense binary mixtures of passive particles. We synthesize chemically active Janus particles by coating one half

of polystyrene (PS) microspheres with platinum. Platinum serves as a catalyst when these particles are dispersed in hydrogen peroxide ($H_2O_2$) solution, decomposing $H_2O_2$ molecules into water and oxygen. The asymmetric distribution of reaction products around particles results in the propulsion of particles by the process of self-diffusiophoresis. By video tracking the particles with a confocal microscope, we analyze passive particle dynamics in the presence of small quantities of active particles by computing the particle mean square displacements with time.

Chapter 8 summarizes the main results of this thesis and briefly discusses the scope for future work.

Prof. Ranjini Bandyopadhyay
(Thesis Supervisor)
Soft Condensed Matter Group
Raman Research Institute
Bangalore 560080 INDIA

Palak
(Student's name)

# List of Publications

1. Emergent patterns and stable interfaces during radial displacement of a viscoelastic fluid

   **Palak**, Rahul Sathyanath, Sreeram K. Kalpathy and Ranjini Bandyopadhyay, *Colloids and Surfaces A*, **629**, 127405, 2021, DOI: https://doi.org/10.1016/j.colsurfa.2021.127405.

2. Pattern selection in radial displacements of a confined aging viscoelastic fluid

   **Palak**, Vaibhav Raj Singh Parmar, Debasish Saha and Ranjini Bandyopadhyay, *JCIS Open*, **6**, 100047, 2022, DOI: https://doi.org/10.1016/j.jciso.2022.100047.

3. Emergence of transient reverse fingers during radial displacement of a shear-thickening fluid

   **Palak**, Vaibhav Raj Singh Parmar, Sayantan Chanda and Ranjini Bandyopadhyay. *Colloids and Surfaces A*, **662**, 130926, 2023, DOI: https://doi.org/10.1016/j.colsurfa.2023.130926. (Updated after submission in October 2022)

4. Growth kinetics of interfacial patterns formed by the radial displacement of an aging viscoelastic suspension

   **Palak**, Vaibhav Raj Singh Parmar and Ranjini Bandyopadhyay, *JCIS Open*, **10**, 100084, 2023, DOI: https://doi.org/10.1016/j.jciso.2023.100084. (Updated after submission in October 2022)

# Contents

**Acknowledgements** **vi**

**Synopsis** **ix**

**Publications** **xiii**

**1 Introduction** **1**

1.1 Granular suspensions . . . . . 1

1.2 Flow regimes of aqueous cornstarch suspensions . . . . . 2

1.3 Colloidal suspensions . . . . . 3

1.4 Inter-particle interactions in colloids . . . . . 4

1.5 Colloidal glass transition . . . . . 7

1.6 Aqueous Laponite suspensions . . . . . 9

1.7 Janus particles . . . . . 11

1.8 Interfacial instabilities . . . . . 12

1.8.1 Instabilities at the interface between two Newtonian fluids . . 13

1.8.2 Instabilities at the interface between Newtonian and non-Newtonian fluids . . . . . 14

1.9 Effect of active particles on a crowded environment of passive particles 16

1.10 Thesis organization . . . . . 17

**2 Materials and Methods** **34**

2.1 Introduction . . . . . 34

2.2 Sample preparation . . . 35
2.2.1 Cornstarch suspensions . . . 35
2.2.2 Laponite® suspensions . . . 35
2.2.3 Synthesis of chemically active Janus particles . . . 35
2.2.4 Binary mixture of passive polystyrene particles . . . 37
2.2.5 Binary mixture of active and passive polystyrene particles . . . 38
2.3 Experimental techniques . . . 39
2.3.1 Rheology . . . 39
2.3.2 Hele-Shaw Cell . . . 44
2.3.3 Bright field microscope . . . 46
2.3.4 Confocal microscope . . . 47

**3 Emergent patterns and stable interfaces during radial displacement of a viscoelastic fluid 53**
3.1 Introduction . . . 53
3.2 Sample preparation and experimental methods . . . 54
3.2.1 Image processing and calculation of sweep efficiencies . . . 56
3.3 Results and Discussion . . . 57
3.3.1 Rheological characterization of dense cornstarch suspensions . . . 57
3.3.2 Interfacial pattern morphologies and their dependence on viscosity ratio . . . 60
3.3.3 Coalescence events at the interface . . . 64
3.3.4 Role of elasticity of the cornstarch suspension on interfacial roughness and sweep efficiency . . . 67
3.3.5 Spacing between fingers: Theoretical estimate vs. experimental measurements . . . 68
3.4 Conclusions . . . 73

**4 Evolution of reverse fingers during radial displacement of a shear-thickening fluid 81**

4.1 Introduction . . . 81
4.2 Materials and Methods . . . 84
4.2.1 Calculations . . . 86
4.3 Results & Discussions . . . 88
4.4 Conclusions . . . 97

**5 Pattern selection in radial displacements of a confined aging viscoelastic fluid 107**
5.1 Introduction . . . 107
5.2 Materials and Methods . . . 110
5.3 Results and Discussion . . . 112
5.3.1 Aging time of the displaced suspension determines interfacial pattern morphology . . . 112
5.3.2 Pattern morphology can be tuned by controlling the shear-thinning rheology of the displaced suspension . . . 118
5.4 Conclusions . . . 122

**6 Growth kinetics of interfacial patterns formed by the radial displacement of an aging viscoelastic suspension 131**
6.1 Introduction . . . 131
6.2 Materials and Methods . . . 133
6.3 Results and Discussion . . . 133
6.4 Conclusions . . . 144

**7 Effects of activity on the dynamics of dense binary mixtures of passive particles 150**
7.1 Introduction . . . 150
7.2 Sample preparation and experimental methods . . . 151
7.3 Results and discussions . . . 153
7.4 Conclusions . . . 157

**8 Summary and future directions 162**

# Chapter 1

# Introduction

Soft condensed matter [1, 2] comprises the broad class of materials which are neither liquids nor crystalline solids and includes colloidal suspensions, polymer melts, liquid crystals, self-assembling amphiphilic molecules and biological materials such as membranes, vesicles, etc. Soft materials have a range of applications, as structural and packaging materials, as detergents, glue, paints and most edible food items, etc. These materials are viscoelastic, showing both solid and liquid-like behavior at laboratory timescales. Due to weak interactions between the constituent particles, they can be easily deformed under small applied strains or stresses.

## 1.1 Granular suspensions

Suspensions of granular particles such as sand and sugar that are of sufficiently large sizes (diameters between 10 $\mu$m and 100 $\mu$m) are non-Brownian in nature [3, 4]. Despite their ubiquity in daily lives, these materials still fascinate researchers. Granular media are athermal systems due to their large sizes [5, 6]. For example, if one considers a glass bead of diameter $d_p = 1$ mm and density $\rho_p$ =2500 kgm$^{-3}$ at room temperature, $T = 300$ K, and under acceleration due to gravity, g = 9.8 m s$^{-2}$, the gravitational energy ($E_p \sim mgd = 10^{-10}$ J) is much larger when compared to the thermal energy ($E_{th} \sim k_B T = 4.0 \times 10^{-21}$ J, where $k_B = 1.38 \times 10^{-23}$ J K$^{-1}$ is

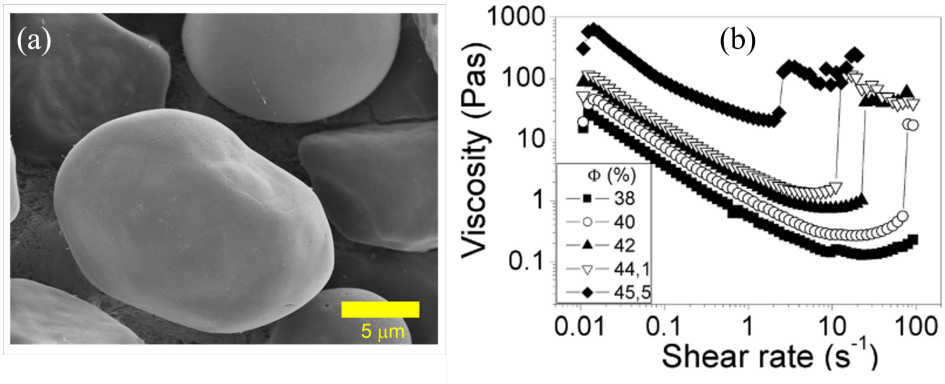



**Fig. 1.1:** (a) Cryogenic scanning electron microscopy (Cryo-SEM) image of anisotropic and irregularly shaped cornstarch particles. (b) Viscosity vs. shear rate for aqueous cornstarch suspensions of different concentrations. This figure is reproduced from [7], with permission of AIP Publishing.

the Boltzmann constant [4]). While granules in dry granular media solely interact via direct contact interactions, both hydrodynamics and contact interactions are present in dense granular suspensions. In this thesis, dense granular suspensions of cornstarch particles (Fig. 1.1(a)) of average diameter $\sim$ 15 $\mu$m, exhibiting a discontinuous transition between fluid-like behavior at a low shear rate and solid-like behavior at a high shear rate, are used.

## 1.2 Flow regimes of aqueous cornstarch suspensions

A dense suspension of polydisperse non-Brownian cornstarch particles exhibits shear-thinning and shear-thickening properties depending on the applied shear stress [8] and particle volume fraction [9]. An aqueous cornstarch suspension subjected to low shear rates exhibits shear-thinning behavior wherein viscosity of the system decreases with applied shear rates. The shear-thinning behavior can be attributed to several factors, such as the organization of suspended particles along the flow, a constant hydrodynamic viscosity contribution due to viscous stresses and an entropic contribution from random particle collisions [7, 9–11]. As the shear rate is increased,

a dense cornstarch suspension shows a continuous shear-thickening (CST) regime followed by a discontinuous shear-thickening (DST) regime [7, 12] (Fig. 1.1(b)). At even higher imposed shear stresses, dense cornstarch suspensions display a shear jamming (SJ) state in which the suspension no longer flows but instead behaves like a solid [8]. The increase in the bulk viscosity of the medium in the ST regime is attributed to the hydrodynamic [9, 13] and frictional [14, 15] interactions between particles. The CST regime is characterized by well-defined high stress dynamic regions which propagate in the shearing direction and span a progressively larger fraction of the entire system as the applied stress is increased [16]. Recent simulations [17] of dense suspensions have shown that inter-particle connectivity due to the formation of force networks determines the rheological response of the suspension. It was reported that the DST regime has more constrained force networks connected via multiple particle contacts having rolling motion when compared to the CST regime with less constrained force networks having single particle-particle contacts. The number density of these frictional contacts increases with increasing shear rates until the SJ state is reached [8].

## 1.3 Colloidal suspensions

Colloidal suspensions are heterogeneous multiphase systems comprising solid, liquid and gaseous particles dispersed in a continuous medium such as liquid, gas or solid [18]. The dispersed particles are significantly larger than the molecules of the suspending medium in the colloidal suspension. The word “colloid” was coined from a Greek word- ”$\kappa\omega\lambda\lambda\alpha$” by Graham Thomas which means “glue” [19, 20]. The thermal energy of a dilute suspension of colloidal particles is of the order of $k_BT$ and the time taken by the particle to diffuse a distance equal to its radius is given by $\tau_D = a^2/D = 6\pi\eta a^3/k_BT$ using Stokes-Einstein relation [21], where $a$ is the radius of the particle, $D$ is the translational diffusion coefficient, $\eta$ is the viscosity of the medium and $T$ is the temperature. The size of the suspended particles is

sufficiently small and varies from nm to m such that the effect of the thermal energy becomes increasingly significant, leading to more pronounced thermal fluctuations such that the diffusive particle flux balances the particle gravitation flux. Owing to the small size of the colloidal particles, the ratio of surface area and volume is very large, which gives rise to complex bulk properties of the colloidal suspensions. Due to thermal fluctuations in the colloidal suspensions, individual colloidal particles undergo Brownian motion. $\tau_D$ is of the order of ms-$\mu$s and allows experimental studies of the dynamics of these particles using tools available in the laboratory. In colloidal suspensions, a balance between the diffusive flux of suspended particles due to thermal fluctuations and particle sedimentation determines suspension stability [18].

## 1.4 Inter-particle interactions in colloids

Depending on the particle nature and suspending medium, suspensions of charged colloidal particles exhibit various interactions *viz.* short-range van der Waals attractions and long-range screened Coulombic repulsion. Both the interactions are described by the DLVO theory developed by Derjaguin, Landau, Verwey and Overbeek [22, 23]. These interactions are described below:

### van der Waals attractions

van der Waals interactions are attractive forces acting between atoms, molecules and surfaces [24]. Van der Waals interactions are weak intermolecular interactions that exist between atoms, molecules, or particles. These forces arise due to temporary or induced fluctuations in electron distributions, leading to attractive or repulsive interactions between the entities involved. The temporal fluctuations in electron distribution result in instantaneous dipoles in one particle inducing dipoles in the other particle [18, 25]. These induced dipoles create an attractive inter-particle force. Such attractive interactions are known as London dispersive interactions and arise

due to the coupling between the induced dipoles to minimize the interaction energy. In case of polar molecules having permanent dipole moments, the particle can attract or repel the other particle depending on the orientation of their dipoles. Such permanent dipole-dipole interactions are known as Keesom interactions. Keesom interactions are stronger than London dispersion forces and play a crucial role in interactions between polar molecules. It is important to note that for certain cases, there can be additional contributions from Debye interactions for particles in polar media. The total van der Waals interactions between two colloidal particles can be obtained by summing the contributions from each of these three types of van der Waals interactions.

The van der Waals interactions are effective between 0.1 nm and 10 nm and their strength depends on the dielectric properties of the colloidal particles and the suspending medium. For the disc-shaped clay platelets used in this thesis, the van der Waals interaction energy between two plates is given by [20]:

$$W_{vdW} = -\frac{A_H}{48\pi}\left[\frac{1}{d^2} + \frac{1}{(d+\Delta)^2} - \frac{2}{(d+\Delta/2)^2}\right] \tag{1.1}$$

where $d$ is the half-distance between two plates. For Laponite clay platelets, $d$ is the distance between the planes of the tetrahedral sheet and the centers of the oxygen atoms and $A_H$ is the Hamaker constant ($1.06 \times 10^{-20}$ J) [20]. Laponite particles consist of an octahedral sheet between two tetrahedral sheets, forming a unit cell as shown in Fig. 1.4(b). Detailed descriptions of structure and properties of Laponite can be found at https://pubchem.ncbi.nlm.nih.gov/compound/Laponite

### Electric double layer interactions

When a colloidal particle is suspended in a liquid, it can acquire charges by various mechanisms such as isomorphous substitution [26, 27], surface adsorption of surfactants [28, 29] and ionic exchange [30, 31]. The charged colloidal particles suspended in the electrolyte solution are surrounded by a layer containing an equal amount of oppositely charged counterions such that these counterions effectively neutralize

the surface charge of the particles. The counterions surrounding the charged particle are diffusive due to thermal fluctuations and screens the surface charge on the particle. The diffusive layer of counterions and the surface charges collectively form an electric double layer (EDL) [18]. The overlap of the diffuse layers in the EDLs of two colloidal particles give rise to an electrostatic repulsion which is also known as electric double layer repulsion. The length scales over which the electric double layer repulsion is effective is described by the Debye screening length ($1/\kappa$) which is related to electrolyte concentration $n$ as follows [32]:

$$\frac{1}{\kappa} = \sqrt{\frac{\epsilon_o \epsilon_r k_B T}{\sum_i (Z_i e)^2 n_i}} \tag{1.2}$$

where $\epsilon_o$ is the permittivity of vacuum, $\epsilon_r$ is the relative permittivity of the medium, $k_B$ is the Boltzmann constant, $T$ is the suspension temperature, $e$ is an electronic charge and $Z_i$ is the valency of the $i$th ion species of concentration $n_i$. The layer comprising the counterions that are attracted to the opposite particle surface charges at a very close distance is known as a Stern layer [33]. It is challenging to measure the exact potential at the particle surface. However, a good approximation of the experimentally measured potential is Zeta potential [18, 20, 34]. Zeta potential is the potential at the slipping plane, a layer of the surrounding solvent that remains attached to the particle during its motion. The EDL interaction energy between two Laponite platelets separated by a distance $2d$ assuming a small double layer overlap ($2d > 1/\kappa$) is given by [20]:

$$W_{EDL} = \left(\frac{64 n k_B T}{\kappa}\right) \gamma^2 e^{-2\kappa d} \tag{1.3}$$

where $n$ is the number density of ions and $\gamma = tanh(ze\phi_o/k_B T)$, $z$ is the valence of the counterions and $\phi_o$ is the surface electric potential.

## 1.5 Colloidal glass transition

Glass is an arrested state which is achieved by rapid cooling of the sample such that it is liquid-like but with ceased microscopic dynamics [37–40]. The temperature corresponding to this sudden arrest is known as grass transition temperature $T_g$. The kinetically arrested state is associated with a rapid rise in the viscosity, relaxation time and heat capacity near to the glass transition temperature $T_g$ [40–43]. According to IUPAC [International Union of Pure and Applied Chemistry, Pure and Appl. Chem. Vol 66, pp 577-594, 1994), a supercooled atomic liquid has achieved its glass transition when its viscosity reaches $10^{13}$ Pa.s. This makes it difficult to study the particle dynamics of glassformers in a laboratory. To overcome these experimental difficulties, colloidal (colloidal particle size- 10 nm to 1 $\mu$m) suspensions are used as a model system to study glass transition via various techniques such as light scattering, rheology, microscopy that are impossible to adapt to the study of a molecular glass former [44–48]. The simplest interaction between two particles is the hard sphere interaction [49]. A suspension of hard colloidal spheres is often used

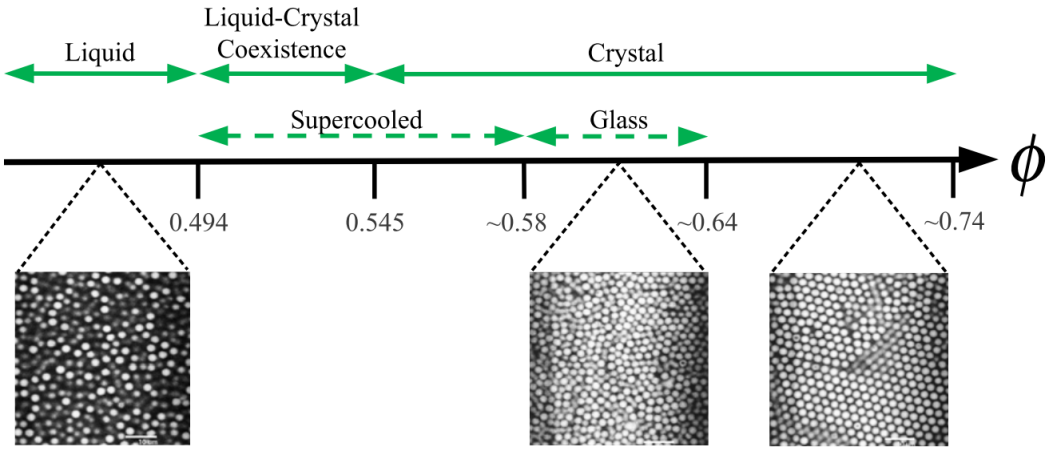



**Fig. 1.2:** Top: phase diagram of monodisperse hard spheres as a function of volume fraction $\phi$. Equilibrium states and non-equilibrium states are denoted by solid green and dashed green lines, respectively. A minimum of 8 % particle polydispersity is required for the existence of a glassy phase [35, 36]. Bottom: Sequence of phases obtained from confocal microscopy of a colloidal suspension with 5% polydispersity. This figure is adapted from [37] with permission.

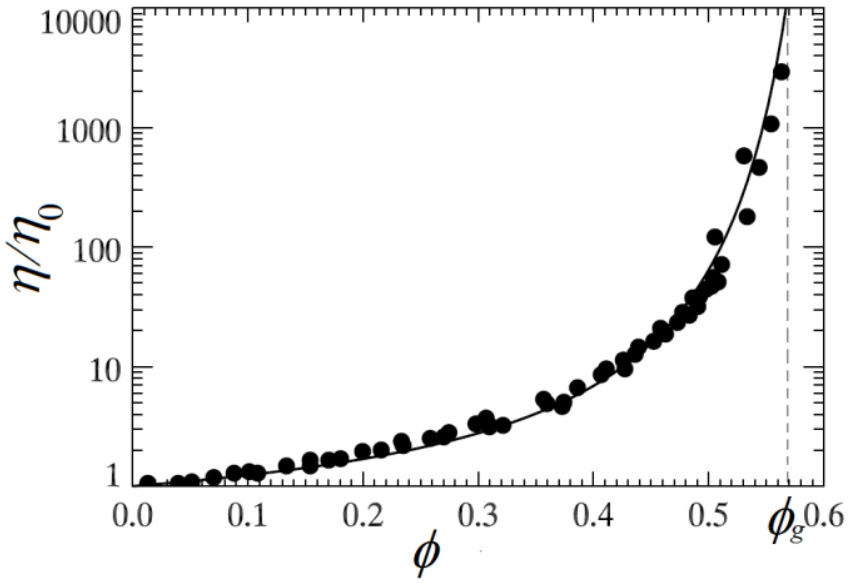



**Fig. 1.3:** Shear viscosity ($\eta$) normalized by the viscosity of the medium ($\eta_o$) is plotted against volume fraction $\phi$ for various colloidal suspensions of nearly monodisperse hard spheres. The dashed line represents the volume fractions close to glass transition volume fraction $\phi_g$. The black line is the fit to Doolittle equation $\frac{\eta}{\eta_o} = C\exp(\frac{\phi}{\phi_m - \phi})$ where $\phi_m$ is volume fraction corresponding to the random close packing of hard spheres [50]. This figure is adapted from [37] with permission.

as a model system to understand the glass transition phenomenon [37]. The volume fraction $\phi = NV_p/V$ is a key control parameter in colloidal suspensions, where $N$ is the number of colloidal particles, $V_P$ is the volume of a single particle and $V$ is the total system volume.

The first experimental study of the phase behavior of colloidal suspensions was performed by Pusey and van Megen [51, 52]. Figure 1.2 shows the phase diagram of colloidal hard spheres with polydispersity $\sim 8$ % as a function of volume fraction $\phi$. An equilibrium liquid state exists for $\phi = 0.494$ which is eventually followed by a crystalline state at $\phi > 0.494$. However, crystallization can be avoided by rapidly increasing $\phi$ such that a supercooled or glassy state forms between $0.494 \leq \phi \leq \phi_g \approx 0.58$. Here, $\phi_g$ denotes the glass transition volume fraction and a glassy region forms in the range $\phi_g \leq \phi \leq \phi_{rcp} \approx 0.64$. Here, $\phi_{rcp}$ is the volume fraction for random close packing. A minimum of 8 % particle polydispersity is required for the

existence of a glassy phase [35, 36]. For denser particle packing, a hexagonal close packed state is seen at $\phi_{hcp} = 0.74$. The packing fraction for random close packing of hard spheres depends on the polydispersity of the system [53]. While incorporating polydispersity increases the random close packing volume fraction $\phi_{rcp}$ to higher values [35, 54], adding charges to the particles shifts $\phi_{rcp}$ to lower values [55–57]. In suspensions of colloidal particles with electric double layers, a glassy phase can be achieved at lower concentrations when compared to hard spheres [58–60]. At the glass transition volume fraction $\phi_g$, the kinetically arrested state of colloidal particles can be described by a caging picture wherein the viscosity of the system increases drastically (Fig. 1.3) due to a dramatic slowing down of particle dynamics in the crowded environment [40, 48]. This drastic increase in viscosity of the colloidal suspensions near $\phi_g$ is reminiscent of the rapid increase in viscosity (upto $10^{12}$ Pa.s) previously seen in molecular glass former upon rapidly quenching the temperature down to the glass transition temperature $T_g$ [40].

## 1.6 Aqueous Laponite suspensions

Synthetic clay particles of Laponite® are disk-shaped with diameters 25-30 nm and thickness $\approx$ 1 nm (Fig. 1.4(a)). Laponite is a 2:1 synthetic hectorite clay mineral with a two-dimensional array of silicon−oxygen tetrahedra that is sandwiched between arrays of oxygen−magnesium−hydroxyl octahedra (Fig. 1.4(b)). Dry Laponite powder exists in the form of one-dimensional stacks called tactoids, with $Na^+$ ions residing in the intergallery spaces of the clay platelets [20]. In an aqueous suspension of pH $<$ 11, the rims of the Laponite particles bear positive charges [61]. The Laponite faces acquire negative charges due to the diffusion of $Na^+$ ions into the aqueous medium [20, 62]. These $Na^+$ counterions contribute to the formation of diffuse electric double layers around the Laponite particles. Osmotic pressure differences within the suspension cause tactoid swelling and the eventual exfoliation of Laponite platelets from the ends of the tactoids [59, 63].

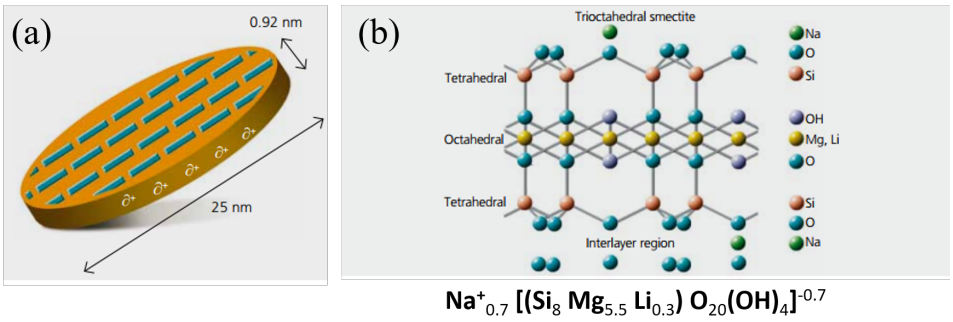



**Fig. 1.4:** (a) Schematic of a Laponite particle when dispersed in water. (b) Schematic illustrating a unit cell of Laponite particle with an octahedral sheet (O) sandwiched between two tetrahedral sheets. Intergallery space is acquired by sodium atoms. These images are adapted from www.byk.com.

This results in a time-dependent inter-particle electrostatic potential, such that the heterogeneously charged Laponite particles gradually self-assemble to form fragile microstructures composed of overlapping coins and house of cards (HoC) aggregates [64]. The percolation of these microstructures throughout the sample is accompanied by continuous particle rearrangements within the fragile suspension structures. These processes contribute to a spontaneous temporal increase in sample rigidity in a phenomenon identified as physical aging [65]. It was reported that the aging of aqueous Laponite suspensions can be controlled by changing clay concentration and suspension temperature, and by incorporating various additives in the dispersion medium [63, 66–68]. The inclusion of dissociating additives modifies interparticle electrostatic interactions, thereby altering the aging dynamics of the clay suspension [68]. Non-dissociating additives, in contrast, alter the structure of the dispersion medium. The resultant changes in intermolecular solvation forces have a non-trivial influence on sample aging [63]. Investigations into the phase behavior of Laponite suspensions have reported phase separation below a concentration of 1 % w/v [69], structural buildup and aging, presumably through Laponite house of cards (HoC) associations, between 1 % w/v and 2 % w/v [70, 71] and formation of a colloidal glassy phase above 2 % w/v [72].

## 1.7 Janus particles

Unlike passive Brownian particles, active particles self-propel by consuming energy from the surroundings and converting it into directed motion [73]. Janus particles are named after the ancient Roman God Janus Bifrons, who has two faces, one gazing into the past and the other into the future. Janus particles have two opposite faces, exhibiting different physical and chemical properties. This asymmetry causes self-propulsion of these active Janus particles. For example, the two opposite faces can be characterized by different charges, hydrophobicities, fluorescence, and electrical or mechanical properties [74–76]. Janus particles have potential applications as biomarkers, sensors, in textiles and in the stabilization of emulsions, etc [77–80]. A review article [81] covered the three major ways of synthesizing Janus particles: masking, self-assembly and phase separation [82]. In this thesis, we employ the masking technique to synthesize Janus particles. Masking can be done in two ways, *viz* by evaporative deposition or by suspension at the interface of two fluids [82]. In the evaporative deposition [83] technique, a homogeneous monolayer of particles is deposited on a substrate and kept in an evaporation chamber to treat the unexposed surface of the particles with metals like gold (Au), platinum (Pt) or aluminum (Al). The particles are finally detached from the substrate. On the other hand, in the phase separation technique [84], the particles are chemically treated at the interface between two fluids and then finally released in homogeneous solutions. In this thesis, we use the evaporative deposition technique to synthesize Pt-coated Janus particles which self propel in the presence of hydrogen peroxide $H_2O_2$ by the catalytic decomposition of $H_2O_2$ into water and oxygen [85]. In this self-propulsion mechanism, the half-Pt-coated spherical particles cause asymmetric distribution of reaction products around the particle surface [86, 87]. The decomposition reaction as follows:

$$2H_2O_2 \xrightarrow{Pt} 2H_2O + O_2 \tag{1.4}$$

## 1.8 Interfacial instabilities

The interface between two fluids in a porous medium, in general, is seen to be unstable when a less viscous fluid displaces a more viscous fluid. The intrusion of one fluid into another leads to formation of a wide range of interfacial patterns that depend on surface tension gradients [88, 89], viscoelasticities of the fluids [90–97], the driving pressures imposed during their injection [98], etc. The formation of complex patterns has been objects of intense scrutiny and found across different length scales, such as ripples in sand, tree branches, dendritic structures in snowflakes, the branching morphogenesis in vertebrate airways [99]. While patterns arise from a system's need to optimize its function, a complete understanding of the mechanisms of their growth and evolution remains elusive.

Given the experimental difficulties in tracking and obtaining useful information about flow in a porous medium, the quasi-two-dimensional Hele-Shaw cell [100] geometry, a setup of typically tiny gap between closely spaced parallel plates, is extensively used as a more straightforward option in the study of interfacial patterns. Since flow in the Hele-Shaw geometry is averaged across the gap, both scenarios can be described by Darcy's law [101]. In Darcy's law, the flow velocity in a narrow channel or a porous medium, $u$, is related to the gradient of pressure ($\nabla P$) as follows::

$$u = -\frac{k}{\eta}\nabla P, \tag{1.5}$$

where $k$ is the permeability of the porous medium and $\eta$ is the viscosity of the fluid. The seminal work of Saffman et al. [102] on the displacement of oil by air in a vertical Hele-Shaw cell geometry (Fig. 1.5) showed that the unstable interface evolves into finger-like patterns that are now popularly referred to as Saffman Taylor fingers or viscous fingers. In [102], the flow in the vertical channel (Fig. 1.5) was governed by the equation of continuity $\nabla.u = 0$, and replacing $u$ using equation 1.5 leads to $\nabla.u = \nabla^2\ \phi$ where, $\phi = (k/\eta)P$. The solutions are given by $\phi_1 = e^{\sigma t}e^{\alpha x+\alpha y}e^{-\alpha z}$ and $\phi_2 = e^{\sigma t}e^{\alpha x+\alpha y}e^{\alpha z}$. The flow is uniform in $x$ and $y$ direction and $\sigma$ is the growth

rate of the perturbations at the interface between the fluid pair which is written as:

$$\frac{\sigma}{\alpha}\left(\frac{\eta_1}{k_1}+\frac{\eta_2}{k_2}\right)=(\rho_1-\rho_2)\,g+\left(\frac{\eta_1}{k_1}-\frac{\eta_2}{k_2}\right)V, \tag{1.6}$$

where, $\eta_1$ and $\eta_2$ are the viscosities of the displacing and displaced fluid, $g$ is the acceleration due to gravity and $V$ is the uniform velocity in the $z$ direction. For the case when densities of the fluid pair is equal, $\sigma > 0$ indicates the growth of perturbation at the interface and therefore, the viscosity of displaced fluid ($\eta_2$) should be greater than the viscosity of displacing fluid ($\eta_1$). For displacements in the horizontal direction, for example, in a quasi two-dimensional radial Hele-Shaw cell, the density term in equation 1.6 becomes zero and the growth of perturbations is governed by the viscosity contrast between the fluid pair.

### 1.8.1 Instabilities at the interface between two Newtonian fluids

A few studies have focused on the vital role that viscosity mismatch plays in the emergence of interfacial patterns in a Hele-Shaw cell [103, 104]. Lajeunesse *et*

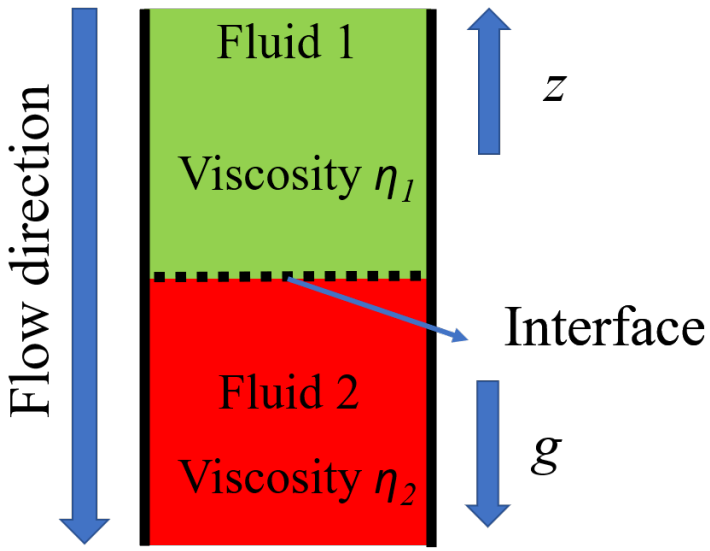



**Fig. 1.5:** Schematic illustration of a vertical Hele-Shaw cell to explain Saffman-Taylor instability.

*al*. [103] studied the downward miscible displacement of a Newtonian fluid by a less viscous fluid and reported the formation of 3D patterns comprising periodic fingers. Bischofberger *et al*. [104] studied pattern evolution at the interface between a pair of miscible Newtonian fluids subject to radial displacement in a Hele-Shaw cell over a wide range of viscosity ratios. Regardless of whether the displacement was rectilinear or radial, a complete suppression of interfacial instability was reported in these experiments above a critical value of viscosity ratio of the inner and outer fluids, $\eta_{in}/\eta_{out}$. Interfacial patterns resulting from the displacement of one Newtonian fluid by another were reported to be sensitive to the miscibility of the fluid pair [89, 105, 106]. Since the formation of sharp tips costs more energy when the interfacial tension is non-zero, immiscible displacement patterns preferentially preserve smooth and rounded finger-tips. A delay in the onset of instability at non-zero interfacial tension was observed in previous experiments involving Newtonian fluid pairs [89, 106]. The other factors affecting the interfacial instabilities at the Newtonian-Newtonian fluids interface are wettability of the fluid pair [107], the gap of the HS cell [93], and the pressure gradient [98].

### 1.8.2 Instabilities at the interface between Newtonian and non-Newtonian fluids

Instabilities that arise due to the displacement of a non-Newtonian fluid by a Newtonian fluid result in interfacial patterns that are quite distinct from those involving Newtonian-Newtonian displacements [90–94, 97]. Given the importance of interfacial dynamics in the design of technological processes involving non-Newtonian fluids [91, 108], researchers have attempted to comprehend instabilities at Newtonian-non-Newtonian fluid interfaces. While some theoretical studies have explored the interface between shear-thinning and Newtonian fluids [90, 109], interfaces involving non-Newtonian fluids such as polymer solutions [110, 111] and colloidal suspensions [93, 94, 112] have been investigated experimentally in Hele-Shaw cells. In experiments involving the displacement of polymer solutions by air, the shear-

thinning behavior of the polymer solutions was shown to result in the narrowing of fingers [110, 111], while elasticity contributed to the formation of wider fingers [110]. Numerical simulations revealed that the displacement of shear-thinning fluids by air resulted in the narrowing of fingers, multiple side branches and a suppression in finger-tip splitting [90]. When foam, an yield stress fluid, was displaced by air at increasing shear rates, a transition from jagged interfaces, believed to arise from the distortions and rearrangements of foam bubbles at high shear rates, to smooth interfacial patterns, was observed experimentally [91].

Apart from displacements experiments, the withdrawal of polyethylene-silicone oil granular mixtures also resulted in a series of interfacial morphologies depending on the particle size, the particle aggregation structures, the hydrodynamic condition and the withdrawal rate of the mixture [113]. The radial displacement of Bentonite clay suspensions by water resulted in viscoelastic fracturing when the stored elastic energy of the displaced suspension exceeded the energy required for fracture onset [93]. The nonlinear flow behavior of dense, viscoelastic suspensions of particles in water, for example, mud flows [114], cement slurries [115], magma and jammed suspensions of anisotropic cornstarch particles [8, 116–118] are also of great importance from a material processing point of view.

A fundamental understanding of the mechanisms responsible for pattern evolution is key to the design and enhancement of certain processes such as filtration, porous media flows, electrodeposition of copper [119] and lithium [120] and in carbon sequestration [121]. There are also certain settings where interfacial instabilities are not always desirable, for example, the formation of lithium dendrites due to instabilities at lithium anode-electrolyte interfaces in rechargeable batteries [122], and the growth and development of viscous fingers at a water/gas-oil interface that can reduce the efficiency of oil recovery [123, 124]. Therefore, control of interfacial instabilities, whether in their suppression or enhancement, has captivated researchers in recent years. Given the experimental difficulties in tracking and analyzing flow through porous media, the quasi-two-dimensional Hele-Shaw cell [100] is extensively

used as an alternative option in the study of interfacial patterns, especially those produced by the mismatch of viscosities between fluids. The control of instabilities at the interface between a pair of fluids is crucial in material transport. In the present thesis, we study different strategies to systematically suppress and enhance interfacial instabilities by controlling the shear and time-dependent complex flow behavior of different viscoelastic materials.

## 1.9 Effect of active particles on a crowded environment of passive particles

Active particles have recently received a lot of interest for their ability to consume energy from their environment and transform it into motion [73, 125, 126]. A dense passive system exhibits a kinetically arrested state near the critical volume fraction $\phi_g$ (as discussed in section 1.5 ). In contrary to passive systems, active particles in suspension show self-clustering and local jamming. A transition from an aligned phase to a jammed phase of soft active disks with an increase in particle density was reported in an earlier study [127]. Active particles show collective dynamics in the high density regimes. Furthermore, it was observed that increase in activity shifts the critical density required to obtain a dynamically arrested state to higher values [128, 129]. Recent studies had studied the effect of doping of dense colloidal suspension with a small number of active particles and had reported a shift in the glass transition in a mixture of active and passive particles [130, 131]. Theoretical and numerical studies have demonstrated activity-induced cage breaking in an arrested state of bidisperse passive particles in suspension [132]. In this thesis, we perform an experimental study of the effect of activity on the dynamics of passive particles in a crowded environment of bidisperse passive hard spheres.

## 1.10 Thesis organization

This thesis studies the non-equilibrium flows of soft materials under confinement and in the presence of activity. Following this introduction (Chapter 1), sample preparation protocols and various experimental techniques used in this thesis are described in chapter 2. Chapter 3 presents the onset and development of instabilities during the displacement of a shear-thinning viscoelastic fluid (aqueous cornstarch suspensions of varying concentrations, displaced fluid) by a Newtonian fluid (glycerol-water mixtures of different viscosities, displacing fluid) in a radial Hele-Shaw cell geometry. The displacement of shear-thickening cornstarch suspensions in a confined geometry by water and the emergence of transient reverse fingers are discussed in chapter 4. Chapter 5 describes the influence of the shear-dependent viscosities and aging dynamics of aqueous Laponite suspensions on the morphologies of the observed interfacial patterns. In chapter 6, the growth kinetics of distinct interfacial pattern morphologies observed during the displacement of aqueous Laponite suspensions by Newtonian fluids is discussed. Chapter 7 describes the effect of activity on the dynamics of passive colloids in a crowded environment of binary passive particles in suspension. A summary of the results and the future scope of research are discussed in chapter 8.

# References


[1] R. Jones, Soft Condensed Matter, Oxford Master Series in Physics, OUP Oxford, 2002.

[2] M. Doi, Soft Matter Physics, EBL-Schweitzer, OUP Oxford, 2013.

[3] E. Guazzelli, O. Pouliquen, Rheology of dense granular suspensions, Journal of Fluid Mechanics 852 (2018) P1. doi:10.1017/jfm.2018.548.

[4] B. Andreotti, Y. Forterre, O. Pouliquen, Granular Media: Between Fluid and Solid, Cambridge University Press, 2013. doi:10.1017/CBO9781139541008.

[5] D. Feys, R. Verhoeven, G. De Schutter, Fresh self compacting concrete, a shear-thickening material, Cement and Concrete Research 38 (7) (2008) 920–929. doi:https://doi.org/10.1016/j.cemconres.2008.02.008.

[6] T. S. Majmudar, R. P. Behringer, Contact force measurements and stress-induced anisotropy in granular materials, Nature 435 (7045) (2005) 1079–1082. doi:10.1038/nature03805.

[7] A. Fall, F. Bertrand, G. Ovarlez, D. Bonn, shear-thickening of cornstarch suspensions, Journal of Rheology 56 (3) (2012) 575–591. doi:10.1122/1.3696875.

[8] I. R. Peters, S. Majumdar, H. M. Jaeger, Direct observation of dynamic shear jamming in dense suspensions, Nature 532 (7598) (2016) 214–217. doi:10.1038/nature17167.

[9] N. J. Wagner, J. F. Brady, shear-thickening in colloidal dispersions, Physics Today 62 (10) (2009) 27–32. doi:10.1063/1.3248476.

[10] X. Cheng, J. H. McCoy, J. N. Israelachvili, I. Cohen, Imaging the microscopic structure of shear-thinning and thickening colloidal suspensions, Science 333 (6047) (2011) 1276–1279. doi:10.1126/science.1207032.

[11] N. C. Crawford, L. B. Popp, K. E. Johns, L. M. Caire, B. N. Peterson, M. W. Liberatore, shear-thickening of corn starch suspensions: Does concentration matter?, Journal of Colloid and Interface Science 396 (2013) 83–89. doi:https://doi.org/10.1016/j.jcis.2013.01.024.

[12] A. Fall, A. Lemaître, F. m. c. Bertrand, D. Bonn, G. Ovarlez, Shear Thickening and Migration in Granular Suspensions, Phys. Rev. Lett. 105 (2010) 268303. doi:10.1103/PhysRevLett.105.268303.

[13] D. R. FOSS, J. F. BRADY, Structure, diffusion and rheology of Brownian suspensions by stokesian dynamics simulation, Journal of Fluid Mechanics 407 (2000) 167–200. doi:10.1017/S0022112099007557.

[14] R. Seto, R. Mari, J. F. Morris, M. M. Denn, Discontinuous shear-thickening of frictional hard-sphere suspensions, Phys. Rev. Lett. 111 (2013) 218301. doi:10.1103/PhysRevLett.111.218301.

[15] M. Wyart, M. E. Cates, Discontinuous shear-thickening without inertia in dense non-brownian suspensions, Phys. Rev. Lett. 112 (2014) 098302. doi:10.1103/PhysRevLett.112.098302.

[16] V. Rathee, D. L. Blair, J. S. Urbach, Localized stress fluctuations drive shear-thickening in dense suspensions, Proceedings of the National Academy of Sciences 114 (33) (2017) 8740–8745. doi:10.1073/pnas.1703871114.

[17] M. Nabizadeh, A. Singh, S. Jamali, Structure and dynamics of force clusters and networks in shear-thickening suspensions, Phys. Rev. Lett. 129 (2022) 068001. doi:10.1103/PhysRevLett.129.068001.

[18] R. Hunter, L. White, D. Chan, Foundations of Colloid Science, no. v. 1 in Foundations of Colloid Science, Clarendon Press, 1987.

[19] T. Graham, X. liquid diffusion applied to analysis, Philosophical Transactions of the Royal Society of London 151 (1861) 183–224. doi:10.1098/rstl.1861.0011.

[20] H. Van Olphen, An Introduction to Clay Colloid Chemistry: For Clay Technologists, Geologists and Soil Scientists, Wiley, New York, 1977.

[21] A. Einstein, Über die von der molekularkinetischen theorie der wärme geforderte bewegung von in ruhenden flüssigkeiten suspendierten teilchen, Annalen der Physik 322 (8) (1905) 549–560. doi:https://doi.org/10.1002/andp.19053220806.

[22] B. V. Derjaguin, L. Landau, Theory of stability of strongly charged lyophobic sols and of the adhesion of strongly charged particles in solutions of electrolytes, Acta Physicochim 17 (1941) 633–662.

[23] E. Vervey, J. Overbeek, Theory of Stability of Lyophobic Colloids, Elseviers, 1948.

[24] A. Stone, The Theory of Intermolecular Forces, Oxford University Press, 2013. doi:10.1093/acprof:oso/9780199672394.001.0001.

[25] F. London, The general theory of molecular forces, Trans. Faraday Soc. 33 (1937) 8b–26. doi:10.1039/TF937330008B.

[26] G. Lagaly, S. Ziesmer, Colloid chemistry of clay minerals: the coagulation of montmorillonite dispersions, Advances in Colloid and Interface Science

100-102 (2003) 105–128. doi:https://doi.org/10.1016/S0001-8686(02)00064-7.

[27] X. Yin, V. Gupta, H. Du, X. Wang, J. D. Miller, Surface charge and wetting characteristics of layered silicate minerals, Advances in Colloid and Interface Science 179-182 (2012) 43–50, interfaces, Wettability, Surface Forces and Applications: Special Issue in honour of the 65th Birthday of John Ralston. doi:https://doi.org/10.1016/j.cis.2012.06.004.

[28] E. Lee, L. Koopal, Adsorption of cationic and anionic surfactants on metal oxide surfaces: surface charge adjustment and competition effects., Journal of Colloid and Interface Science 177 (1996) 478–489. doi:10.1006/jcis.1996.0061.

[29] K. G. Marinova, R. G. Alargova, N. D. Denkov, O. D. Velev, D. N. Petsev, I. B. Ivanov, R. P. Borwankar, Charging of oil−water interfaces due to spontaneous adsorption of hydroxyl ions, Langmuir 12 (8) (1996) 2045–2051. doi:10.1021/la950928i.

[30] C. A. Bunton, F. Nome, F. H. Quina, L. S. Romsted, Ion binding and reactivity at charged aqueous interfaces, Accounts of Chemical Research 24 (1991) 357–364. doi:10.1021/AR00012A001.

[31] L. H. Allen, E. Matijevic´, Stability of colloidal silica: Ii. ion exchange, Journal of Colloid and Interface Science 33 (3) (1970) 420–429. doi:https://doi.org/10.1016/0021-9797(70)90234-1.

[32] J. Israelachvili, Intermolecular and Surface Forces, Academic Press, New York, 2010.

[33] O. Stern, Zur theorie der elektrolytischen doppelschicht, Zeitschrift für Elektrochemie und angewandte physikalische Chemie 30 (21-22) (1924) 508–516. doi:https://doi.org/10.1002/bbpc.192400182.

[34] D. Wang, Colloid science. principles, methods and applications. edited by terence cosgrove., Angewandte Chemie International Edition 45 (16) (2006) 2498–2498. arXiv:https://onlinelibrary.wiley.com/doi/pdf/10.1002/anie.200585362, doi:https://doi.org/10.1002/anie.200585362.

[35] P. N. Pusey, E. Zaccarelli, C. Valeriani, E. Sanz, W. C. K. Poon, M. E. Cates, Hard spheres: crystallization and glass formation, Philosophical Transactions of the Royal Society A: Mathematical, Physical and Engineering Sciences 367 (1909) (2009) 4993–5011. doi:10.1098/rsta.2009.0181.

[36] E. Zaccarelli, C. Valeriani, E. Sanz, W. C. K. Poon, M. E. Cates, P. N. Pusey, Crystallization of Hard-Sphere Glasses, Phys. Rev. Lett. 103 (2009) 135704. doi:10.1103/PhysRevLett.103.135704.

[37] G. L. Hunter, E. R. Weeks, The physics of the colloidal glass transition, Reports on Progress in Physics 75 (6) (2012) 066501. doi:10.1088/0034-4885/75/6/066501.

[38] F. H. Stillinger, A topographic view of supercooled liquids and glass formation, Science 267 (5206) (1995) 1935–1939. doi:10.1126/science.267.5206.1935.

[39] P. G. Debenedetti, F. H. Stillinger, Supercooled liquids and the glass transition, Nature 410 (6825) (2001) 259–267. doi:10.1038/35065704.

[40] C. A. Angell, Formation of glasses from liquids and biopolymers, Science 267 (5206) (1995) 1924–1935. doi:10.1126/science.267.5206.1924.

[41] M. D. Ediger, P. Harrowell, Perspective: Supercooled liquids and glasses, The Journal of Chemical Physics 137 (8) (2012) 080901. doi:10.1063/1.4747326.

[42] M. D. Ediger, Spatially heterogeneous dynamics in supercooled liquids, Annual Review of Physical Chemistry 51 (1) (2000) 99–128, pMID: 11031277. doi:10.1146/annurev.physchem.51.1.99.

[43] V. N. Novikov, A. P. Sokolov, Poisson's ratio and the fragility of glass-forming liquids, Nature 431 (7011) (2004) 961–963. doi:10.1038/nature02947.

[44] D. Saha, Y. M. Joshi, R. Bandyopadhyay, Investigation of the dynamical slowing down process in soft glassy colloidal suspensions: comparisons with supercooled liquids, Soft Matter 10 (2014) 3292–3300. doi:10.1039/C4SM00187G.

[45] K. Hima Nagamanasa, S. Gokhale, A. K. Sood, R. Ganapathy, Direct measurements of growing amorphous order and non-monotonic dynamic correlations in a colloidal glass-former, Nature Physics 11 (5) (2015) 403–408. doi:10.1038/nphys3289.

[46] P. N. Pusey, R. J. A. Tough, Particle Interactions, Springer US, Boston, MA, 1985, pp. 85–179. doi:10.1007/978-1-4613-2389-1_4.

[47] E. Weeks, J. Crocker, A. Levitt, A. Schofield, D. Weitz, Three-dimensional direct imaging of structural relaxation near the colloidal glass transition, Science 287 (5453) (2000) 627–631. doi:10.1126/science.287.5453.627.

[48] E. R. Weeks, D. A. Weitz, Subdiffusion and the cage effect studied near the colloidal glass transition, Chemical Physics 284 (1-2) (2002) 361–367.

[49] The bakerian lecture, 1962 the structure of liquids, Proceedings of the Royal Society of London. Series A. Mathematical and Physical Sciences 280 (1382) (1964) 299–322. doi:10.1098/rspa.1964.0147.

[50] A. K. Doolittle, Studies in newtonian flow. ii. the dependence of the viscosity of liquids on free-space, Journal of Applied Physics 22 (12) (1951) 1471–1475. doi:10.1063/1.1699894.

[51] P. N. Pusey, W. van Megen, Phase behaviour of concentrated suspensions of nearly hard colloidal spheres, Nature 320 (6060) (1986) 340–342. doi:10.1038/320340a0.

[52] P. N. Pusey, W. van Megen, Observation of a glass transition in suspensions of spherical colloidal particles, Phys. Rev. Lett. 59 (1987) 2083–2086. doi:10.1103/PhysRevLett.59.2083.

[53] S. Torquato, T. M. Truskett, P. G. Debenedetti, Is Random Close Packing of Spheres Well Defined?, Phys. Rev. Lett. 84 (2000) 2064–2067. doi:10.1103/PhysRevLett.84.2064.

[54] M. Fasolo, P. Sollich, Equilibrium Phase Behavior of Polydisperse Hard Spheres, Phys. Rev. Lett. 91 (2003) 068301. doi:10.1103/PhysRevLett.91.068301.

[55] A.-P. Hynninen, M. Dijkstra, Phase diagrams of hard-core repulsive Yukawa particles, Phys. Rev. E 68 (2003) 021407. doi:10.1103/PhysRevE.68.021407.

[56] W. Härtl, Colloidal glasses, Current Opinion in Colloid & Interface Science 6 (5) (2001) 479–483. doi:https://doi.org/10.1016/S1359-0294(01)00120-0.

[57] J. Hernández-Guzmán, E. R. Weeks, The equilibrium intrinsic crystal-liquid interface of colloids, Proceedings of the National Academy of Sciences 106 (36) (2009) 15198–15202. doi:10.1073/pnas.0904682106.

[58] H. Tanaka, J. Meunier, D. Bonn, Nonergodic states of charged colloidal suspensions: Repulsive and attractive glasses and gels, Phys. Rev. E 69 (2004) 031404. doi:10.1103/PhysRevE.69.031404.

[59] R. Bandyopadhyay, D. Liang, H. Yardimci, D. A. Sessoms, M. A. Borthwick, S. G. J. Mochrie, J. L. Harden, R. L. Leheny, Evolution of particle-scale dynamics in an aging clay suspension, Phys. Rev. Lett. 93 (2004) 228302. doi:10.1103/PhysRevLett.93.228302.

[60] K. Kang, J. K. G. Dhont, Glass transition in suspensions of charged rods: Structural arrest and texture dynamics, Phys. Rev. Lett. 110 (2013) 015901. doi:10.1103/PhysRevLett.110.015901.

[61] C. Martin, F. Pignon, J.-M. Piau, A. Magnin, P. Lindner, B. Cabane, Dissociation of thixotropic clay gels, Phys. Rev. E 66 (2002) 021401. doi:10.1103/PhysRevE.66.021401.

[62] F. Bergaya, G. Lagaly, Handbook of Clay Science: Part A Fundamentals, 2nd ed., Vol. 5A, Elsevier, Amsterdam, 2013.

[63] C. Misra, V. T. Ranganathan, R. Bandyopadhyay, Influence of medium structure on the physicochemical properties of aging colloidal dispersions investigated using the synthetic clay Laponite®, Soft Matter 17 (2021) 9387–9398. doi:10.1039/D1SM00987G.

[64] M. Delhorme, B. Jönsson, C. Labbez, Monte Carlo simulations of a clay inspired model suspension: the role of rim charge, Soft Matter 8 (2012) 9691–9704. doi:10.1039/C2SM25731A.

[65] S. Ali, R. Bandyopadhyay, Effect of electrolytes on the microstructure and yielding of aqueous dispersions of colloidal clay, Soft Matter 12 (2016) 414–421. doi:10.1039/C5SM01700A.

[66] V. Thrithamara Ranganathan, R. Bandyopadhyay, Effects of aging on the yielding behaviour of acid and salt induced Laponite gels, Colloids Surf. A Physicochem. Eng. Asp. 522 (2017) 304–309. doi:10.1016/j.colsurfa.2017.03.006.

[67] A. Shahin, Y. M. Joshi, Physicochemical Effects in Aging Aqueous Laponite Suspensions, Langmuir 28 (44) (2012) 15674–15686. doi:10.1021/la302544y.

[68] D. Saha, R. Bandyopadhyay, Y. M. Joshi, Dynamic Light Scattering Study and DLVO Analysis of Physicochemical Interactions in Colloidal Suspensions of Charged Disks, Langmuir 31 (10) (2015) 3012–3020. doi:10.1021/acs.langmuir.5b00291.

[69] B. Ruzicka, E. Zaccarelli, A fresh look at the Laponite phase diagram, Soft Matter 7 (4) (2011) 1268–1286. doi:10.1039/C0SM00590H.

[70] S. Jabbari-Farouji, H. Tanaka, G. H. Wegdam, D. Bonn, Multiple nonergodic disordered states in Laponite suspensions: A phase diagram, Phys. Rev. E 78 (2008) 061405. doi:10.1103/PhysRevE.78.061405.

[71] T. Nicolai, S. Cocard, Dynamic Light-Scattering Study of Aggregating and Gelling Colloidal Disks, J. Colloid Interface Sci. 244 (1) (2001) 51–57. doi:10.1006/jcis.2001.7930.

[72] R. Angelini, E. Zaccarelli, F. A. de Melo Marques, M. Sztucki, A. Fluerasu, G. Ruocco, B. Ruzicka, Glass–glass transition during aging of a colloidal clay, Nat. Commun. 5 (1) (2014) 4049. doi:10.1038/ncomms5049.

[73] S. Ramaswamy, The mechanics and statistics of active matter, Annual Review of Condensed Matter Physics 1 (1) (2010) 323–345. doi:10.1146/annurev-conmatphys-070909-104101.

[74] R. Nakamura, M. Tokuda, T. Suzuki, H. Minami, Preparation of poly(ionic liquid) hollow particles with switchable permeability, Langmuir 32 (10) (2016) 2331–2337. doi:10.1021/acs.langmuir.6b00263.

[75] A. Ghosh, P. Fischer, Controlled propulsion of artificial magnetic nanostructured propellers, Nano Letters 9 (6) (2009) 2243–2245. doi:10.1021/nl900186w.

[76] D. Nishiguchi, M. Sano, Mesoscopic turbulence and local order in janus particles self-propelling under an ac electric field, Phys. Rev. E 92 (2015) 052309. doi:10.1103/PhysRevE.92.052309.

[77] S.-H. Hu, X. Gao, Nanocomposites with spatially separated functionalities for combined imaging and magnetolytic therapy, Journal of the American Chemical Society 132 (21) (2010) 7234–7237. doi:10.1021/ja102489q.

[78] M. Yoshida, K.-H. Roh, S. Mandal, S. Bhaskar, D. Lim, H. Nandivada, X. Deng, J. Lahann, Structurally controlled bio-hybrid materials based on unidirectional association of anisotropic microparticles with human endothelial cells, Advanced Materials 21 (48) (2009) 4920–4925. doi:https://doi.org/10.1002/adma.200901971.

[79] B. J. Nelson, I. K. Kaliakatsos, J. J. Abbott, Microrobots for minimally invasive medicine, Annual Review of Biomedical Engineering 12 (1) (2010) 55–85, pMID: 20415589. doi:10.1146/annurev-bioeng-010510-103409.

[80] A. Synytska, R. Khanum, L. Ionov, C. Cherif, C. Bellmann, Water-repellent textile via decorating fibers with amphiphilic janus particles, ACS Applied Materials & Interfaces 3 (4) (2011) 1216–1220. doi:10.1021/am200033u.

[81] A. Walther, A. H. E. Müller, Janus particles: Synthesis, self-assembly, physical properties, and applications, Chemical Reviews 113 (7) (2013) 5194–5261. doi:10.1021/cr300089t.

[82] M. Lattuada, T. A. Hatton, Synthesis, properties and applications of janus nanoparticles, Nano Today 6 (2011) 286–308.

[83] J. C. Love, B. D. Gates, D. B. Wolfe, K. E. Paul, G. M. Whitesides, Fabrication and wetting properties of metallic half-shells with submicron diameters, Nano Letters 2 (8) (2002) 891–894. doi:10.1021/nl0256331.

[84] H. Gu, Z. Yang, J. Gao, C. K. Chang, B. Xu, Heterodimers of nanoparticles: formation at a liquid−liquid interface and particle-specific surface modification by functional molecules, Journal of the American Chemical Society 127 (1) (2005) 34–35. doi:10.1021/ja045220h.

[85] L. F. Valadares, Y.-G. Tao, N. S. Zacharia, V. Kitaev, F. Galembeck, R. Kapral, G. A. Ozin, Catalytic nanomotors: Self-propelled sphere dimers, Small 6 (4) 565–572. doi:https://doi.org/10.1002/smll.200901976.

[86] J. R. Howse, R. A. L. Jones, A. J. Ryan, T. Gough, R. Vafabakhsh, R. Golestanian, Self-motile colloidal particles: From directed propulsion to random walk, Phys. Rev. Lett. 99 (2007) 048102. doi:10.1103/PhysRevLett.99.048102.

[87] R. Golestanian, T. B. Liverpool, A. Ajdari, Propulsion of a molecular machine by asymmetric distribution of reaction products, Phys. Rev. Lett. 94 (2005) 220801. doi:10.1103/PhysRevLett.94.220801.

[88] J.-D. Chen, Growth of radial viscous fingers in a Hele-Shaw cell, J. Fluid Mech. 201 (1989) 223–242. doi:10.1017/S0022112089000911.

[89] I. Bischofberger, R. Ramachandran, S. R. Nagel, An island of stability in a sea of fingers: emergent global features of the viscous-flow instability, Soft Matter 11 (2015) 7428–7432. doi:10.1039/C5SM00943J.

[90] L. Kondic, M. J. Shelley, P. Palffy-Muhoray, Non-Newtonian Hele-Shaw Flow and the Saffman-Taylor Instability, Phys. Rev. Lett. 80 (1998) 1433–1436. doi:10.1103/PhysRevLett.80.1433.

[91] S. S. Park, D. J. Durian, Viscous and elastic fingering instabilities in foam, Phys. Rev. Lett. 72 (1994) 3347–3350. doi:10.1103/PhysRevLett.72.3347.

[92] Palak, R. Sathyanath, S. K. Kalpathy, R. Bandyopadhyay, Emergent patterns and stable interfaces during radial displacement of a viscoelastic fluid, Colloids

Surf. A Physicochem. Eng. Asp. 629 (2021) 127405. doi:https://doi.org/10.1016/j.colsurfa.2021.127405.

[93] E. Lemaire, P. Levitz, G. Daccord, H. Van Damme, From viscous fingering to viscoelastic fracturing in colloidal fluids, Phys. Rev. Lett. 67 (1991) 2009–2012. doi:10.1103/PhysRevLett.67.2009.

[94] D. Ozturk, M. L. Morgan, B. Sandnes, Flow-to-fracture transition and pattern formation in a discontinuous shear-thickening fluid, Commun. Phys. 3 (1) (2020) 1–9. doi:10.1038/s42005-020-0382-7.

[95] T. V. Ball, N. J. Balmforth, A. P. Dufresne, Viscoplastic fingers and fractures in a Hele-Shaw cell, J. Non-Newton. Fluid Mech. 289 (2021) 104492. doi:10.1016/J.JNNFM.2021.104492.

[96] K. Osei-Bonsu, N. Shokri, P. Grassia, Fundamental investigation of foam flow in a liquid-filled Hele-Shaw cell, J. Colloid Interface Sci. 462 (2016) 288–296. doi:https://doi.org/10.1016/j.jcis.2015.10.017.

[97] Palak, V. R. S. Parmar, D. Saha, R. Bandyopadhyay, Pattern selection in radial displacements of a confined aging viscoelastic fluid, JCIS Open 6 (2022) 100047. doi:10.1016/j.jciso.2022.100047.

[98] O. Praud, H. L. Swinney, Fractal dimension and unscreened angles measured for radial viscous fingering, Phys. Rev. E 72 (2005) 011406. doi:10.1103/PhysRevE.72.011406.

[99] F. Gallaire, P.-T. Brun, Fluid dynamic instabilities: theory and application to pattern forming in complex media, Philosophical Transactions of the Royal Society A: Mathematical, Physical and Engineering Sciences 375 (2093) (2017) 20160155. doi:10.1098/rsta.2016.0155.

[100] H. S. HELE-SHAW, The flow of water, Nature 58 (1489) (1898) 34–36. doi:10.1038/058034a0.

[101] S. Whitaker, Flow in porous media i: A theoretical derivation of darcy's law, Transport in Porous Media 1 (1) (1986) 3–25. doi:10.1007/BF01036523.

[102] P. G. Saffman, G. I. Taylor, The penetration of a fluid into a porous medium or Hele-Shaw cell containing a more viscous liquid, Proceedings of the Royal Society of London. Series A. Mathematical and Physical Sciences 245 (1242) (1958) 312–329. doi:10.1098/rspa.1958.0085.

[103] E. Lajeunesse, J. Martin, N. Rakotomalala, D. Salin, 3D instability of miscible displacements in a Hele-Shaw cell, Phys. Rev. Lett. 79 (1997) 5254–5257. doi:10.1103/PhysRevLett.79.5254.

[104] I. Bischofberger, R. Ramachandran, S. R. Nagel, Fingering versus stability in the limit of zero interfacial tension, Nat. Commun. 5 (1) (2014) 1–6. doi:10.1038/ncomms6265.

[105] R. X. Suzuki, F. W. Quah, T. Ban, M. Mishra, Y. Nagatsu, Experimental study of miscible viscous fingering with different effective interfacial tension, AIP Adv. 10 (11) (2020) 115219. doi:10.1063/5.0030152.

[106] L. Paterson, Radial fingering in a Hele-Shaw cell, Journal of Fluid Mechanics 113 (1981) 513–529. doi:10.1017/S0022112081003613.

[107] A. Eslami, S. Taghavi, Viscous fingering of yield stress fluids: The effects of wettability, Journal of non-Newtonian Fluid Mechanics 264 (2019) 25–47. doi:https://doi.org/10.1016/j.jnnfm.2018.12.007.

[108] C. Z. van Doorn, Dynamic behavior of twisted nematic liquid-crystal layers in switched fields, Journal of Applied Physics 46 (9) (1975) 3738–3745. doi:10.1063/1.322177.

[109] E. Corvera Poiré, M. Ben Amar, Finger behavior of a shear-thinning fluid in a Hele-Shaw cell, Phys. Rev. Lett. 81 (1998) 2048–2051. doi:10.1103/PhysRevLett.81.2048.

[110] A. Lindner, D. Bonn, J. Meunier, Viscous fingering in complex fluids, Journal of Physics: Condensed Matter 12 (8A) (2000) A477–A482. doi:10.1088/0953-8984/12/8a/366.

[111] M. Kawaguchi, K. Makino, T. Kato, Viscous fingering patterns in polymer solutions, Physica D: Nonlinear Phenomena 109 (3) (1997) 325–332. doi:https://doi.org/10.1016/S0167-2789(97)00069-9.

[112] N. Kagei, D. Kanie, M. Kawaguchi, Viscous fingering in shear-thickening silica suspensions, Physics of Fluids 17 (5) (2005) 054103. doi:10.1063/1.1894407.

[113] D. Li, Z. Yang, R. Zhang, R. Hu, Y.-F. Chen, Morphological patterns and interface instability during withdrawal of liquid-particle mixtures, J. Colloid Interface Sci. 608 (2022) 1598–1607. doi:10.1016/j.jcis.2021.10.115.

[114] S. H. Bittleston, J. Ferguson, I. A. Frigaard, Mud removal and cement placement during primary cementing of an oil well – laminar non-newtonian displacements in an eccentric annular Hele-Shaw cell, Journal of Engineering Mathematics 43 (2) (2002) 229–253. doi:10.1023/A:1020370417367.

[115] On the Instability of Cement-Fluid Interface and Fluid Mixing, Vol. Day 2 Thu, September 15, 2016 of SPE Deepwater Drilling and Completions Conference. doi:10.2118/180322-MS.

[116] A. Fall, N. Huang, F. Bertrand, G. Ovarlez, D. Bonn, shear-thickening of cornstarch suspensions as a reentrant jamming transition, Phys. Rev. Lett. 100 (2008) 018301. doi:10.1103/PhysRevLett.100.018301.

[117] A. J. Liu, S. R. Nagel, Jamming is not just cool any more, Nature 396 (6706) (1998) 21–22. doi:10.1038/23819.

[118] A. Fall, F. Bertrand, D. Hautemayou, C. Mezière, P. Moucheront, A. Lemaître, G. Ovarlez, Macroscopic discontinuous shear-thickening versus local shear

jamming in cornstarch, Phys. Rev. Lett. 114 (2015) 098301. doi:10.1103/PhysRevLett.114.098301.

[119] R. M. Brady, R. C. Ball, Fractal growth of copper electrodeposits, Nature 309 (5965) (1984) 225–229. doi:10.1038/309225a0.

[120] P. Bai, J. Li, F. R. Brushett, M. Z. Bazant, Transition of lithium growth mechanisms in liquid electrolytes, Energy Environ. Sci. 9 (2016) 3221–3229. doi:10.1039/C6EE01674J.

[121] Y. Cinar, A. Riaz, H. A. Tchelepi, Experimental Study of CO2 Injection Into Saline Formations, SPE Journal 14 (04) (2009) 588–594. doi:10.2118/110628-PA.

[122] W. Xu, J. Wang, F. Ding, X. Chen, E. Nasybulin, Y. Zhang, J.-G. Zhang, Lithium metal anodes for rechargeable batteries, Energy Environ. Sci. 7 (2014) 513–537. doi:10.1039/C3EE40795K.

[123] S. Gorell, G. Homsy, Theory of the optimal policy of oil recovery by secondary displacement processes., SIAM Journal on Applied Mathematics 43 (1) (1983) 79–98. doi:10.1137/0143007.

[124] F. M. Orr, J. J. Taber, Use of Carbon Dioxide in Enhanced Oil Recovery, Science 224 (4649) (1984) 563–569. doi:10.1126/science.224.4649.563.

[125] M. C. Marchetti, J. F. Joanny, S. Ramaswamy, T. B. Liverpool, J. Prost, M. Rao, R. A. Simha, Hydrodynamics of soft active matter, Rev. Mod. Phys. 85 (2013) 1143–1189. doi:10.1103/RevModPhys.85.1143.

[126] C. Bechinger, R. Di Leonardo, H. Löwen, C. Reichhardt, G. Volpe, G. Volpe, Active particles in complex and crowded environments, Rev. Mod. Phys. 88 (2016) 045006. doi:10.1103/RevModPhys.88.045006.

[127] S. Henkes, Y. Fily, M. C. Marchetti, Active jamming: Self-propelled soft particles at high density, Phys. Rev. E 84 (2011) 040301. doi:10.1103/PhysRevE.84.040301.

[128] L. Berthier, J. Kurchan, Non-equilibrium glass transitions in driven and active matter, Nature Physics 9 (5) (2013) 310–314. doi:10.1038/nphys2592.

[129] L. Berthier, Nonequilibrium glassy dynamics of self-propelled hard disks, Phys. Rev. Lett. 112 (2014) 220602. doi:10.1103/PhysRevLett.112.220602.

[130] R. Ni, M. A. C. Stuart, M. Dijkstra, Pushing the glass transition towards random close packing using self-propelled hard spheres, Nature Communications 4 (1) (2013) 2704. doi:10.1038/ncomms3704.

[131] W. T. Kranz, M. Sperl, A. Zippelius, Glass transition for driven granular fluids, Phys. Rev. Lett. 104 (2010) 225701. doi:10.1103/PhysRevLett.104.225701.

[132] R. Mandal, P. J. Bhuyan, M. Rao, C. Dasgupta, Active fluidization in dense glassy systems, Soft Matter 12 (2016) 6268–6276. doi:10.1039/C5SM02950C.

# Chapter 2

# Materials and Methods

## 2.1 Introduction

Chapter 2 describes sample preparation protocols and experimental techniques employed in this thesis. Aqueous suspensions of granular cornstarch particles and colloidal synthetic clay particles are prepared, and the displacements of these suspensions by a Newtonian fluid are studied in a confined geometry using video imaging. Chemically active Janus polystyrene (PS) particles are synthesized and their influence on the dynamics of passive PS particles in a dense binary mixture is reported. Commercial stress-controlled rheometers are used to characterize the dense suspensions used in this thesis. A brief description of measuring geometries and rheological measurements is provided. A custom-made quasi-two-dimensional radial Hele-Shaw (HS) cell setup is used to study the interfacial instabilities formed at the interface between a Newtonian fluid and a viscoelastic fluid. Bright-field microscopy is used to characterize the synthesized Janus particles. Confocal microscopy is used to study the dynamics of passive PS particles in the presence of small quantities of active PS particles.

## 2.2 Sample preparation

### 2.2.1 Cornstarch suspensions

Cornstarch powder and cesium chloride (ReagentPlus®, 99.9%) are procured from Sigma-Aldrich. Cornstarch suspensions of concentrations in the range of 30 wt.% to 42 wt.% are prepared by gradually adding cornstarch powder to a 55 wt.% aqueous cesium chloride (CsCl) solution to ensure density matching of the cornstarch particles having a density of 1.59 g/cm$^3$ [1, 2]. The samples are stirred thoroughly using a magnetic stirrer (1 MLH, Remi Equipments Ltd., Mumbai), followed by ultra-sonication (USC 400, ANM Industries Pvt. Ltd.) for 15 minutes. The sample is left undisturbed for 24 hours to ensure uniform hydration of the cornstarch grains [3]. These samples are re-stirred and re-sonicated before each experiment to ensure sample homogeneity.

### 2.2.2 Laponite® suspensions

Hygroscopic Laponite® XLG powder (BYK additives Inc.) is baked in an oven at 120°C for 18-20 hours prior to sample preparation. To prepare an aqueous Laponite suspension, dried Laponite powder is added to 50 mL double distilled water (Millipore Corp., resistivity 18.2 MΩ.cm). Granules of the Laponite powder are added to water, and the mixture is stirred continuously and vigorously for 45 minutes using a magnetic stirrer (1 MLH, Remi Equipments Ltd., Mumbai) at room temperature (25°C). The resulting homogeneous suspension is filtered through a syringe filter (Millex®, Sigma Aldrich) having pore size 0.45 $\mu$m.

### 2.2.3 Synthesis of chemically active Janus particles

Polystyrene (PS) microspheres with a mean diameter 2.07 ± 0.15 $\mu$m are procured from Bangs Laboratories Inc. and are used in preparing suspensions of Janus particles. 1 wt.% polystyrene microspheres, procured from Bangs Laboratories Inc.,

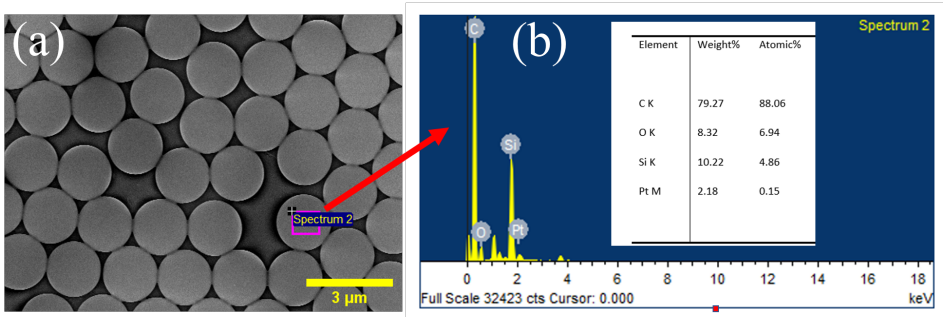



**Fig. 2.1:** Scanning electron microscope image of platinum coated polystyrene (Janus) particles of mean diameter 2.07 ± 0.15 $\mu$m (procured from Bangs Laboratories Inc.) on a glass substrate. (b) A spectrum obtained from Energy dispersive X-ray analysis (EDAX) of platinum coated PS particles. Inset of (b) shows the elemental composition of Janus PS particles as extracted from EDAX data by probing the region within the pink box shown in (a)

are further diluted with 1:1 ethanol: Milli-Q water (Millipore Corp., resistivity 18.2 MΩ.cm) mixture to prepare 0.8 wt.% stock suspension. We come to this concentration by trial method. Glass slides are ultrasonicated in acetone, ethanol and Milli-Q water respectively for 15 minutes and then immersed in piranha solution (a mixture of 3 : 1 sulfuric acid and hydrogen peroxide) for one hour. All glass slides are rinsed with Milli-Q water and dried in a hot air oven, followed by nitrogen purging. This procedure ensures that the glass slides are not contaminated. A monolayer of the prepared dilute suspension of PS particles over these clean microscope glass slides is achieved by spin coating using an EZspin-A1 Apex Instruments spin coater. The glass slide is rotated at 1000 rpm for 40 s with an acceleration time of 5 s. A 5 nm thick layer of platinum (Pt) is deposited on the top surface of the PS-coated glass slide by using a vapor deposition technique in vacuum [4]. In this process, Pt is evaporated onto the PS-coated slides for 50 s at 20 mA current using Quorum Q150RS sputter coater. Figure 2.1(a) shows a scanning electron microscope image of a dense monolayer of PS particles on a glass microscope slide. An ULTRA-PLUS field effect scanning electron microscope from Carl Zeiss is used to visualize the monolayer of Pt-coated PS particles. Figure 2.1(b) shows the energy spectrum obtained using energy dispersive X-ray analysis (EDAX, Oxford Instruments). The

elemental composition of a Janus particle, analyzed by EDAX for the region enclosed by the pink box in Fig. 2.1(a), is shown in the inset of Fig. 2.1(b). The half Pt-coated PS particles are detached from the glass slide using a polytetrafluoroethylene (Goodfellow) sheet of thickness 200 $\mu$m and then dispersed in Milli-Q water. The stock suspension of Janus particles is centrifuged at 6000 rpm for 25 minutes in a Spinwin MC-02 microcentrifuge machine. The supernatant water is removed and the sample is vacuum dried to obtain a closely packed suspension [5]. A 1 wt.% aqueous suspension of Janus particles is prepared by diluting the closely packed suspension obtained during the previous stage with an appropriate amount of Milli-Q water.

### 2.2.4 Binary mixture of passive polystyrene particles

A binary mixture of passive fluorescent polystyrene (PS) particles is prepared using small particles (dyed with flash red, Bangs Laboratories Inc.) of diameter $d_S = 2.07 \pm 0.15$ $\mu$m and large particles (dyed with envy green, Bangs Laboratories Inc.) of diameter $d_L = 3.87 \pm 0.15$ $\mu$m. 1 wt.% aqueous stock suspensions of PS particles

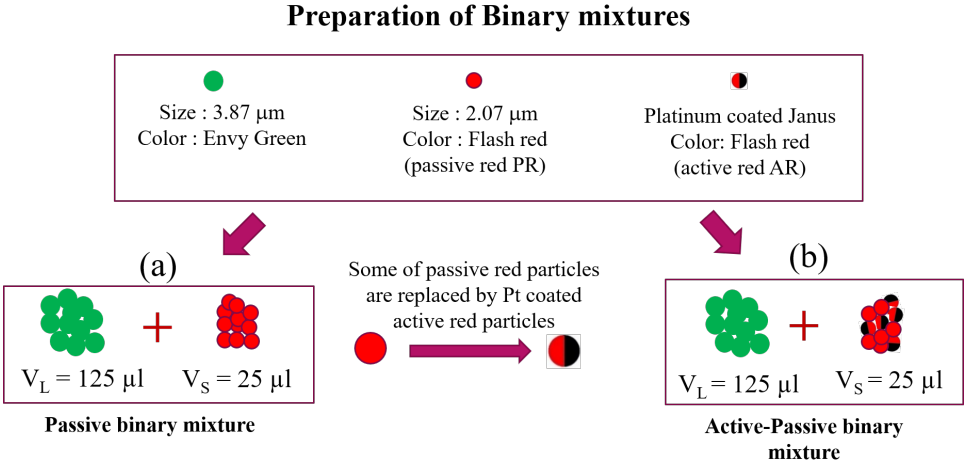



**Fig. 2.2:** Schematic diagram for the preparation of binary mixtures of fluorescent PS particles. (a) shows the composition of a passive binary mixture and (b) shows the composition of an active binary mixture. $V_L$ and $V_S$ refer to the volumes of suspensions comprising large and small particles used for preparing the binary mixtures.

are used in the preparation of the binary mixtures. The mixture is labelled by the particle size ratio $d_L/d_S$, where $d_L$ and $d_S$ are the daimeters of large and small particles, and particle number ratio $N_L/N_S$, where $N_L$ and $N_S$ refer to the numbers of large and small particles respectively. For the experiments reported in this thesis, a size ratio $d_L/d_S = 1.87$ and number ratio $N_L/N_S = 0.76$ are chosen to prevent crystallization of the binary mixture. A stock suspension is prepared by mixing large and small particles respectively of volumes $V_L = 125$ $\mu$L and $V_S = 25$ $\mu$L respectively. Figure 2.2(a) shows a schematic illustration of the preparation procedure of passive binary mixtures. Finally, we ensure the preparation of a homogeneous sample by sonicating the mixture for 15 minutes and then centrifuging it for 25 minutes at 6000 rpm in a Spinwin MC-02 microcentrifuge machine. After centrifugation, the supernatant water is discarded and the sample is vacuum dried. A binary mixture of $\phi = 0.57$ is prepared by diluting the binary mixtures of PS particles with a 1:1 $D_2O : H_2O$ solution. The $D_2O : H_2O$ solution ensures density matching of PS particles with the suspension medium.

### 2.2.5 Binary mixture of active and passive polystyrene particles

Some of the passive PS red particles ($d_S = 2.07 \pm 0.15$ $\mu$m) in the binary mixture (section 2.2.4) are replaced by active PS particles (section 2.2.3) to produce a hybrid binary mixture of active and passive particles. Volume of the small red particles in the binary mixture is defined as $V_S = V_{PR}+V_{AR}$, where $V_{PR}$ and $V_{AR}$ are the volumes of passive red particles and active red particles respectively. In this thesis, the number of active PS particles in the binary mixture is controlled by systematically changing the $V_{AR}$ (Fig. 2.2(b)). The prepared mixture is centrifuged and vacuum dried by following the same protocols as described in section 2.2.4. The closely packed dried sample is further diluted with a 1:1 $D_2O : H_2O$ solution to prepare a binary mixture of volume fraction $\phi = 0.57$. The total volume fraction of the binary mixtures is kept fixed in this thesis. These Pt-coated active PS particles in the

suspension self propel in the presence of hydrogen peroxide $H_2O_2$ due to Pt-induced catalytic decomposition of $H_2O_2$ molecules into water and oxygen molecules [4]. The decomposition reaction as follows:

$$2H_2O_2 \xrightarrow{Pt} 2H_2O + O_2 \tag{2.1}$$

## 2.3 Experimental techniques

### 2.3.1 Rheology

Rheology is the study of flow and deformation of materials [6, 7]. Rheological measurements in this thesis are performed using stress-controlled modular compact rheometers Anton Paar MCR 501 and MCR 702. The key components of the MCR series rheometer are shown in Fig. 2.3(a). MCR rheometers are equipped with an air-bearing-supported and electronically commutated (EC) synchronous DC motor [8]. The motor achieves torque measurements as low as $5.0 \times 10^{-1}$ nN.m with a resolution of $1.0 \times 10^{-2}$ nN.m. A normal force transducer in the air-bearing unit enables the measurement of normal forces. Normal forces in the range between $1.0 \times 10^{-2}$ mN.m and $3.0 \times 10^{2}$ mN.m are measured with a resolution of $1.0 \times 10^{-2}$ nN.m [8]. An optical encoder, calibrated to make precise measurements of the strain response, can measure angular deflections with a resolution $< 1$ $\mu$ rad [8].

Data acquisition is achieved using Rheoplus and RheoCompass softwares respectively for the MCR 501 and MCR 702 rheometers and are provided by the manufacturer. For the plate-plate and cone-plate sample geometries, a Peltier unit is used to control sample temperature between 1°C and 180°C with temperature stability of $\pm$ 0.1°C. Viscotherm VT2, a water circulation unit, controls the temperature of the sample in the double gap and cylinder geometries in the range between 5°C and 80°C with temperature stability $\pm$ 0.1°C. Different measuring geometries are used in this work depending on the mechanical properties of the samples. The measuring geometries are attached to the rotating rod while controlling the gap size

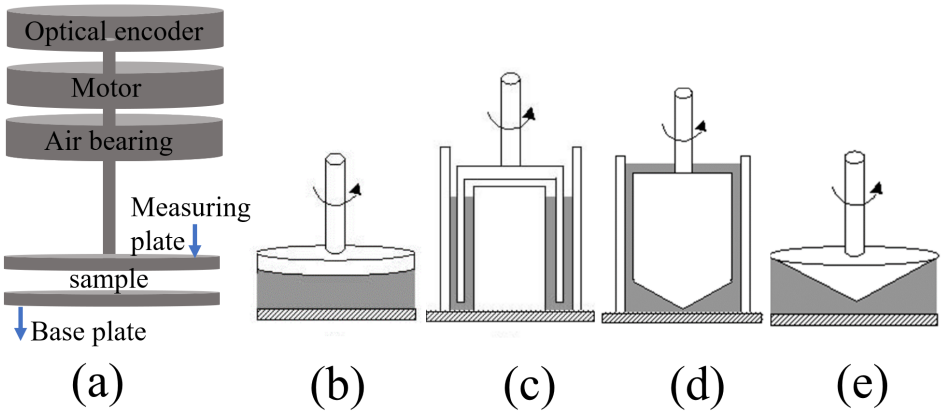



**Fig. 2.3:** (a) Schematic diagram of key components of Anton Paar MCR rheometer. Schematic diagrams of (b) parallel plate geometry, (c) double gap geometry, (d) concentric cylinder geometry and (e) cone and plate geometry. The images (b-e) are adapted from [8].

by TruGap$^{TM}$ technology, provided with the rheometer. The different measuring geometries are described below:

### Parallel plate geometry

A parallel plate PP50 geometry is used to perform rheological measurements of a sample of high concentration or viscosity. The parallel plate geometry (PP50) comprises two parallel plates with an external diameter 49.974 mm (Fig. 2.3(b)). The required volume of sample for this geometry at a plate gap 1 mm is 1.96 mL.

### Double gap geometry

The double-gap geometry DG26.7/Q1 comprises a co-axially arranged rotating inner hollow cylinder and cylindrical cup assembly (Fig. 2.3(c)). This geometry is suitable for low viscosity fluids, as it is designed to increase the total surface area of the sample that is in contact, thereby maximizing the viscous drag on the rotating inner cylinder. The gap between these two cylinders is 1.886 mm with an effective length of 40 mm and the geometry requires a sample volume of 3.8 mL.

### Concentric cylinder geometry

As illustrated in Fig. 2.3(d), the concentric cylinder (CC) geometry consists of a co-axially oriented rotating cylindrical bob and cylindrical cup. Samples of intermediate viscosity or concentration are often studied using CC geometry. The CC17 geometry has a gap of 0.71 mm and an effective length of 24.99 mm. Each experimental run requires a sample volume of 4.72 mL.

### Cone and plate geometry

Rheological measurements of high viscosity materials, such as pastes, gels, and dense suspensions, are performed using the cone and plate (CP) geometry. A revolving inverted cone is positioned above a stationary flat plate in the CP geometry (Fig. 2.3(e)). The sample is loaded between the cone and plate. The cone and plate CP-25 geometry that we employed for our rheological experiments has a measuring gap of $d = 0.048$ mm, a cone radius of $r_c = 12.49$ mm, a cone angle $\alpha = 0.979$ and requires sample volume 0.07 mL in each measurement. Further details about the different geometries can be found in [8].

### Application of rheometer

The viscoelastic samples investigated in this thesis have been studied in the Anton Paar MCR series rheometers using both rotational and oscillatory measurements.

### Rotational measurements

In a rotational experiment, a shear strain or shear rate is applied to the viscoelastic sample along a specific direction. The shear flow of the sample is assessed in terms of its shear stress ($\sigma$) or viscosity ($\eta$). In this thesis, rotational experiments have been employed to examine the shear-thinning and shear-thickening properties of viscoelastic materials such as aqueous cornstarch suspensions and Laponite suspensions under applied shear rates. Glycerol-water mixtures having different glycerol

concentrations have been used as a Newtonian fluid in many of our experiments. The Newtonian behavior of glycerol-water mixtures is confirmed from Fig. 2.4(a) which shows that the measured viscosities are independent of shear rate. Glycerol and water are miscible in all proportions and their viscosity changes negligibly over the range of shear rates explored, thereby highlighting the Newtonian flow behavior of the mixture. In contrast, as shown in Fig. 2.4(b), the viscosity of a 35 wt.% aqueous cornstarch suspension at 25°C decreases with applied shear rates ($\dot{\gamma} \leq 35.2\ \mathrm{s}^{-1}$), thereby depicting its shear-thinning behavior. When the shear rate $\dot{\gamma}$ lies above a critical shear rate $\dot{\gamma}_c = 35.2\ \mathrm{s}^{-1}$, viscosity of the cornstarch suspension increases with applied shear rates, thereby indicating shear-thickening behavior of the suspension.

## Oscillatory measurements

In oscillatory tests, a sinusoidal strain $\gamma' = \gamma \sin \omega t$ is applied and the stress response $\sigma(t) = \gamma' G^*(\omega)$ is measured. Here, $G^*(\omega)$ is the complex shear modulus [6] and is expressed in terms of the elastic or storage modulus $G'$ and the viscous or loss modulus $G''$ as follows:

$$G^*(\omega) = G'(\omega) + iG''(\omega) \tag{2.2}$$

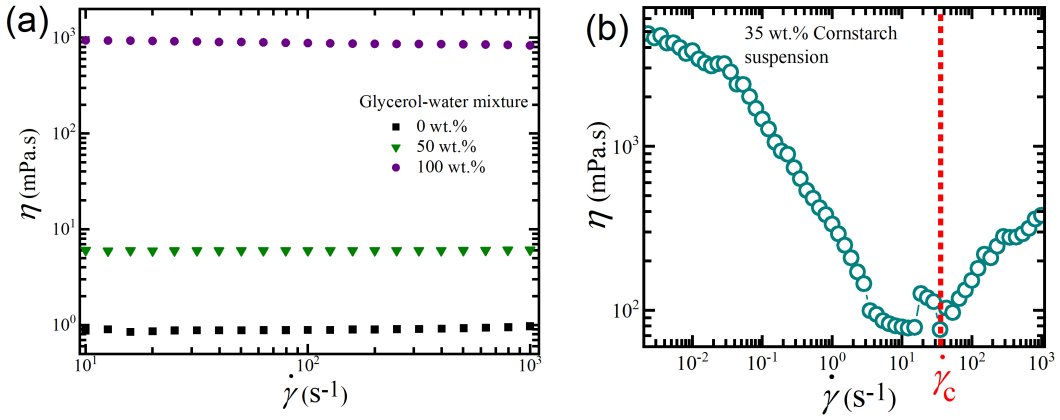



**Fig. 2.4:** (a) Viscosities of glycerol-water mixtures *vs*. shear rate ($\dot{\gamma}$) for different weight percent (wt.%) of glycerol. (b) Viscosity *vs*. shear rate ($\dot{\gamma}$) of a 35 wt.% aqueous cornstarch suspension. All the measurements were made at room temperature (25°C).

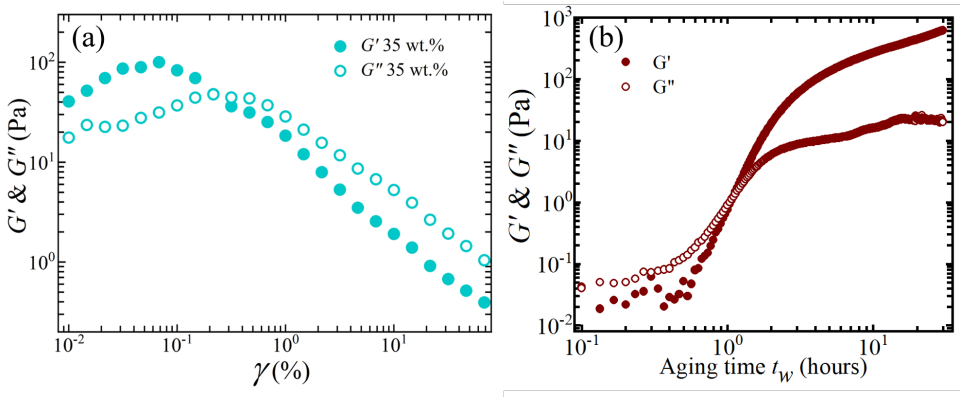



**Fig. 2.5:** (a) Elastic modulus $G'$ (solid symbols) and viscous modulus $G''$ (open symbols) of 35 wt.% cornstarch suspension as a function of strain amplitude $\gamma$. (b) Evolution of elastic modulus $G'$ and viscous modulus $G''$ for a 3.25% w/v Laponite suspension with increasing aging time $t_w$. All tests are performed at room temperature (25°C)

We discuss below the oscillatory tests used in this thesis.:

### Strain amplitude sweep

In a strain sweep experiment, the viscoelastic moduli ($G'$ and $G''$) are measured at a constant oscillatory frequency $\omega$ while varying the amplitude of the applied oscillatory strain $\gamma$. Figure 2.5(a) shows an amplitude sweep measurement for a 35 wt.% aqueous cornstarch suspension at room temperature (25°C). At very low strains $G'$ is practically insensitive to applied strain and $G' > G''$, thereby indicating solid-like behavior. The observed decrease in viscoelastic moduli at higher strain values, with $G'' > G'$, signifies viscoelastic-liquid behavior of the suspension.

### Time sweep

In a time sweep experiment, the spontaneous evolution of the viscoelastic moduli ($G'$ & $G''$) is recorded under an oscillatory strain of constant amplitude $\gamma$ and a constant angular frequency $\omega$. The amplitude of the applied strain is small enough that no underlying sample microstructures are perturbed during the measurement. These tests are usually employed to study the rheological responses of viscoelastic materials exhibiting aging dynamics. Figure 2.5(b) shows the elastic ($G'$) and viscous ($G''$)

moduli of a 3.25 wt.% aqueous Laponite suspension that is known to exhibit physical aging [9–13]. The data is acquired as a function of aging time $t_w$ at an applied strain amplitude 0.5 % and angular frequency 1 rad/s. In these measurements, the freshly prepared Laponite suspension is first loaded in the geometry and shear melted at a high shear rate of 500 $s^{-1}$ to remove any memory of the sample loading process. The time at which shear application is stopped and the sample is allowed to evolve spontaneously in the rheological experiments is noted as aging time $t_w = 0$.

### 2.3.2 Hele-Shaw Cell

Intricate patterns in the branching of trees, sand ripples, the formation of river networks, the branching morphogenesis in vertebrate airways, and in geological contexts [14] are common in nature. A salient and visually striking example of complex patterns in fluids is viscous fingers which form during the displacement of a more viscous fluid by a less viscous fluid [15–21]. Given the experimental difficulties in tracking and obtaining useful information about flow in a porous medium, the quasi-two-dimensional Hele-Shaw (HS) cell [22] geometry, named after the English mechanical and automobile engineer Henry Selby Hele-Shaw, is extensively used as

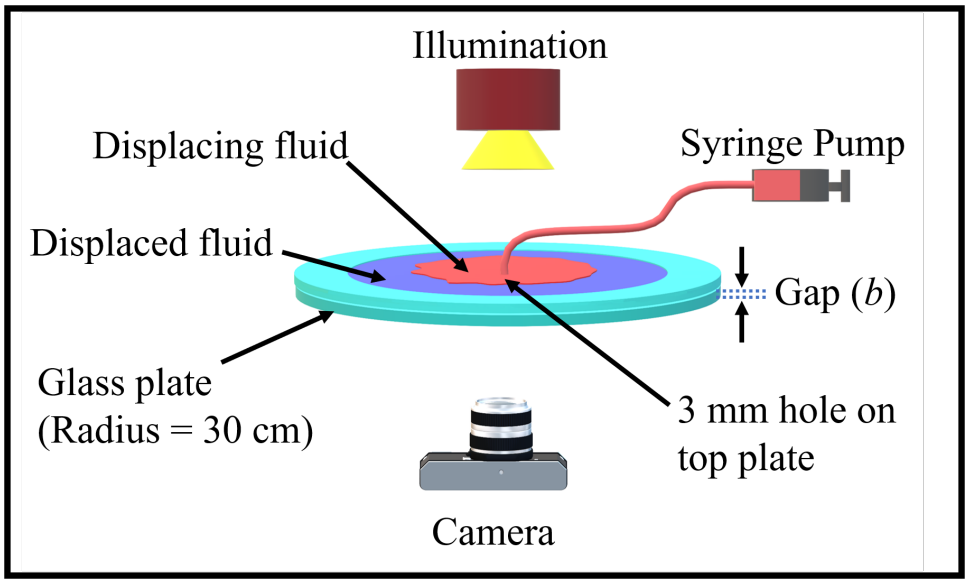



**Fig. 2.6:** Schematic illustration of a radial Hele-Shaw cell.

a more straightforward option in the study of interfacial patterns. The HS cell is a setup with a typically tiny gap between closely spaced parallel plates. Since the flow in the Hele-Shaw geometry is averaged across the gap, the resultant flow can be described by Darcy's law [23]. While a conventional Hele-Shaw cell is based on the displacement of a more viscous fluid by a less viscous one under high pressure, experimentalists have also studied viscous fingering in modified Hele-Shaw cells. In lifting Hele-Shaw cell experiments, the air penetrating into a confined layer of a fluid causes the latter to undergo stretch flow, thereby giving rise to interfacial instabilities [24]. A rotating Hele-Shaw cell is a special example of a confined geometry where the centrifugal force and density difference between two fluids control the morphology of the interfacial pattern [25]. Flow anisotropies in the Hele-Shaw cell can be introduced by different means, such as engraving a six-fold symmetric lattice of channels on the cell [26] or by stretching a piece of cloth across the lower plate [27].

When a shear thinning or shear thickening complex fluid is displaced in a confined HS cell, interfacial instabilities having very distinct morphologies are reported to arise. In this thesis, the impact of shear and time-dependent rheology of a displaced outer viscoelastic fluid on the morphology of interfacial patterns between the displaced and displacing fluids in a conventional Hele-Shaw cell is investigated. The Hele-Shaw cell used in the present thesis comprises two circular glass plates of thickness 10 mm and diameter 60 cm, thereby ensuring good mechanical stability (Fig. 2.6). Teflon spacers are used to ensure a uniform gap between the plates. The outer fluid is first injected through a 3 mm hole drilled on the top plate of the HS cell with a syringe pump (NE-8000, New Era Pump Systems, USA). The second fluid is then injected with a controlled flow rate $q$ through the same hole. The whole setup is placed on a mechanically stable table and the interfacial patterns are recorded using a D5200 DSLR camera (set up below the cell, Fig. 2.6).

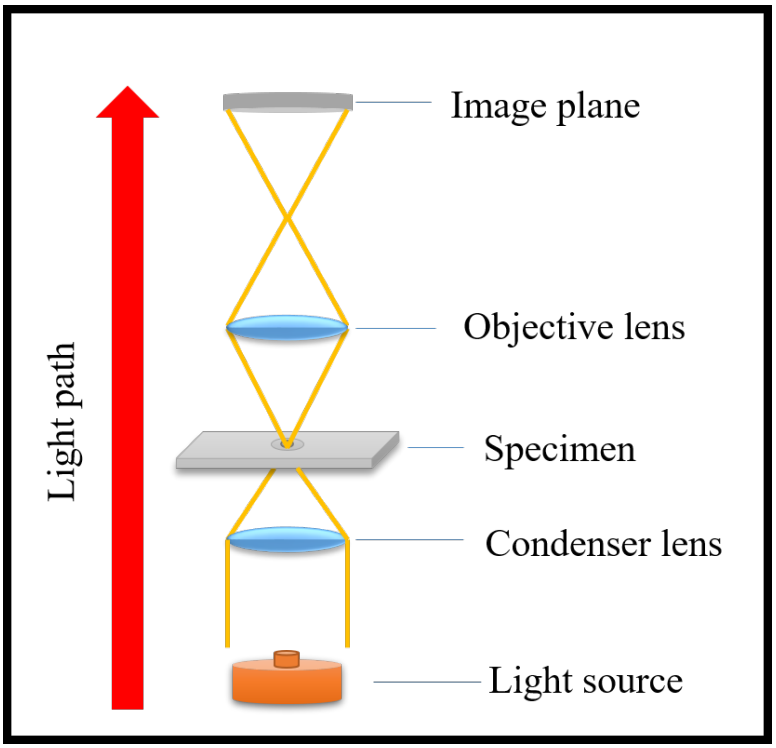



**Fig. 2.7:** Schematic diagram of a bright field microscope setup.

### 2.3.3 Bright field microscope

A bright field microscope (BFM) is the simplest optical microscope that generates dark images of the sample over a bright background [28]. A contrast in the sample arises due to absorption of some of the transmitted light from its dense regions. Figure 2.7 shows the schematic diagram of the BFM. The key components of BFM are objective lens, eyepiece lens/detector, moving stage for the specimen, condenser lens with an aperture diaphragm, and light source [29]. A condenser lens directs light from the source onto the specimen. The aperture diaphragm of the condenser lens controls and focuses light on the specimen. The light after passing through the specimen, is captured by an objective lens placed above the stage. The image, enlarged by the objective is recorded on the computer through a CCD detector. The alignment of the condenser, objective and eyepiece lens is very important to get a high quality image of the sample.

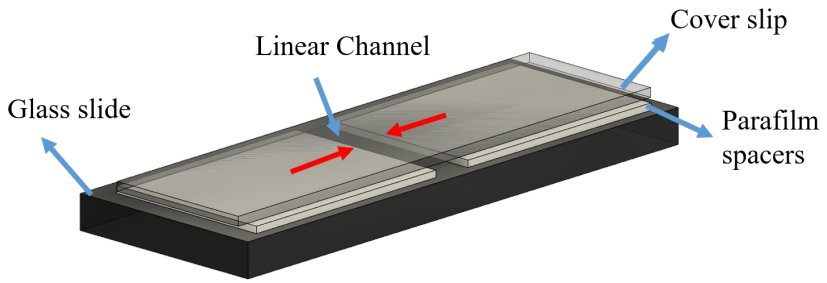



**Fig. 2.8:** Schematic diagram of a linear microchannel.

## Linear microchannel

The microchannel used here (Fig. 2.8) for Janus experiments is of width 3 mm, comprising a microscopic glass slide and a number 1 coverslip that are separated by parafilm of thickness 100 $\mu$m. All the glass slides and coverslips are procured from Blue Star. All the glassware used are sonicated in 1.5% v/v Hellmanex III solution at 70°C followed by rinsing with Milli-Q water. The washed glassware are then dried in a hot oven at 60°C for one hour. It is important to follow this cleaning procedure to ensure that particles do not stick to the coverslip or the glass surfaces. The parafilm is heated using a hot plate to attach it to the glass slide.

### 2.3.4 Confocal microscope

Confocal microscopy has been used in this thesis to obtain high-resolution optical images [30]. A unique feature of a confocal microscope is its ability to perform optical sectioning, by which background information from regions away from the focal plane is discarded and in-focus images of the thick samples are recorded. It allows the three-dimensional reconstruction of a complex topological object by performing point by point scanning at different depths of the sample. Figure 2.9 shows a schematic illustration of a confocal microscope. The key components of a confocal microscope are a laser excitation source, two pinhole apertures, a dichromatic mirror, a scanning unit, an objective lens, and a detector (photomultiplier tube) [31].

The collimated laser beam from the excitation source passes through a pinhole aperture and gets reflected by the dichromatic mirror. The reflected light is focused by an objective lens on the specimen. A three-dimensional image of the specimen is constructed by scanning across it using oscillating mirrors present in the scanning unit. After excitation of the fluorescent sample, the re-emitted secondary fluorescence passes through the dichromatic mirror and focuses on the pinhole aperture close to the photomultiplier detector, transforming the light signal into an electrical one that is recorded by a computer. The out-of-focus light rays arising due to emission from points above and below the focal plane of the objective are significantly reduced by the pinhole aperture, thereby improving the contrast of the resulting image.

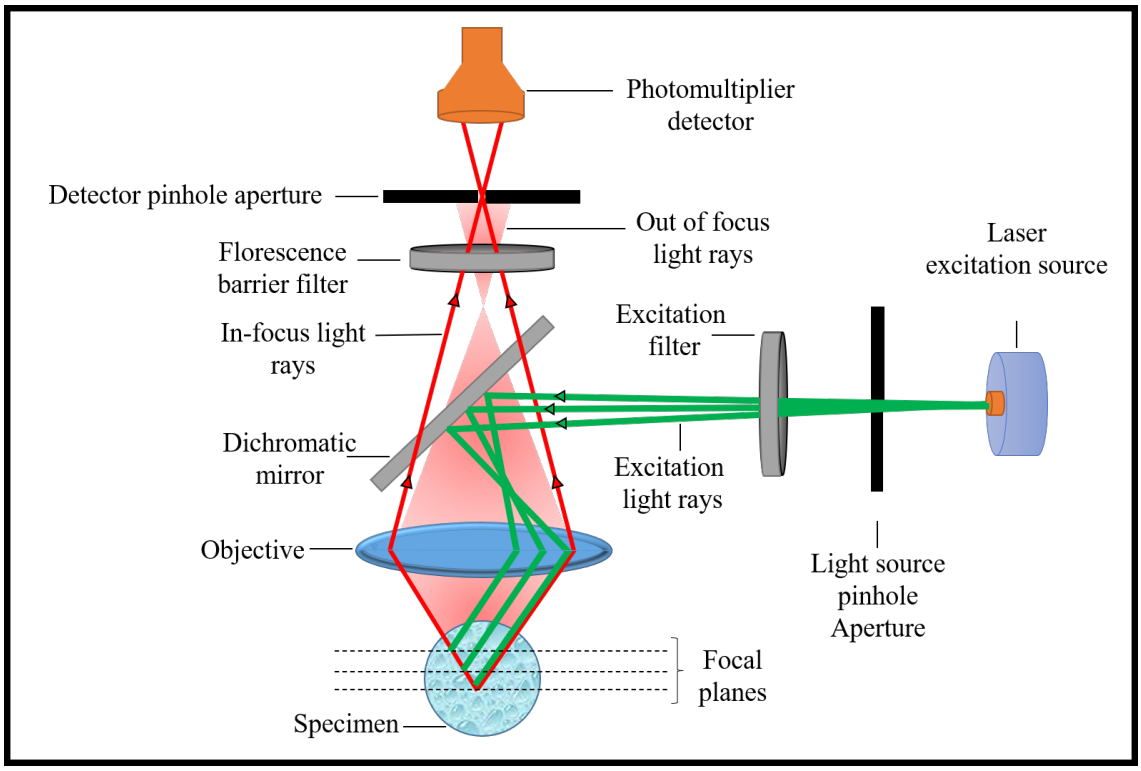



**Fig. 2.9:** Schematic diagram of a confocal microscope setup.

# References


[1] F. S. Merkt, R. D. Deegan, D. I. Goldman, E. C. Rericha, H. L. Swinney, Persistent holes in a fluid, Phys. Rev. Lett. 92 (2004) 184501. doi:10.1103/PhysRevLett.92.184501.

[2] E. Brown, H. M. Jaeger, Dynamic jamming point for shear thickening suspensions, Phys. Rev. Lett. 103 (2009) 086001. doi:10.1103/PhysRevLett.103.086001.

[3] N. C. Crawford, L. B. Popp, K. E. Johns, L. M. Caire, B. N. Peterson, M. W. Liberatore, Shear thickening of corn starch suspensions: Does concentration matter?, Journal of Colloid and Interface Science 396 (2013) 83–89. doi:https://doi.org/10.1016/j.jcis.2013.01.024.

[4] J. R. Howse, R. A. L. Jones, A. J. Ryan, T. Gough, R. Vafabakhsh, R. Golestanian, Self-motile colloidal particles: From directed propulsion to random walk, Phys. Rev. Lett. 99 (2007) 048102. doi:10.1103/PhysRevLett.99.048102.

[5] P. N. Pusey, W. van Megen, Observation of a glass transition in suspensions of spherical colloidal particles, Phys. Rev. Lett. 59 (1987) 2083–2086. doi:10.1103/PhysRevLett.59.2083.

[6] C. W. Macosko, Rheology: Principles, Measurements, and Applications, VCH Publishes, New York, 1994.

[7] H. Barnes, J. Hutton, K. Walters, An Introduction to Rheology, Rheology Series, Elsevier Science, 1989.

[8] Anton Paar Mcr 702 users manual, https://www.anton-paar.com/in-en/.

[9] H. V. Damme, E. Lemaire, From Flow to Fracture and Fragmentation in Colloidal Media, In: J.C. Charmet, S. Roux, E. Guyon (Eds.), Disorder and Fracture., Springer, Boston, MA, 1990, pp. 83–104. doi:10.1007/978-1-4615-6864-3_6.

[10] F. Bergaya, G. Lagaly, Handbook of Clay Science: Part A Fundamentals, 2nd ed., Vol. 5A, Elsevier, Amsterdam, 2013.

[11] R. Bandyopadhyay, D. Liang, H. Yardimci, D. A. Sessoms, M. A. Borthwick, S. G. J. Mochrie, J. L. Harden, R. L. Leheny, Evolution of Particle-Scale Dynamics in an Aging Clay Suspension, Phys. Rev. Lett. 93 (2004) 228302. doi:10.1103/PhysRevLett.93.228302.

[12] C. Misra, V. T. Ranganathan, R. Bandyopadhyay, Influence of medium structure on the physicochemical properties of aging colloidal dispersions investigated using the synthetic clay Laponite®, Soft Matter 17 (2021) 9387–9398. doi:10.1039/D1SM00987G.

[13] M. Delhorme, B. Jönsson, C. Labbez, Monte Carlo simulations of a clay inspired model suspension: the role of rim charge, Soft Matter 8 (2012) 9691–9704. doi:10.1039/C2SM25731A.

[14] F. Gallaire, P.-T. Brun, Fluid dynamic instabilities: theory and application to pattern forming in complex media, Philosophical Transactions of the Royal Society A: Mathematical, Physical and Engineering Sciences 375 (2093) (2017) 20160155. doi:10.1098/rsta.2016.0155.

[15] P. G. Saffman, G. I. Taylor, The penetration of a fluid into a porous medium or Hele-Shaw cell containing a more viscous liquid, Proc. Math. Phys. Eng. Sci. 245 (1242) (1958) 312–329. doi:10.1098/rspa.1958.0085.

[16] G. M. Homsy, Viscous fingering in porous media, Annual Review of Fluid Mechanics 19 (1) (1987) 271–311. doi:10.1146/annurev.fl.19.010187.001415.

[17] L. Paterson, Radial fingering in a Hele-Shaw cell, J. Fluid Mech. 113 (1981) 513–529. doi:10.1017/S0022112081003613.

[18] T. T. Al-Housseiny, P. A. Tsai, H. A. Stone, Control of interfacial instabilities using flow geometry, Nature Physics 8 (10) (2012) 747–750. doi:10.1038/nphys2396.

[19] J.-D. Chen, Growth of radial viscous fingers in a Hele-Shaw cell, J. Fluid Mech. 201 (1989) 223–242. doi:10.1017/S0022112089000911.

[20] D. Bensimon, L. Kadanoff, S. Liang, B. Shraiman, C. Tang, Viscous flows in two dimensions, Reviews of Modern Physics 58 (4) (1986) 977–999. doi:10.1103/RevModPhys.58.977.

[21] S. A. Setu, I. Zacharoudiou, G. J. Davies, D. Bartolo, S. Moulinet, A. A. Louis, J. M. Yeomans, D. G. A. L. Aarts, Viscous fingering at ultralow interfacial tension, Soft Matter 9 (2013) 10599–10605. doi:10.1039/C3SM51571K.

[22] H. S. HELE-SHAW, The flow of water, Nature 58 (1489) (1898) 34–36. doi:10.1038/058034a0.

[23] S. Whitaker, Flow in porous media i: A theoretical derivation of darcy's law, Transport in Porous Media 1 (1) (1986) 3–25. doi:10.1007/BF01036523.

[24] S. Roy, S. Tarafdar, Patterns in the variable Hele-Shaw cell for different viscosity ratios: Similarity to river network geometry, Phys. Rev. E 54 (1996) 6495–6499. doi:10.1103/PhysRevE.54.6495.

[25] L. Carrillo, F. X. Magdaleno, J. Casademunt, J. Ortín, Experiments in a rotating Hele-Shaw cell, Phys. Rev. E 54 (1996) 6260–6267. doi:10.1103/PhysRevE.54.6260.

[26] Q. Zhang, A. Amooie, M. Z. Bazant, I. Bischofberger, Growth morphology and symmetry selection of interfacial instabilities in anisotropic environments, Soft Matter 17 (2021) 1202–1209. doi:10.1039/D0SM01706J.

[27] M. Ben Amar, R. Combescot, Y. Couder, Viscous fingering with adverse anisotropy: A new saffman-taylor finger, Phys. Rev. Lett. 70 (1993) 3047–3050. doi:10.1103/PhysRevLett.70.3047.

[28] Microscope, Bright Field, John Wiley & Sons, Ltd, 2020, Ch. 238, pp. 1275–1279. doi:https://doi.org/10.1002/9781119288190.ch238.

[29] Leica TCS SP8 bright field microscopy users manual, https://www.leica-microsystems.com/.

[30] J. B. Pawley, Handbook of Biological Confocal Microscopy, Springer, New York, 2006.

[31] Leica TCS SP8 confocal microscopy users manual, https://www.leica-microsystems.com/.

# Chapter 3

# Emergent patterns and stable interfaces during radial displacement of a viscoelastic fluid

## 3.1 Introduction

Intricate patterns in the branching of trees, the formation of river networks and the branching morphogenesis in vertebrate airways are common in nature. While patterns arise from a system's need to optimize its function, a complete understanding of the mechanisms of their growth and evolution remains elusive. A salient and visually striking example of complex patterns in fluids is the viscous fingers that form during the displacement of a more viscous fluid by a less viscous fluid [1–7]. As discussed in Chapter 1, interfacial patterns resulting from the displacement of one Newtonian fluid by another in a Hele-Shaw cell were reported to be sensitive to the viscosity contrast between the fluid pair [8, 9]. A transition from a fractal growth regime (similar to that reported by Saffman and Taylor [1]) to a stable regime (as reported by Lajeunesse *et al.* [8]) was seen as $\eta_{in}/\eta_{out}$ was increased. Here, $\eta_{in}$ and $\eta_{out}$ are the viscosities of the displacing (inner) and displacing (outer) fluids. In a more recent study, Sharma *et al.* [10] have experimentally identified the transition

from a stable to an unstable interface on a parameter space map of viscosity ratio and Peclet number during radial displacement of miscible Newtonian fluids. Despite these prominent works, physical descriptions of viscous fingering instabilities may be compounded by other factors such as fluid rheology, nonlinear branching effects, and long term stability of patterns.

In the context of existing literature on miscible viscous fingering in Hele-Shaw cells, the present chapter addresses the role of relaxation processes in a radially displaced fluid on the interfacial instability. We show that the kinetics of the process is not merely a function of viscosity mismatch between the two fluids, but also the elasticity of a fluid. Moreover, as the viscosity ratio between the two fluids is increased, transitions from radial branched patterns to increasingly stable interfaces exhibiting features of proportionate growth are observed. Striking interfacial dynamics such as finger coalescence phenomena are also observed, in which two fingers at the periphery of the interface eventually merge. We model the pattern morphologies at the initial stages of pattern formation by employing a linear stability analysis of the interface between a Newtonian and a shear-thinning fluid [11], considering viscosity ratio as the only control parameter. The computational work was conducted in collaboration with the Metallurgical and Material Engineering department, Indian Institute of Technology Madras, Chennai, India [12].

## 3.2 Sample preparation and experimental methods

The interfacial patterns are studied in a radial Hele-Shaw cell (section 2.3.2 in chapter 2). Aqueous cornstarch suspensions are used as the non-Newtonian outer fluid, which are displaced by glycerol-water mixtures, the Newtonian inner fluid. All experiments are performed at room temperature (25°C). Fig. 3.1(a) shows a schematic of the top view of the radial Hele-Shaw cell. A cornstarch suspension of fixed concentration (black area in Fig. 3.1(a)), the outer fluid, is first introduced with a syringe

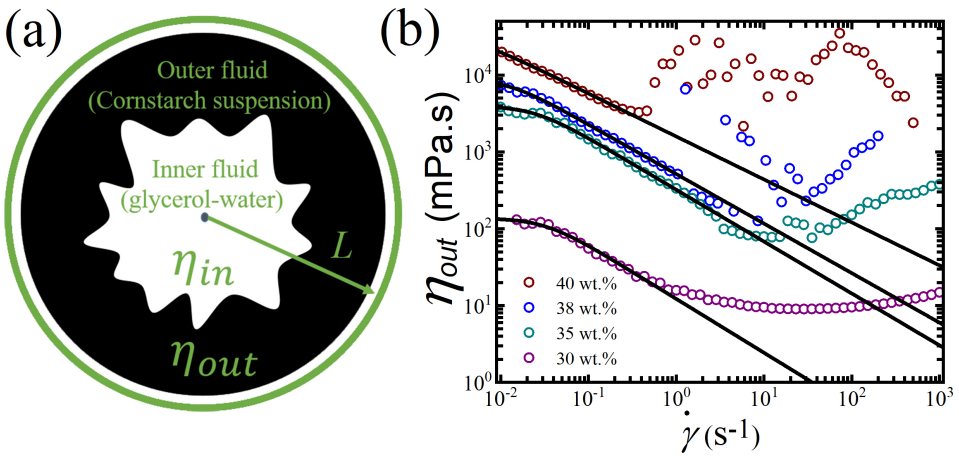



**Fig. 3.1:** **(a)** Schematic illustration of a radial Hele-Shaw cell (top view). **(b)** Viscosity ($\eta_{out}$) *vs.* shear rate ($\dot{\gamma}$) for different concentrations of cornstarch suspensions. The black solid line is the fit of the data in the shear-thinning regime to the simplified Carreau model [13], $\eta_{out} = \eta^o_{out}[(1 + (\tau\dot{\gamma})^2)]^{(n-1)/2}$. Here, $\eta^o_{out}$ is the zero-shear viscosity of the cornstarch suspension, $\tau$ denotes its characteristic relaxation time and $n$ is an exponent. The extrapolated value of viscosity at a shear rate approaching zero is denoted by $\eta^o_{out}$. All experiments are performed at room temperature (25°C).

pump at a constant volumetric flow rate of 2 ml/min through a 3 mm hole drilled in the top plate. Sample preparation protocols of cornstarch suspensions are provided in section 2.2.1 of chapter 2. A glycerol-water mixture (white area in Fig. 3.1(a)), the inner fluid, is next pumped into the cell through the same hole at a flow rate of 1 ml/min. Details of the Hele-Shaw cell are given in chapter 2 (section 2.3.2). The interfacial pattern evolution is recorded as an RGB image using a D5200 DSLR camera (set up below the cell) having a spatial resolution of 6000 × 4000 pixels with a time interval of 1 s between successive images. The RGB image is first converted into a grayscale image and then to a binary form using the imbinarize function in the MATLAB@2018 toolbox. In the binarization process, the threshold of the grayscale image is set by a global method based on Otsu's algorithm [14]. Otsu's method, which is based on computing image variances, is a very successful global thresholding method, particularly for images involving good contrast.

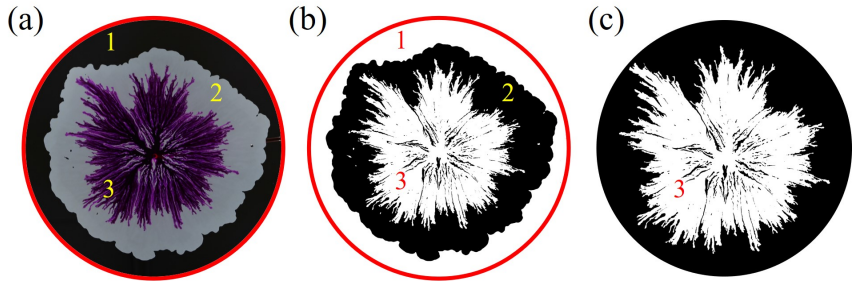



**Fig. 3.2:** **(a)** RGB image for $\eta_{in}/\eta_{out} = 9.4 \times 10^{-4}$ at $t = 100$ s. The region 1 represents the glass plate of the Hele-Shaw cell, region 2 represents the outer viscoelastic cornstarch suspension and region 3 represents the inner dyed glycerol-water mixture. In order to estimate sweep efficiency, the areas of regions 2 and 3 are estimated from the RGB image in (a) using the MATLAB@2018 image toolbox. **(b)** Binary form of RGB image in (a). **(c)** Binary form of the interfacial pattern formed by the displacing fluid (region 3) is highlighted.

### 3.2.1 Image processing and calculation of sweep efficiencies

Figure 3.2(a) shows the RGB image for $\eta_{in}/\eta_{out} = 9.4 \times 10^{-4}$ with region 1 representing the glass plate of the Hele-Shaw cell, region 2 representing the outer cornstarch suspension and region 3 representing the pattern formed by the dyed glycerol-water mixture. The RGB image is first converted into grayscale image and then into binary form using the imbinarize function using MATLAB@2018 (Fig. 3.2(b-c)). All the different regions 1, 2 and 3 in the binary image (Fig. 3.2(b)) are labeled in order to process them separately. The areas of regions 2 and 3 are estimated by analyzing the RGB image using the MATLAB@2018 image toolbox. Sweep efficiency [15] is estimated by taking the ratio of the area contacted by the inner fluid (region 2 in Fig. 3.2(b)) and the total area occupied by both inner and outer fluids (sum of the areas of regions 2 and 3 in the same figure).

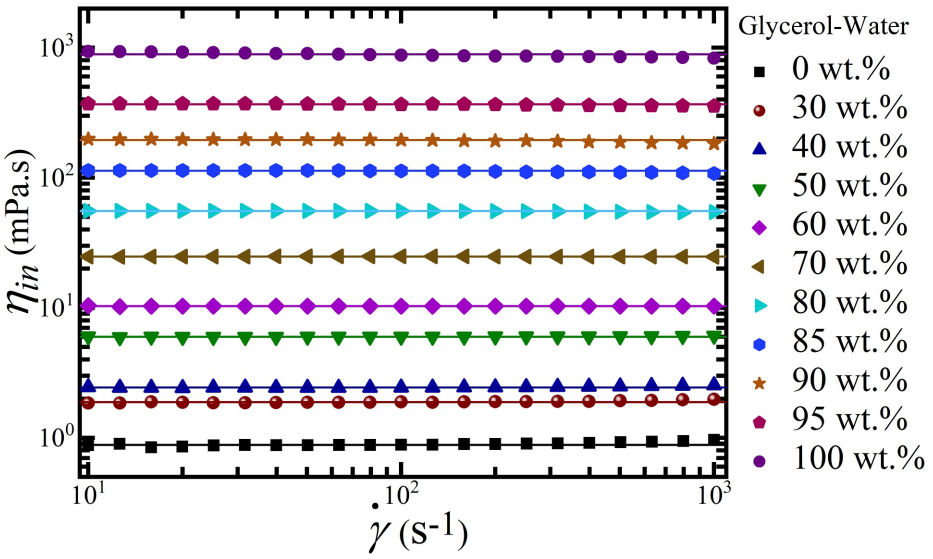



**Fig. 3.3:** Viscosities of glycerol-water mixtures (inner fluid) ($\eta_{in}$) *vs.* shear rate ($\dot{\gamma}$), where the weight percent (wt.%) of glycerol ranges from 0 (■) to 100 (●). The viscosity changes negligibly over the range of shear rates explored, thereby highlighting the Newtonian flow behavior of the mixture. The viscosity value at shear rate $\dot{\gamma} \to 0$ is taken as $\eta_{in}$.

## 3.3 Results and Discussion

### 3.3.1 Rheological characterization of dense cornstarch suspensions

Steady state flow experiments of cornstarch suspensions are performed using a parallel plate geometry with a plate diameter of 50 mm and a gap of 300 $\mu$m in a stress controlled Anton Paar MCR 702 rheometer. Flow curves for different concentrations of cornstarch suspensions (outer fluid) are shown in Fig. 3.1(b). We note that cornstarch suspensions have shear dependent viscosities (Fig. 3.1(b)), therefore, shear rates ($\dot{\gamma}$) imposed by the inner fluid while displacing the outer fluid are estimated as $2U/b$ [16] where, $U$ is the characteristic radial propagation velocity of the displacing fluid and $b$ is the gap of the Hele-Shaw cell. In order to estimate $U$, the instantaneous values of finger tip velocity, $U = dR_o/dt$, are calculated by taking

the time derivative of the length scale $R_o$ of the fingers. The estimated values of $U$ vary in the range of $2.0 \times 10^{-3} - 3.0 \times 10^{-1}$ cm/s for the different viscosity ratios, $\eta_{in}/\eta_{out}$, for a cornstarch suspension concentration of 35 wt.%. In our work, $\eta_{in}$ is the viscosity of the inner (glycerol-water mixture) fluid and $\eta_{out}$ is the viscosity of the outer (cornstarch suspensions) fluid. These values of $U$ correspond to shear rates of $2.0 \times 10^{-1}$ s$^{-1}$ $\leq \dot{\gamma} \leq 35.0$ s$^{-1}$. The shear rate $2.0 \times 10^{-1}$ s$^{-1}$ is used as a representative value for calculations in the remainder of this chapter. The viscosity $\eta_{out}$ of the cornstarch suspensions at this shear rate and viscosity $\eta_{in}$ of the Newtonian inner fluid are used to compute the viscosity ratio $\eta_{in}/\eta_{out}$ for each glycerol-water mixture. A double gap geometry with an effective length of 40 mm and a gap of 1.886 mm is used in a stress controlled Anton Paar MCR 501 rheometer for measuring the viscosities $\eta_{in}$ of glycerol-water mixtures with varying proportions of glycerol and water (Fig. 3.3).

For a given cornstarch suspension concentration, the viscosity ratio $\eta_{in}/\eta_{out}$ is

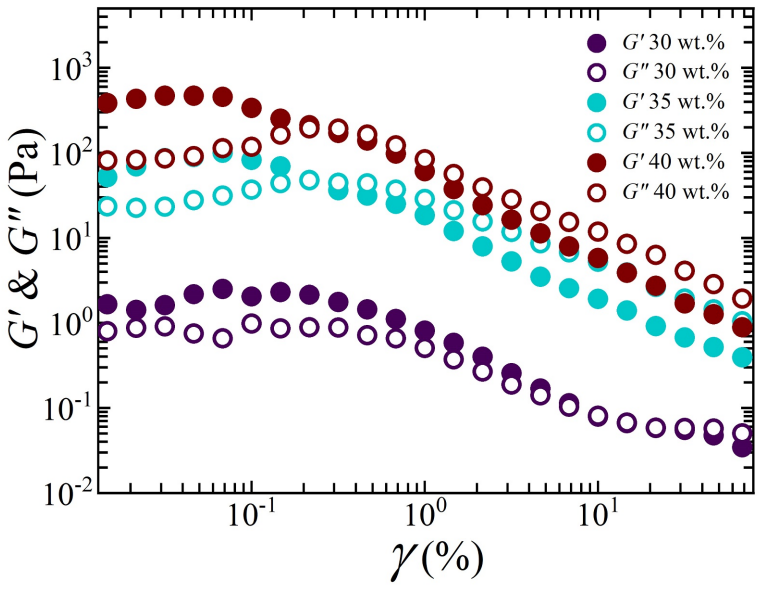



**Fig. 3.4:** Elastic moduli $G'$ (solid symbols) and viscous moduli $G''$ (open symbols) of cornstarch suspensions of different concentrations as a function of strain amplitude $\gamma$. Here, the weight percent (wt.%) of cornstarch suspensions ranges from 30 ($G'$(●),$G''$ (○)) to 40 ($G'$(●),$G''$ (○)). All experiments are performed at room temperature (25°C).

controlled by tuning the glycerol concentration in the glycerol-water mixture. It is seen that the shear rate $2.0 \times 10^{-1}$ s$^{-1}$ lies in the shear-thinning regime for cornstarch suspensions in the concentration range of 30 – 40 wt.% used in this study. Oscillatory rheological tests at low strains show an increase in elastic modulus with an increase in concentration of the cornstarch suspensions (Fig. 3.4). The concentration-dependent elasticity of the cornstarch suspensions is characterized in terms of Weissenberg number ($Wi$), which measures the ratio of elastic and viscous forces in simple shear flows [17] and is defined as $Wi = \dot{\gamma}\tau$, where $\dot{\gamma}$ is set to $2.0 \times 10^{-1}$ s$^{-1}$ and $\tau$ is the characteristic relaxation time of the cornstarch suspension. The values of $\tau$ for different concentrations of cornstarch suspensions are estimated from fits of the viscosity *vs.* shear rate data (Fig. 3.1(b) and Table 3.1) to the simplified Carreau model:

$$\eta_{out} = \eta^{o}_{out}[(1 + (\tau\dot{\gamma})^2)]^{(n-1)/2} \tag{3.1}$$

Here, $\eta^{o}_{out}$ is the zero-shear viscosity of the cornstarch suspension, $\tau$ denotes its characteristic relaxation time and $n$ is an exponent. The black solid line in Fig. 3.1(b) is the fit of the data to the simplified Carreau model (equation 3.1). For the 35 wt.% suspension, the fitting parameters are $\eta^{o}_{out} = 3.952$ Pa.s, $n = 0.32$, and $\tau = 41$ s (Table 3.1). Here, $\eta^{o}_{out}$ is the extrapolated value of viscosity at a shear rate approaching zero. Shear-thinning of cornstarch suspensions can be attributed to particle rearrangements, a constant hydrodynamic viscosity contribution arising from viscous stresses and an entropic contribution originating from random particle collisions [18, 19]. Beyond a high critical shear rate, inter-particle frictional forces lead to the formation of a fragile soft solid that exhibits shear-thickening [20–22]. In this chapter, the displacement of shear-thinning cornstarch suspensions by glycerol-water mixtures in the radial Hele-Shaw geometry is recorded at different viscosity ratios of the two fluids and while controlling $Wi$ of the viscoelastic outer fluid.

**Table 3.1:** Values of $\eta^o_{out}$, $\tau$ and $n$, obtained from fits of the flow curve data in Fig. 3.1(b)) to the simplified Carreau model (equation 3.1). Weissenberg numbers (for a representative $\dot{\gamma} = 2.0 \times 10^{-1}$ s$^{-1}$), obtained for cornstarch suspensions of different concentrations, are also shown.

| Conc. (wt.%) | $\eta^o_{out}$ (mPa.s) | $\tau$ (s) | $n$ | $Wi$ |
|---|---|---|---|---|
| 30 | 137 | 31 | 0.29 | 6.2 |
| 35 | 3952 | 41 | 0.32 | 8.2 |
| 38 | 8951 | 84 | 0.35 | 16.8 |
| 40 | 31471 | 206 | 0.44 | 41.2 |

### 3.3.2 Interfacial pattern morphologies and their dependence on viscosity ratio

Figure 3.5 shows the temporal evolution of the interfacial patterns obtained during the displacement of 35 wt.% cornstarch suspension by water for various viscosity ratios. The binary forms of the fully-developed pattern morphologies in Figs. 3.5(a3, b3, c3, d3, e3 & f3) are shown in Figs. 3.6(a-f). At low $\eta_{in}/\eta_{out}$, radial branched patterns (Fig. 3.6(a)) are observed. The shear-thinning nature of the outer fluid enhances the velocity of the tips of the fingers while suppressing the motion of the fingers away from the tips. The large driving pressures, in contrast, attempt to broaden the fingertips. The competition of these two processes leads to the formation of ramified patterns [23] at low viscosity ratios. As $\eta_{in}/\eta_{out}$ is increased, pattern morphologies change substantially, even displaying features of proportionate growth. At intermediate and high viscosity ratios, a dark inner circular region, devoid of fingers and comprising only the inner fluid, appears and grows larger (Figs. 3.6(b-f)). This inner circular region covers almost the entire pattern (Fig. 3.6(f)) at the highest $\eta_{in}/\eta_{out}$, with small protrusions forming at the periphery of the pattern. Our observations are in agreement with previous numerical and experimental studies which have reported that elasticity sets a shorter instability wavelength and enhances finger formation at the interface between a Newtonian and a non-Newtonian fluid [24, 25].

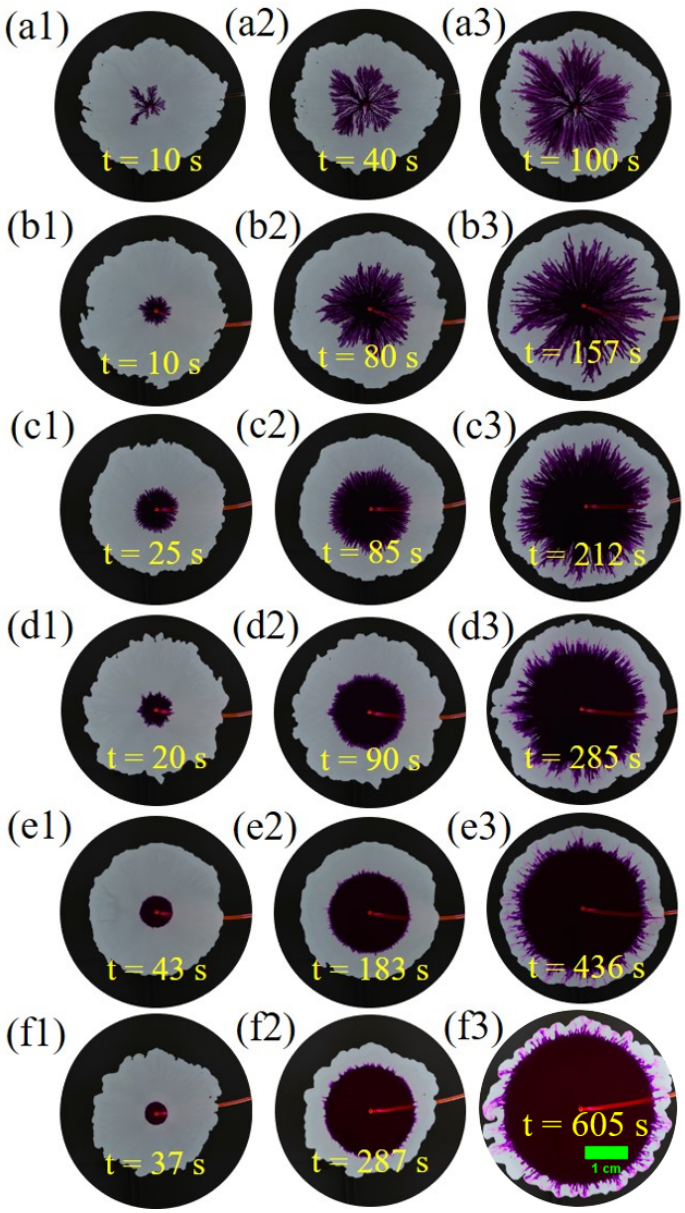



**Fig. 3.5:** The raw RGB images showing temporal evolution of interfacial patterns for viscosity ratios: **(a1-a3)** $\eta_{in}/\eta_{out} = 9.4 \times 10^{-4}$, **(b1-b3)** $2.0 \times 10^{-3}$, **(c1-c3)** $6.4 \times 10^{-3}$, **(d1-d3)** $5.9 \times 10^{-2}$, **(e1-e3)** $3.9 \times 10^{-1}$ and **(f1-f3)** $9.5 \times 10^{-1}$ when a dyed glycerol-water mixture invades a cornstarch suspension (35 wt.%, $Wi = 8.2$ at $\dot{\gamma} = 2.0 \times 10^{-1}$ s$^{-1}$) in a radial Hele-Shaw cell. The outside black region represents the glass plate of the Hele-Shaw cell, the white region represents the outer viscoelastic cornstarch suspension and the magenta region represents the dyed glycerol-water mixture. The scale bar is 1 cm.

We follow the protocol adopted by Bischofberger *et al.* [9] and quantify the interfacial patterns in terms of the following distinct length scales (bottom inset

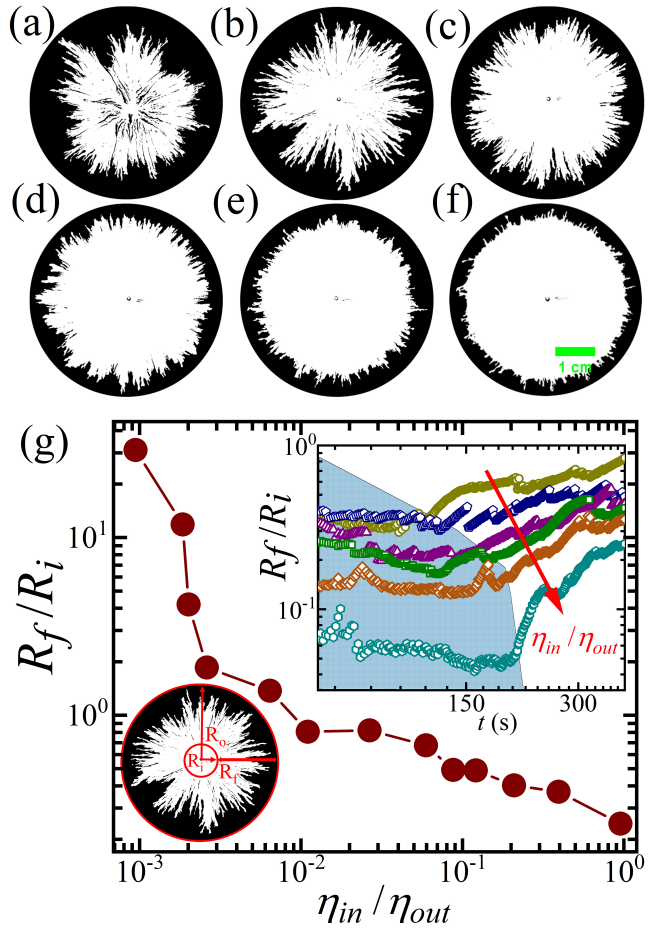



**Fig. 3.6: (a-f)** Patterns for increasing viscosity ratios: $\eta_{in}/\eta_{out} = 9.4 \times 10^{-4}$, $2.0 \times 10^{-3}$, $6.4 \times 10^{-3}$, $5.9 \times 10^{-2}$, $3.9 \times 10^{-1}$, $9.5 \times 10^{-1}$ at 100 s, 157 s, 212 s, 285 s, 436 s and 605 s after a glycerol-water mixture invades a cornstarch suspension ($Wi = 8.2$) in a radial Hele-Shaw cell. **(g)** Inset (bottom) shows the three characteristic length scales, $R_o$, $R_i$ and $R_f$. The size ratio $R_f/R_i$ *vs.* $\eta_{in}/\eta_{out}$ for $R_o = 13.5$ cm. Inset (top) shows $R_f/R_i$ *vs.* time ($t$) to illustrate the seemingly proportionate growth of the patterns at earlier times for $5.9 \times 10^{-2} \leq \eta_{in}/\eta_{out} \leq 9.5 \times 10^{-1}$.

of Fig. 3.6(g)): $R_o$, the radius of the smallest circle enclosing the entire pattern, $R_i$, the radius of the largest circle enclosing the solid region comprising the inner Newtonian fluid and $R_f$, the finger length defined as $R_f = R_o - R_i$. Figure 3.6(g) shows a systematic decrease in pattern size ratios, $R_f/R_i$, with increasing $\eta_{in}/\eta_{out}$ for fixed $R_o = 13.5$ cm and resembles the observation for a pair of Newtonian fluids [9]. For $5.9 \times 10^{-2} \leq \eta_{in}/\eta_{out} \leq 9.5 \times 10^{-1}$, the interfacial patterns (Fig. 3.7) exhibit features of proportionate growth [26, 27], with $R_f$ and $R_i$ growing almost

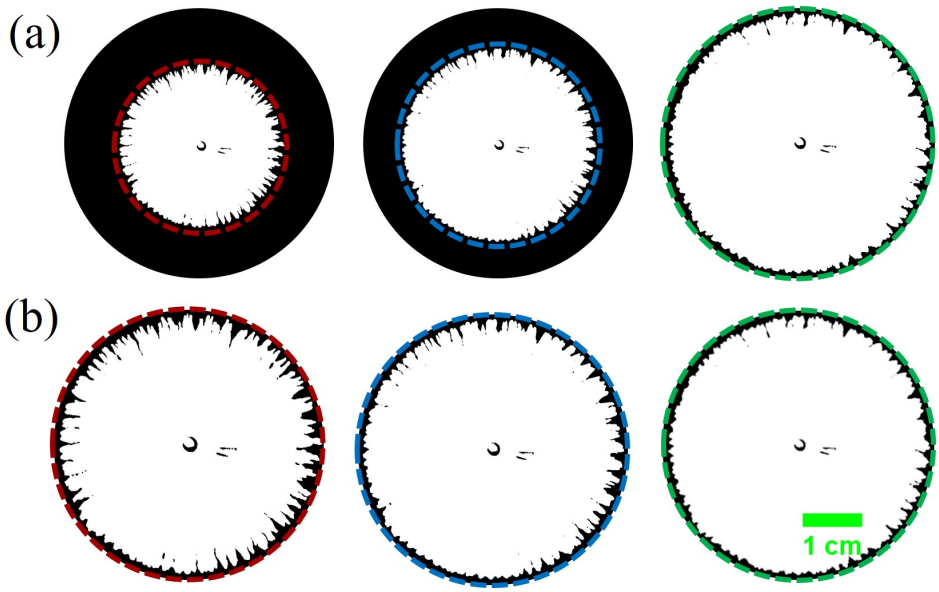



**Fig. 3.7: (a)** Temporal evolution of interfacial patterns for $\eta_{in}/\eta_{out} = 1.2\times10^{-1}$ (from left to right) at 61 s, 81 s and 101 s. The scale bar is 1 cm. The colored dashed circles enclose the inner fluid as the interfacial patterns develop with time. **(b)** Zoomed images of the patterns displayed in (a) in which only the region within the colored circles are displayed. The images are nearly indistinguishable, indicating that fingers at the periphery of the pattern grow proportionally with the overall pattern.

proportionally with time. This leads to near-flattening of $R_f/R_i$ at early times of pattern growth (Fig. 3.6(g), shaded region in top inset).

The sweep efficiency, defined as the ratio of the area contacted by the inner fluid (black area in Fig. 3.1(a)) and the total area occupied by both inner and outer fluids (sum of the black and white areas in the same figure) [15], measures the displacement of the outer fluid by the inner fluid. Details about the calculation of sweep efficiency is provided in section 3.2.1. Figure 3.8 shows the variation of sweep efficiency with time for various $\eta_{in}/\eta_{out}$. The viscosity ratio strongly affects the morphologies of the interfacial patterns which in turn changes the sweep efficiencies at any given time. The sweep efficiency increases with increasing $\eta_{in}/\eta_{out}$, indicating suppression of instabilities. At early times, the fingers do not grow appreciably until a certain short response time required to overcome the inertial effects of the flow. Once inertial effects are overcome, the patterns grow steadily, leading to a rapid decrease in the sweep efficiency at later times. We note that a small region of upwardly

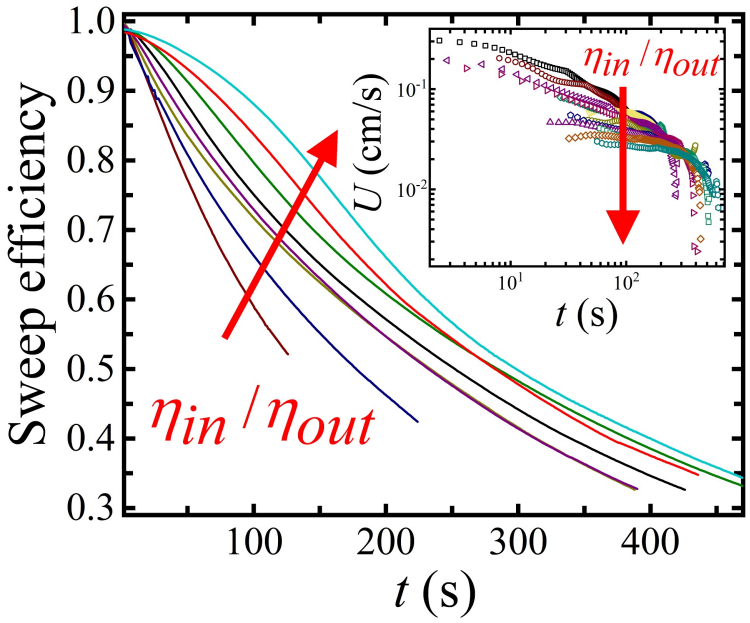



**Fig. 3.8:** Sweep efficiency *vs.* time ($t$) for different viscosity ratios ($9.4\times10^{-4} \leq \eta_{in}/\eta_{out} \leq 9.5 \times 10^{-1}$). Inset shows the estimated values of instantaneous finger tip velocity ($U$) *vs.* time ($t$) for the same viscosity ratio regime.

convex variation at initial times is present for experiments performed at the higher viscosity ratio values. At the highest viscosity ratio of $\eta_{in}/\eta_{out} = 9.5 \times 10^{-1}$, the disparity between the two fluid viscosities is the least, and the driving force for fingering instability has weakened. Hence, it takes longer for the fingers to grow, when the viscosity ratios are high, as shown in Fig. 3.8. Suppression of instability for increasing viscosity ratios is further confirmed by a decrease in the estimated finger tip velocity $U$ (inset of Fig. 3.8).

### 3.3.3 Coalescence events at the interface

Figure 3.9(a) shows the evolution of interfacial patterns for $\eta_{in}/\eta_{out} = 5.9 \times 10^{-2}$. Magnified images of interfacial areas marked within colored circles in Fig. 3.9(a) are shown in Fig. 3.9(b). The red box in Fig. 3.9(b) encloses two fingers (designated in white in the binary image) which eventually merge at a later time (blue box in Fig. 3.9(b)). In certain interfacial regions, a pool of cornstarch suspension forms

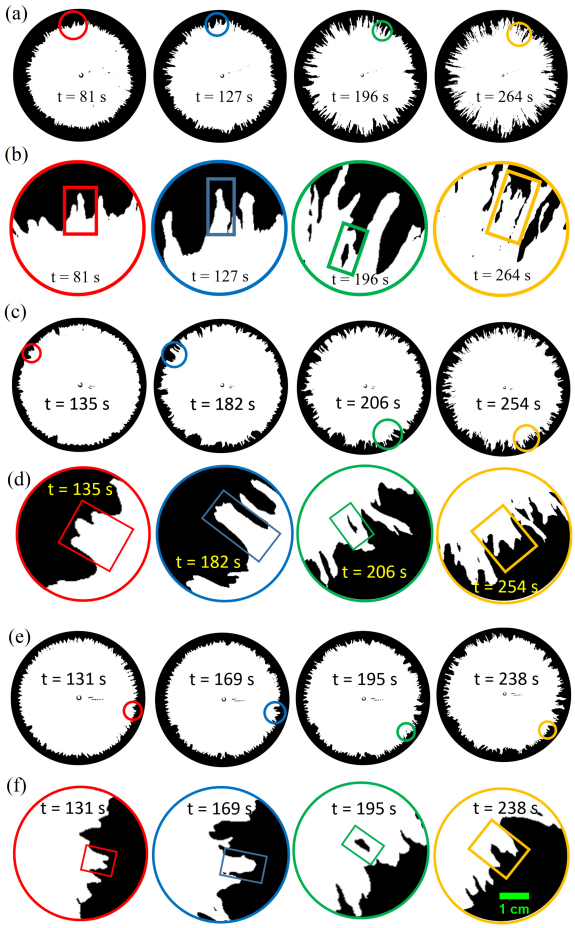



**Fig. 3.9:** **(a)** The evolution of the patterns for viscosity ratio, $\eta_{in}/\eta_{out} = 5.9 \times 10^{-2}$, with time increasing from left to right. Colored boxes are drawn to display the coalescence events. **(b)** Zoomed images of the interfacial patterns areas within the colored circles drawn in (a). Colored solid circles are drawn to highlight the areas where coalescence events are observed. In all the images above, the solid red circle encloses a portion of the interface just before the coalescence event. The portions enclosed by the solid blue circle shows the merging of the fingers. The green box shows the formation of a pool of cornstarch in the inner fluid that diffuses out and is eventually followed by the growth of new fingers, displayed within the yellow box. **(c)** Patterns for viscosity ratio $\eta_{in}/\eta_{out} = 1.2 \times 10^{-1}$ with time increasing from left to right. **(d)** Zoomed images of the areas within the colored circles drawn in (c). Colored boxes are drawn to display the events with enhanced clarity. **(e)** Patterns for $\eta_{in}/\eta_{out} = 2.0 \times 10^{-1}$. **(f)** Zoomed images of the areas within the colored circles drawn in the patterns shown in (e).

within the inner fluid (green box in Fig. 3.9(b)) and diffuses out gradually. This is followed by the growth of new fingers at the interface (designated in black and enclosed by the yellow box in Fig. 3.9(b)). Coalescence events, typically observed in the intermediate to high viscosity ratio regimes, are also shown for two viscosity

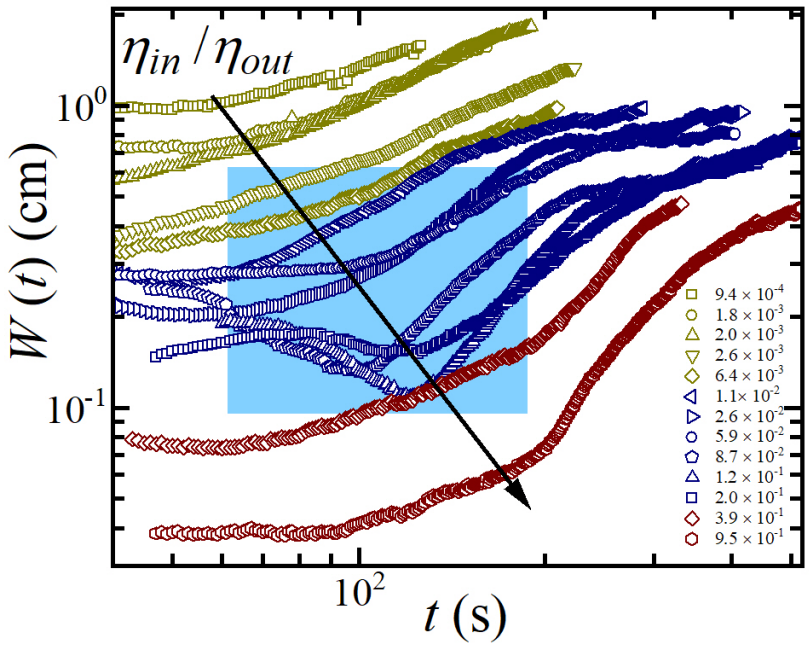



**Fig. 3.10:** Growth of overall width $W(t)$ of the interface for three different viscosity ratio regimes: $9.4 \times 10^{-4} - 6.4 \times 10^{-3}$, $1.1 \times 10^{-2} - 2.0 \times 10^{-1}$ and $3.9 \times 10^{-1} - 9.5 \times 10^{-1}$. The blue shaded region highlights the time domain in which the overall width decreases.

ratios, $\eta_{in}/\eta_{out} = 1.2 \times 10^{-1}$ (Figs. 3.9(c-d)) and $\eta_{in}/\eta_{out} = 2.0 \times 10^{-1}$ (Figs. 3.9(e-f)). The observed coalescence events can be attributed to differences in velocity profiles of two neighboring fingers [28]. This mismatch controls the interactions between the two neighboring fingers and results in one finger merging into another.

Jackson *et al.* [29] have provided insights into mechanisms of finger interaction phenomena in Hele-Shaw cells such as shielding, coalescence, and finger break-off through detailed numerical simulations. At very low $\eta_{in}/\eta_{out}$, the interface velocity is much smaller near the base of the fingers than at the tip, and the bases effectively become stagnation points. This leads to lower sweep efficiency (as confirmed by Fig. 3.8), and larger fingers shield the growth of smaller ones. However, at higher $\eta_{in}/\eta_{out}$, the velocity of the base of the fingers is large enough for the outer fluid to be displaced significantly. These regions will have a significantly high velocity component in the radial direction compared to the case of lower $\eta_{in}/\eta_{out}$. Therefore, the ensuing mass transport helps in overcoming the miscible region between fingers,

causing coalescence. The fluctuation in the radial extent of the interface is computed in terms of its overall width $W(t) = \sqrt{< (r(\theta,t) - < r(\theta,t) >_\theta)^2 >_\theta}$, where $r(\theta,t)$ is the local radius of the interface at an angle $\theta$, measured from an arbitrary axis and varying from 0 to $2\pi$, and $< ... >_\theta$ denotes the average over $\theta$ [30]. Figure 3.10 shows the variation in the overall width $W(t)$ of the pattern with time $t$. The observed reduction in $W(t)$ for $1.1 \times 10^{-2} \leq \eta_{in}/\eta_{out} \leq 2.0 \times 10^{-1}$ (within blue shaded region in Fig. 3.10) can likely be attributed to coalescence events. Such finger interaction events have been observed earlier at fluid interfaces during miscible linear displacements [31, 32] as well as predicted by numerical simulations [15].

### 3.3.4 Role of elasticity of the cornstarch suspension on interfacial roughness and sweep efficiency

The impact of elasticity of the outer cornstarch suspensions on interfacial patterns at a fixed $\eta_{in}/\eta_{out}$ is next explored (Figs. 3.11(a-d)). The viscosity ratio is fixed by tuning the concentrations of both glycerol-water mixtures and cornstarch suspensions. Increasing the concentration-dependent elasticity of the outer cornstarch suspension,

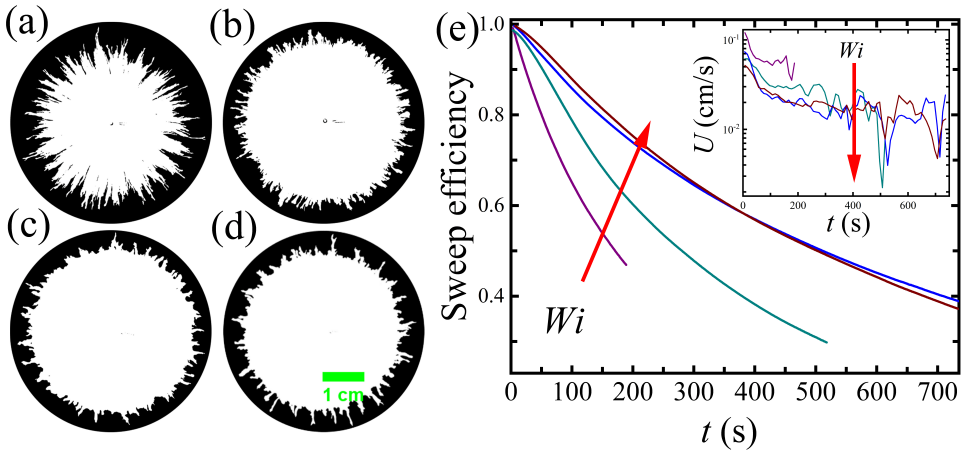



**Fig. 3.11:** Patterns at $\eta_{in}/\eta_{out} = 2.0 \times 10^{-1}$ for different Weissenberg numbers: **(a)** $Wi$ = 6.2, **(b)** $Wi$ = 8.2, **(c)** $Wi$ = 16.8 and **(d)** $Wi$ = 41.2 at 190 s, 391 s, 648 s and 614 s for an identical $R_o$ = 13.5 cm. **(e)** Sweep efficiency *vs.* time ($t$) plot for $Wi$ = 6.2 (—), $Wi$ = 8.2 (—), $Wi$ = 16.8 (—) and $Wi$ = 41.2 (—). Inset shows instantaneous values of finger tip velocity $U$ *vs.* $t$ for different $Wi$.

and hence the value of its Weissenberg number ($Wi$, Fig. 3.4 & Table 3.1), leads to a reduction in lengths of the fingers. As predicted in nonlinear simulations [15], we see that lengths of fingers depend on $Wi$ of the displaced viscoelastic cornstarch suspension. A simultaneous breakup of the interface into multiple small protrusions is also noted. Sweep efficiency, as defined in section 3.2, is computed, and is seen to increase with increasing $Wi$, before eventually saturating at the highest $Wi$ values explored here (Fig. 3.11(e)). This is attributed to the higher normal stresses at larger $Wi$, which can limit finger growth [15] and enhance sweep efficiency. Owing to the elasticity of the outer fluid, the non-zero normal stresses cause a stress difference between the propagating direction and the direction perpendicular to it, which in turn retards the growth of propagating fingers by dragging it in the reverse flow direction. Increased flow stabilization with increasing $Wi$, also predicted in nonlinear simulations [15], is further verified by a decrease in instantaneous values of finger tip velocity ($U$) with increase in $Wi$ (inset of Fig. 3.11(e)). The non-Newtonian outer viscoelastic material leads to fluctuations in the local stress profiles and affects interfacial instabilities [33]. The stable regime at high $Wi$ can also arise from the stabilizing effect of the non-vanishing normal stress differences [15] of the outer cornstarch suspension. The morphological evolution at the interface between a Newtonian and a non-Newtonian fluid is therefore extremely sensitive to the elasticity of the outer fluid even at constant $\eta_{in}/\eta_{out}$.

### 3.3.5 Spacing between fingers: Theoretical estimate vs. experimental measurements

We compare the experimentally observed formation of interfacial patterns at the onset of instability with the predictions of a mathematical model. The computational part is performed by collaborators at IIT Madras, India [12] and is included here to ensure that the discussion is compete. It has been noted that the estimated values of shear rates lie in the shear-thinning regime of the flow curves of the cornstarch suspensions. Therefore, we follow the protocols adopted in a previous study [11] for

numerical prediction of the dominant wavelength of interfacial perturbation at the onset of instability between a Newtonian inner fluid and a shear-thinning outer fluid. The dominant interfacial instability wavelength is computed through linear stability analysis of the interface between a Newtonian and a shear-thinning fluid. We employ the model in [11] that caters to the rectilinear displacement of the interface between miscible fluids in a Hele-Shaw cell. Our experimentally measured spacing between fingers at the onset of instability is found to be smaller than the radius of the circular interface at those instances for most viscosity ratios, permitting the use of a flat interface approximation. The goal is to understand the dependence of instability wavelength on liquid rheological properties like zero shear viscosity $\eta^o_{out}$, Deborah number ($De = \tau U/b$), and the Carreau model exponent $n$ to explain the initial distribution of fingers seen experimentally. First, the equations governing the flow, Darcy's law [34], continuity equation and convection-diffusion equation [35] for the concentration of the displacing fluid (glycerol-water mixtures in our experiments) are written. The inner fluid velocity, $u$, in the displacement direction, the concentration-dependent dynamic viscosity, $\eta_{out}$, of the cornstarch suspension, and the concentration $c$ are respectively subjected to small perturbations from their base state values ($u_o$,$\eta^o_{out}$,$c_o$). The perturbations, $u^{'}$, $\eta'_{out}$ and $c^{'}$ can be described by the dimensional equations [11]:

$$\left(\frac{\partial^2 u'}{\partial x^2} + \frac{\partial^2 u'}{\partial y^2}\right) + \frac{1}{\eta^o_{out}}\frac{\partial \eta^o_{out}}{\partial x}\frac{\partial u'}{\partial x} + \frac{1}{\eta^o_{out}}\frac{\partial^2 \eta'_{out}}{\partial y^2} = 0 \tag{3.2}$$

$$\frac{\partial c'}{\partial t} + u'\frac{\partial c_o}{\partial x} = \frac{\partial^2 c'}{\partial x^2} + \frac{\partial^2 c'}{\partial y^2} \tag{3.3}$$

where $x$ denotes the direction of flow, and $y$ is parallel to the interface. The scaling factors for non-dimensionalisation are $D/U$ for lengths, $D/U^2$ for time, the viscosity of the displacing fluid, $\eta_{in}$, for the viscosities of both fluids, and $D\eta_{in}/\kappa$ for pressure. Here, $D$ is the diffusion coefficient of the system, $U$ is the characteristic velocity of the displacing fluid and $\kappa$ is the permeability of the medium which is assumed

constant.

We seek solutions to equations (3.2) and (3.3) of the form:

$$(c', u')\,(x, y, t) = (C', U')\,(x) \exp(\sigma\,(t_0)\,t) \exp(iky) \tag{3.4}$$

where $(C', U')$ are the amplitudes in the perturbations $(c', u')$, $k$ represents the wavenumber and $\sigma$ is the growth rate for the perturbations. Neglecting all non-linear terms in the perturbations, the dispersion relation for a Newtonian fluid displacing a non-Newtonian fluid is obtained as:

$$k(k-l)(k\beta-l)\left[l^3 + (1+\beta)kl^2 + \left(\frac{2k^2\beta(\alpha\beta+\zeta)}{(\alpha+\zeta)(1+\beta)} - \frac{\tilde{R}k}{1+\beta}\right)l - \frac{\tilde{R}k^2(\alpha+\zeta\beta)}{(\alpha+\zeta)(1+\beta)}\right] = 0 \tag{3.5}$$

The equation is further simplified to obtain the cutt-off wavenumber $k_c$ by setting $\sigma = 0$ in equation 3.5 as:

$$k_c = \tilde{R}\frac{2\alpha + \zeta(1+\beta)}{(2+\beta)(1+\beta)(\alpha+\zeta) + 2\beta(\alpha\beta+\zeta)} \tag{3.6}$$

Here, $l$ is given by $l^2 = k^2 + \sigma$ while $\tilde{R}$, $\alpha$, $\beta$ and $\zeta$ are defined as follows:

$$\tilde{R} = ln(\alpha) + \frac{(n-1)}{2} ln(1 + De^2), \tag{3.7}$$

$$\alpha = \frac{\eta^o_{out}}{\eta_{in}}, \tag{3.8}$$

$$\beta = \sqrt{1 + (n-1)(\frac{De^2}{1+De^2})}, \tag{3.9}$$

$$\zeta = \left(1 + De^2\right)^{(1-n)/2}. \tag{3.10}$$

Here, $De$ is the Deborah number, $n$ is the exponent and $\eta^o_{out}$ refers to the zero shear

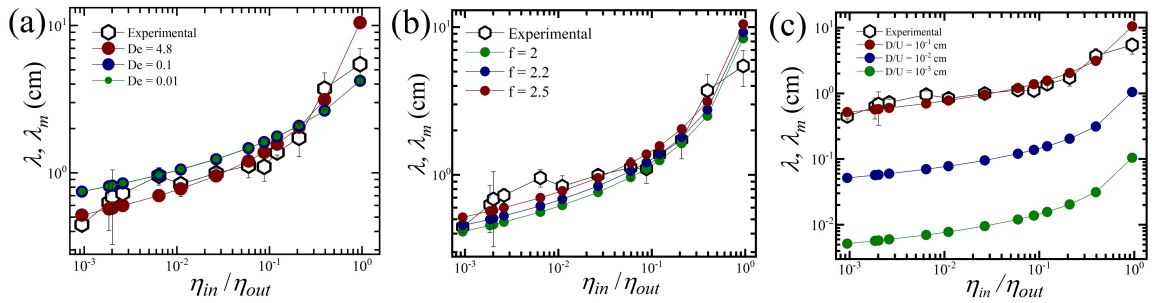



**Fig. 3.12:** Most dominant wavelength ($\lambda_m$) *vs.* viscosity ratio ($\eta_{in}/\eta_{out}$) illustrating the effect of variation of parameters: **(a)** $De = 4.8$, 0.1, 0.01 for $f = 2.5$ and $D/U = 1.0\times10^{-1}$ cm **(b)** $f = 2.0$, 2.2, and 2.5 for $D/U = 1.0\times10^{-1}$ cm and $De = 4.8$. **(c)** $D/U = 1.0\times10^{-1}$ cm, $1.0 \times 10^{-2}$ cm, $1.0 \times 10^{-3}$ cm for $De = 4.8$ and $f = 2.5$. The plots show a good agreement between experimental, $\lambda$, and computational, $\lambda_m$, values of most dominant wavelength for $f = 2.5$, $De = 4.8$ and $D/U = 1.0 \times 10^{-1}$ cm.

viscosity of cornstarch, as defined in equation 3.1.

$De$ and $D/U$ are the two input parameters used to compute the most dominant wavelength of the interfacial perturbation $\lambda_m = 2\pi/k_m$. $De$ is calculated from the definition $De = \tau U/b$, where $b$ is the gap of the Hele-Shaw cell [11]. Setting $U = 2.0 \times 10^{-3}$ cm/s (section 3.3.1), $\tau = 41$ s (Fig. 3.1(b)), and $b = 170$ $\mu$m, the value of $De$ is calculated to be 4.8, a typical value for a shear-thinning, viscoelastic fluid [36]. The uncertainty in the literature regarding $D$ values [37–41] and the difficulties in measuring $U$ preclude accurate estimation of $D/U$ for our experimental system. Nevertheless, if $D$ be considered an adjustable parameter, $D/U = 1.0 \times 10^{-1}$ cm provides a close match between the experimentally measured $\lambda$ and the numerically computed $\lambda_m$ in Fig. 3.12(c). The plots depicting the effects of variation of parameters $De$ ( Fig. 3.12(a)), $f$ (Fig. 3.12(b)) and $D/U$ (Fig. 3.12(c)) on the relationship between the most dominant wavelength and viscosity ratios, are illustrated. The computed value of the the dimensionless wavelength $\lambda_m$ has been dimensionalized by multiplying with $D/U$ and the dimensional values are used in the plots of Fig. 3.12. Accordingly, we compare the qualitative dependence of the experimentally measured instability wavelength on $\eta_{in}/\eta_{out}$ using the dimensionless expression for $k_c$ in equation 3.6, the critical wavenumber above which interfacial

perturbations are stable [11]. Using equation (3.6), the fastest-growing wavenumber, $k_m = k_c/f$, where $f$ is a multiplication factor that lies between 2 to 2.5 in thin-film flows of miscible liquids of similar densities (where the flow is governed by a balance between viscous stress and pressure gradient in the Hele-Shaw cell), is computed [11, 15, 42, 43].

To compare the most dominant wavelength of the interfacial perturbation, $\lambda_m = 2\pi/k_m$ (Fig. 3.13), with the corresponding wavelength $\lambda$ identified experimentally, the average finger spacing for different $\eta_{in}/\eta_{out}$ is estimated from experimental images at the early stages ($t < 100$ s) of pattern evolution. These patterns are selected as the mathematical model ignores nonlinear effects and the time-dependent viscosity changes of cornstarch suspensions that ensue during the later stages of pattern growth. Inset of Fig. 3.13 displays the experimental pattern observed at an initial

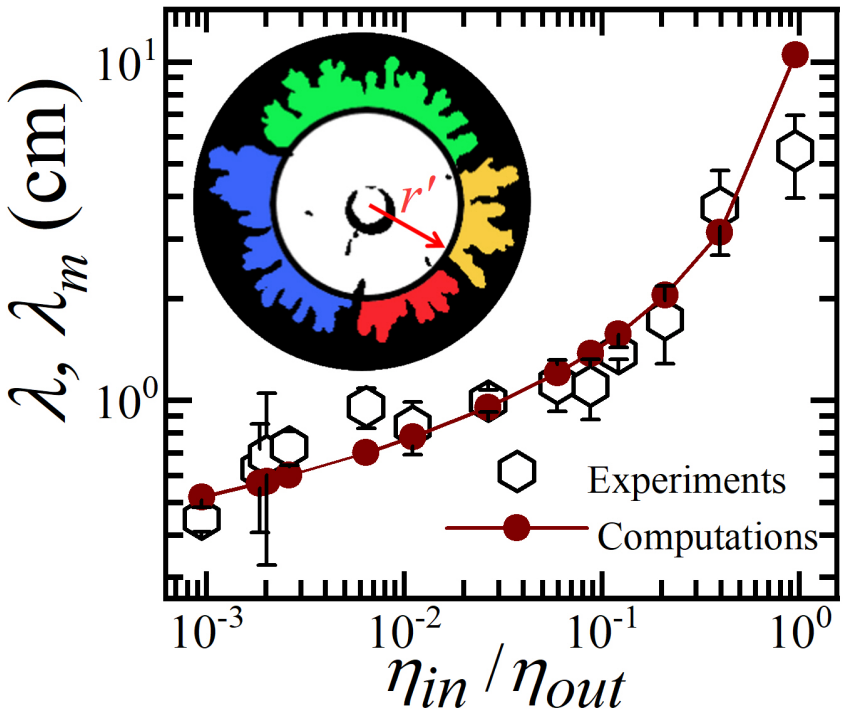



**Fig. 3.13:** Most dominant wavelengths for $\eta_{in}/\eta_{out} = 9.4 \times 10^{-4} - 9.5 \times 10^{-1}$ obtained from computational, $\lambda_m$, and experimental, $\lambda$, analyses for $Wi = 8.2$. Error bars represent standard deviation. Here $\lambda_m$ is computed for $De = 4.8$, $n = 0.32$, and $f = 2.5$. Inset shows an interfacial pattern at an early stage ($t = 5$ s) in a Hele-Shaw experiment for $\eta_{in}/\eta_{out} = 2.0 \times 10^{-3}$.

stage ($t = 5$ s) for $\eta_{in}/\eta_{out} = 2.0 \times 10^{-3}$, with the primary fingers designated by multiple colors. The average finger spacing, $\lambda$, is estimated as $\lambda = 2\pi r'/N$, where $N$ is the number of primary fingers (indicated by multiple colors) and $r'$ is the radius of the circle passing through the deepest trough of the pattern. A comparison of $\lambda_m$, obtained from numerical analysis, and $\lambda$, estimated from experimental data, for different $\eta_{in}/\eta_{out}$ shows good correlation for the 35 wt.% cornstarch suspension (Fig. 3.13). This suggests that the most dominant wavelength of the interfacial perturbation is a reliable estimate of the average spacing between experimentally obtained fingers. Since the shear-thinning behavior of cornstarch suspensions provides an additional source for the production of vorticity disturbance leading to a destabilizing effect on the flow, the interfacial instability is likely determined by a competition between this destabilizing source and momentum dissipation [11].

## 3.4 Conclusions

Motivated by the importance of rheological properties of fluids in large scale material processing, we have studied interfacial instabilities between dense viscoelastic cornstarch suspensions and glycerol-water mixtures (the miscible inner Newtonian fluid) over a wide range of viscosity ratios in a radial Hele-Shaw cell. We show in detail the emergence of various pattern regimes as a function of viscosity ratios, previously not reported extensively at Newtonian-non-Newtonian fluid interfaces. Despite the low interfacial tension, the patterns become less branched, have shorter fingers and display features of proportionate growth and finger coalescence with increasing viscosity ratios. While the general understanding from the existing literature is that pattern formation is primarily a function of viscosity ratios, here we have reported quantitatively the role of outer fluid elasticity on interfacial roughness and sweep efficiency in radial displacement of miscible fluids. Our results establish that the kinetics of pattern formation and displacement even at a fixed viscosity ratio is dependent on relaxation effects in a fluid by virtue of its viscoelasticity.

The viscosity ratio of the two fluids and the elasticity of the viscoelastic outer fluid modify the roughness of the interface and contribute to flow stabilization. The observed dependence of the dominant wavelength on viscosity ratio during the onset of the instability is computed by performing a linear stability analysis of the interface, wherein the shear-thinning viscoelastic fluid is described by a simplified Carreau model. Previous studies have suggested different strategies for controlling flow instabilities in pairs of Newtonian fluids [44, 45]. Our study augments the literature by identifying viscosity and elasticity regimes over which fingering patterns, finger coalescence and stable interfaces will exist for Newtonian-non-Newtonian fluid pairs. Our results have potential implications for processes involving displacement of shear-thinning slurries of viscoelastic materials such as mud and cement.

# References


[1] P. G. Saffman, G. I. Taylor, The penetration of a fluid into a porous medium or Hele-Shaw cell containing a more viscous liquid, Proc. Math. Phys. Eng. Sci. 245 (1242) (1958) 312–329. doi:10.1098/rspa.1958.0085.

[2] G. M. Homsy, Viscous fingering in porous media, Annual Review of Fluid Mechanics 19 (1) (1987) 271–311. doi:10.1146/annurev.fl.19.010187.001415.

[3] L. Paterson, Radial fingering in a Hele Shaw cell, J. Fluid Mech. 113 (1981) 513–529. doi:10.1017/S0022112081003613.

[4] T. T. Al-Housseiny, P. A. Tsai, H. A. Stone, Control of interfacial instabilities using flow geometry, Nature Physics 8 (10) (2012) 747–750. doi:10.1038/nphys2396.

[5] J.-D. Chen, Growth of radial viscous fingers in a Hele-Shaw cell, J. Fluid Mech. 201 (1989) 223–242. doi:10.1017/S0022112089000911.

[6] D. Bensimon, L. Kadanoff, S. Liang, B. Shraiman, C. Tang, Viscous flows in two dimensions, Reviews of Modern Physics 58 (4) (1986) 977–999. doi:10.1103/RevModPhys.58.977.

[7] S. A. Setu, I. Zacharoudiou, G. J. Davies, D. Bartolo, S. Moulinet, A. A. Louis, J. M. Yeomans, D. G. A. L. Aarts, Viscous fingering at ultralow interfacial tension, Soft Matter 9 (2013) 10599–10605. doi:10.1039/C3SM51571K.

[8] E. Lajeunesse, J. Martin, N. Rakotomalala, D. Salin, 3D instability of miscible displacements in a Hele-Shaw cell, Phys. Rev. Lett. 79 (1997) 5254–5257. doi:10.1103/PhysRevLett.79.5254.

[9] I. Bischofberger, R. Ramachandran, S. R. Nagel, An island of stability in a sea of fingers: emergent global features of the viscous-flow instability, Soft Matter 11 (2015) 7428–7432. doi:10.1039/C5SM00943J.

[10] V. Sharma, S. Nand, S. Pramanik, C.-Y. Chen, M. Mishra, Control of radial miscible viscous fingering, Journal of Fluid Mechanics 884 (2020). doi:10.1017/jfm.2019.932.

[11] J. Azaiez, B. Singh, Stability of miscible displacements of shear thinning fluids in a Hele-Shaw cell, Physics of Fluids 14 (5) (2002) 1557–1571. doi:10.1063/1.1462030.

[12] R. Sathyanath, Coating flows and features of liquids, suspensions, and polymers near porous substrates, Ph.D. thesis, Indian Institute of Technology Madras, Chennai, India (2011).

[13] R. B. Bird, R. C. Armstrong, O. Hassager, Dynamics of polymeric liquids. vol. 1, 2nd ed. : Fluid mechanics.

[14] N. Otsu, A threshold selection method from gray-level histograms, IEEE Transactions on Systems, Man, and Cybernetics 9 (1) (1979) 62–66. doi:10.1109/TSMC.1979.4310076.

[15] H. Shokri, M. H. Kayhani, M. Norouzi, Nonlinear simulation and linear stability analysis of viscous fingering instability of viscoelastic liquids, Physics of Fluids 29 (3) (2017) 033101. doi:10.1063/1.4977443.

[16] Y. Nagatsu, C. Iguchi, K. Matsuda, Y. Kato, Y. Tada, Miscible viscous fingering involving viscosity changes of the displacing fluid by chemical reactions, Physics of Fluids 22 (2) (2010) 024101. doi:10.1063/1.3301244.

[17] R. J. Poole, The Deborah and Weissenberg numbers, Rheology Bulletin 53 (2) (2012) 32–39.

[18] X. Cheng, J. H. McCoy, J. N. Israelachvili, I. Cohen, Imaging the microscopic structure of shear thinning and thickening colloidal suspensions, Science 333 (6047) (2011) 1276–1279. doi:10.1126/science.1207032.

[19] N. C. Crawford, L. B. Popp, K. E. Johns, L. M. Caire, B. N. Peterson, M. W. Liberatore, Shear thickening of corn starch suspensions: Does concentration matter?, Journal of Colloid and Interface Science 396 (2013) 83–89. doi:https://doi.org/10.1016/j.jcis.2013.01.024.

[20] A. Fall, N. Huang, F. Bertrand, G. Ovarlez, D. Bonn, Shear thickening of cornstarch suspensions as a reentrant jamming transition, Phys. Rev. Lett. 100 (2008) 018301. doi:10.1103/PhysRevLett.100.018301.

[21] A. J. Liu, S. R. Nagel, Jamming is not just cool any more, Nature 396 (6706) (1998) 21–22. doi:10.1038/23819.

[22] I. R. Peters, S. Majumdar, H. M. Jaeger, Direct observation of dynamic shear jamming in dense suspensions, Nature 532 (7598) (2016) 214–217. doi:10.1038/nature17167.

[23] L. Kondic, M. J. Shelley, P. Palffy-Muhoray, Non-Newtonian Hele-Shaw Flow and the Saffman-Taylor Instability, Phys. Rev. Lett. 80 (1998) 1433–1436. doi:10.1103/PhysRevLett.80.1433.

[24] S. Malhotra, M. M. Sharma, Impact of fluid elasticity on miscible viscous fingering, Chemical Engineering Science 117 (2014) 125–135. doi:https://doi.org/10.1016/j.ces.2014.06.023.

[25] S. Mora, M. Manna, From viscous fingering to elastic instabilities, Journal of Non-Newtonian Fluid Mechanics 173-174 (2012) 30–39. doi:https://doi.org/10.1016/j.jnnfm.2012.01.010.

[26] T. Sadhu, D. Dhar, Modelling proportionate growth, Current Science 103 (5) (2012) 512–517, full publication date: 10 September 2012.

[27] D. Dhar, T. Sadhu, A sandpile model for proportionate growth, Journal of Statistical Mechanics: Theory and Experiment 2013 (11) P11006. doi:10.1088/1742-5468/2013/11/p11006.

[28] K. Ghesmat, J. Azaiez, Viscous fingering instability in porous media: Effect of anisotropic velocity-dependent dispersion tensor, Transport in Porous Media 73 (3) (2008) 297–318. doi:10.1007/s11242-007-9171-y.

[29] S. J. Jackson, D. Stevens, H. Power, D. Giddings, A boundary element method for the solution of finite mobility ratio immiscible displacement in a Hele-Shaw cell, International Journal for Numerical Methods in Fluids 78 (9) (2015) 521–551. doi:https://doi.org/10.1002/fld.4028.

[30] K. A. Takeuchi, M. Sano, T. Sasamoto, H. Spohn, Growing interfaces uncover universal fluctuations behind scale invariance, Scientific Reports 1 (1) (2011) 34. doi:10.1038/srep00034.

[31] H. Li, B. Maini, J. Azaiez, Experimental and numerical analysis of the viscous fingering instability of shear-thinning fluids, The Canadian Journal of Chemical Engineering 84 (1) (2006) 52–62. doi:https://doi.org/10.1002/cjce.5450840109.

[32] S. Malhotra, M. M. Sharma, E. R. Lehman, Experimental study of the growth of mixing zone in miscible viscous fingering, Physics of Fluids 27 (1) (2015) 014105. doi:10.1063/1.4905581.

[33] N. Kagei, D. Kanie, M. Kawaguchi, Viscous fingering in shear thickening silica suspensions, Physics of Fluids 17 (5) (2005) 054103. doi:10.1063/1.1894407.

[34] S. Whitaker, Flow in porous media i: A theoretical derivation of darcy's law, Transport in Porous Media 1 (1) (1986) 3–25. doi:10.1007/BF01036523.

[35] C. T. Tan, G. M. Homsy, Stability of miscible displacements in porous media: Rectilinear flow, The Physics of Fluids 29 (11) (1986) 3549–3556. doi:10.1063/1.865832.

[36] M. T. Arigo, G. H. McKinley, The effects of viscoelasticity on the transient motion of a sphere in a shear-thinning fluid, Journal of Rheology 41 (1) (1997) 103–128. doi:10.1122/1.550803.

[37] M. A. Araújo, E. C. Ferreira, A. M. Cunha, M. Mota, Determination of diffusion coefficients of glycerol and glucose from starch based thermoplastic compounds on simulated physiological solution, Journal of Materials Science: Materials in Medicine 16 (3) (2005) 239–246. doi:10.1007/s10856-005-6685-0.

[38] X. Yu, A. R. Schmidt, L. A. Bello-Perez, S. J. Schmidt, Determination of the bulk moisture diffusion coefficient for corn starch using an automated water sorption instrument, Journal of Agricultural and Food Chemistry 56 (1) (2008) 50–58. doi:10.1021/jf071894a.

[39] J. L. Gaddis, T. C. A. III, R. L. Thomas, Ultrafiltration of gelatinous cornstarch suspensions, Separation Science and Technology 34 (6-7) (1999) 1253–1276. doi:10.1080/01496399908951092.

[40] I. Hopkinson, R. Jones, S. Black, D. Lane, P. McDonald, Fickian and case ii diffusion of water into amylose: A stray field nmr study, Carbohydrate Polymers 34 (1) (1997) 39–47. doi:https://doi.org/10.1016/S0144-8617(97)00106-9.

[41] S. L. Umbach, E. A. Davis, J. Gordon, P. T. Callaghan, Water self-diffusion coefficients and dielectric properties determined for starch-gluten-water mixtures heated by microwave by conventional methods, Cereal Chemistry 69 (1992) 637–642.

[42] A. Riaz, C. Pankiewitz, E. Meiburg, Linear stability of radial displacements in porous media: Influence of velocity-induced dispersion and concentration-

dependent diffusion, Physics of Fluids 16 (10) (2004) 3592–3598. doi:10.1063/1.1775431.

[43] F. Graf, E. Meiburg, C. Hartel, Density-driven instabilities of miscible fluids in a Hele-Shaw cell: linear stability analysis of the three-dimensional stokes equations, Journal of Fluid Mechanics 451 (2002) 261–282. doi:10.1017/S0022112001006516.

[44] S. Li, J. S. Lowengrub, J. Fontana, P. Palffy-Muhoray, Control of Viscous Fingering Patterns in a Radial Hele-Shaw Cell, Phys. Rev. Lett. 102 (2009) 174501. doi:10.1103/PhysRevLett.102.174501.

[45] T. Gao, M. Mirzadeh, P. Bai, K. M. Conforti, M. Z. Bazant, Active control of viscous fingering using electric fields, Nat. Commun. 10 (1) (2019) 4002. doi:10.1038/s41467-019-11939-7.

# Chapter 4

# Evolution of reverse fingers during radial displacement of a shear-thickening fluid

## 4.1 Introduction

An aqueous dense granular suspension of polydisperse irregular-shaped cornstarch (CS) particles in water exhibits shear-thinning and shear-thickening properties depending on the applied shear stress [1] and particle volume fraction [2]. As discussed in Chapter 1, while the organization of suspended particles, a constant hydrodynamic viscosity [2] and random particle collisions [3, 4] cause the shear-thinning of CS suspensions at low shear rate, frictional [5, 6] interactions between the constituent particles leads to shear-thickening at high shear rates. Measurements of the first normal stress difference $N_1$ [7] can indirectly shed light on the underlying inter-particle interactions contributing to the generation of large stresses in concentrated suspensions [8, 9]. While negative values of $N_1$ suggest hydrodynamic or lubrication effects in the suspension, positive $N_1$ values indicate the presence of inter-particle friction [8]. The further details about the flow regimes of CS suspensions under applied shear rates are discussed in section 1.2 of chapter 1.

Interfacial instabilities have been systematically investigated in non-Newtonian fluids with exotic nonlinear rheological responses such as shear-thinning, shear-thickening and non-zero yield stresses. Experiments involving the displacement of shear-thickening propylene glycol (PPG)-silica suspensions by air [10] demonstrated that the finger velocity deviates from the prediction of the modified Darcy's law [11] as the injection pressure is increased. When a silica suspension was displaced by air at a shear rate exceeding the critical value necessary to initiate suspension shear thickening, a transition from a stable pattern to viscous fingering (VF) instability was observed [12]. Another report on the displacement of shear-thickening cornstarch suspensions by air reported an excellent correlation between suspension rheology and the observed interfacial pattern morphologies [13]. This work demonstrated that interfacial pattern morphologies change with increasing injection pressures as the cornstarch suspension transitions from one flow regime to another. While earlier research work focussed on the miscible displacements of shear-thinning cornstarch suspensions [14] and the immiscible displacements of shear-thickening suspensions [10, 12, 13, 15], the miscible displacement of shear-thickening suspensions has never been investigated experimentally to the best of our knowledge.

In chapter 3 on the miscible displacement of cornstarch suspensions in the shear-thinning regime, we showed that increasing the elasticity of the suspension and viscosity ratio of the fluid pair resulted in the suppression of interfacial instability [14]. In the present chapter, we explore the influence of the shear-thickening rheology of a dense cornstarch suspension (displaced fluid) on the onset and growth of interfacial instabilities during its radial displacement by water (inner fluid) in a quasi-two-dimensional Hele-Shaw (HS) cell. While the existing literature on the study of instabilities focusses exclusively on the propagation of the inner fluid front at the interface between the inner and displaced fluids, our present work observes two growing interfaces simultaneously in a single experiment, *viz.*, the inner interface between water and displaced cornstarch suspension, and the outer interface between

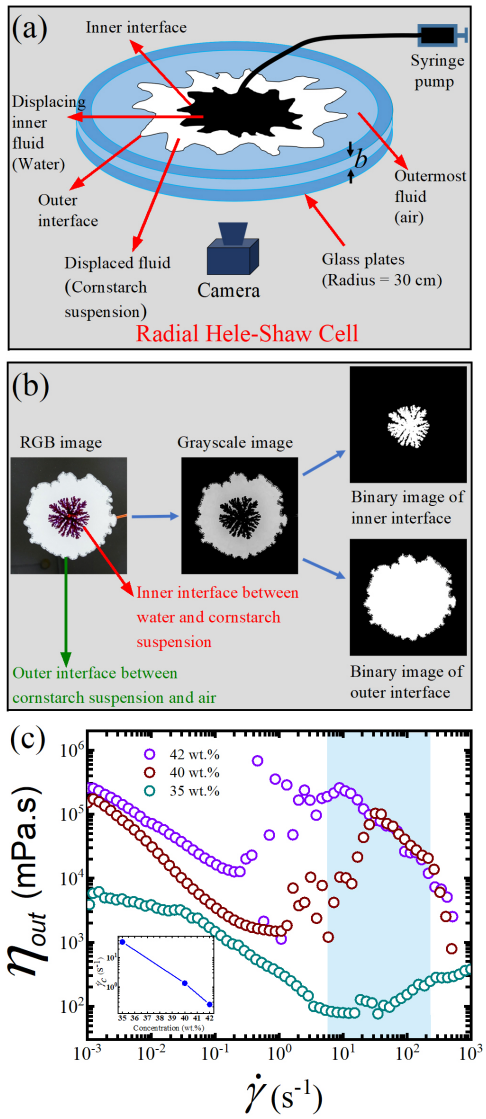



**Fig. 4.1:** **(a)** Schematic illustration of a radial Hele-Shaw (HS) cell. **(b)** Binarization steps for detecting the inner interface between water (inner fluid) and cornstarch (CS) suspension (displaced fluid), and the outer interface between cornstarch suspension and air (outermost fluid). **(c)** Viscosity $\eta_{out}$ vs. shear rate $\dot{\gamma}$ for aqueous cornstarch suspensions of different concentrations at a plate separation of 300 $\mu$m. The region highlighted in blue indicates the shear-thickening flow regime of a 40 wt.% cornstarch suspension. Inset shows the variation in critical shear rate $\dot{\gamma}_c$ for the onset of shear-thickening as a function of concentration of the CS suspension.

cornstarch suspension and air (outermost fluid). Interestingly, we observe a transient withdrawal of the cornstarch suspension and the evolution of reverse fingers at the outer interface during displacement of the suspension by water at large injection

flow rates. We attribute this phenomenon to the build-up of normal stresses in the highly sheared dense cornstarch suspension. We demonstrate that the generation of reverse fingers depends sensitively on injection flow rate, concentration of the cornstarch suspension and gap of the HS cell. We quantify the formation of reverse fingers by estimating the perimeter of the pattern at the outer interface ($\Delta P_{out}$), the number of reverse fingers ($N_{rf}$) and the average spacing between these fingers ($\lambda$). Furthermore, we report a clear correlation in the interfacial dynamics at the inner and outer interfaces. Finally, we show that the emergence of reverse fingers at the outer interface reduces the efficiency of displacement of the cornstarch suspension.

## 4.2 Materials and Methods

A radial Hele-Shaw (HS) cell setup (Fig. 4.1(a), section 2.3.2 in chapter 2), is used to study the displacement of a dense cornstarch suspension by water. Teflon spacers of thicknesses 170 $\mu$m, 300 $\mu$m, 500 $\mu$m and 800 $\mu$m are used to maintain a constant gap between the glass plates. The fluids are injected with a syringe pump (NE-8000, New Era Pump Systems, USA) through a 3 mm hole drilled at the centre of the top plate. The sample preparation protocols of cornstarch suspension are provided in the section 2.2.1 of chapter 2. To perform displacement experiments, the homogeneous cornstarch suspension is first loaded in the radial HS cell until its boundary reaches approximately 10 cm from the injection point. After loading the cornstarch suspension, Milli-Q water (Millipore Corp., resistivity 18.2 M$\Omega$.cm), dyed with rhodamine B (Sigma-Aldrich) for enhancing the contrast at the interface, is injected into the HS cell as the inner displacing fluid at a controlled injection flow rate $q$. The growth of interfacial patterns is recorded using a DSLR camera (D5200, Nikon, Japan) with a spatial resolution of 1920×1080 pixels (one-pixel area = $2.2 \times 10^{-3}$ cm$^2$) and a frame rate of 30 fps. The obtained stack of images is converted to grayscale format and analysed using the MATLAB@2021 image processing toolbox. The procedure for binarization of raw images is shown in Fig. 4.1(b). Snapshots

of raw images corresponding to the temporal evolution of interfacial patterns are shown in Fig. 4.2. A stress-controlled rheometer (Anton Paar, MCR 702) is used to perform rheological measurements in a parallel plate geometry (PP50) at different plate separations. Figure 4.1(c) shows the plots of the measured viscosities $\eta_{out}$ versus applied rotational shear rates $\dot{\gamma}$ for dense cornstarch suspensions of different concentrations at a plate separation of 300 $\mu$m. Shear-thickening, an increase in the viscosity of the fluid with increasing $\dot{\gamma}$ above a critical shear rate $\dot{\gamma}_c$ [16], is prominent in the CS suspensions prepared at high concentrations. We observe from the inset of

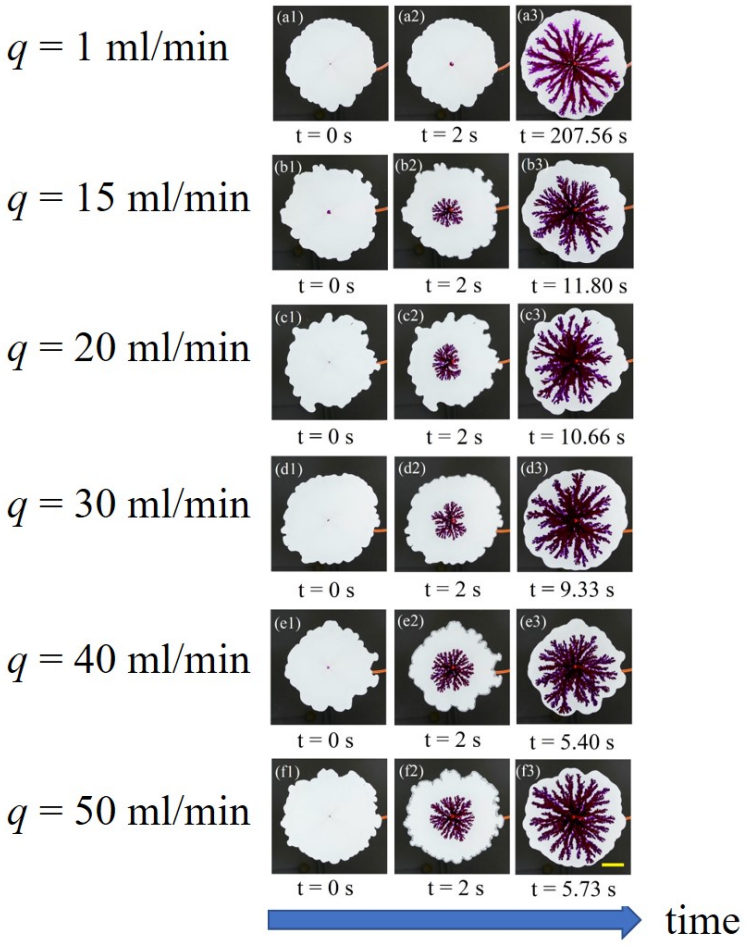



**Fig. 4.2:** Raw RGB images showing the temporal evolution of interfacial patterns obtained during radial displacements of an aqueous 40 wt.% cornstarch suspension by water at different flow rates: **(a)** $q = 1$ ml/min **(b)** 15 ml/min **(c)** 20 ml/min **(d)** 30 ml/min **(e)** 40 ml/min **(f)** 50 ml/min. The scale bar is 5 cm. The HS cell gap $b$ in these experiments is kept fixed at 170 $\mu$m.

Fig. 4.1(c) that $\dot{\gamma}_c$ decreases with increase in concentration of the CS suspension [16]. We note that the observed decrease in the viscosities of 40 wt.% and 42 wt.% CS suspensions at very high shear rates arises due to the slippage of the dense CS suspensions at the stainless steel rheometer plates. All the displacement experiments and rheological measurements are performed at room temperature (25°C).

### 4.2.1 Calculations

We estimate the shear rate $\dot{\gamma}$ imposed by water (the inner fluid) on the cornstarch (CS) suspension (displaced fluid) during displacement of the latter in the Hele-Shaw cell. The shear rate imposed by a propagating finger-tip is computed using $\dot{\gamma}= 2U/b$ [17], where $U$ is the characteristic radial propagation velocity of the interfacial finger-tips and $b$ is the gap of the Hele-Shaw cell. The finger-tip velocity, $U$, was estimated by tracking the temporal propagation of finger-tips at the inner interface using video imaging. Since each finger-tip in a pattern experiences a different local shear rate, an average over multiple finger-tips is calculated to estimate $\dot{\gamma}$ values for

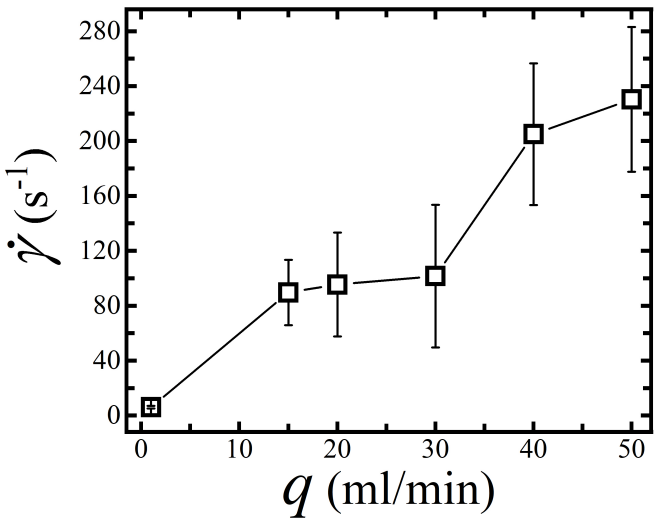



**Fig. 4.3:** Shear rates $\dot{\gamma}$ computed for various injection flow rates $q$ of the inner fluid (water) during radial displacement of an aqueous 40 wt.% cornstarch suspension in a Hele-Shaw cell of gap $b = 170$ $\mu$m. Error bars represent the standard deviations in measurements of shear rates for multiple tips.

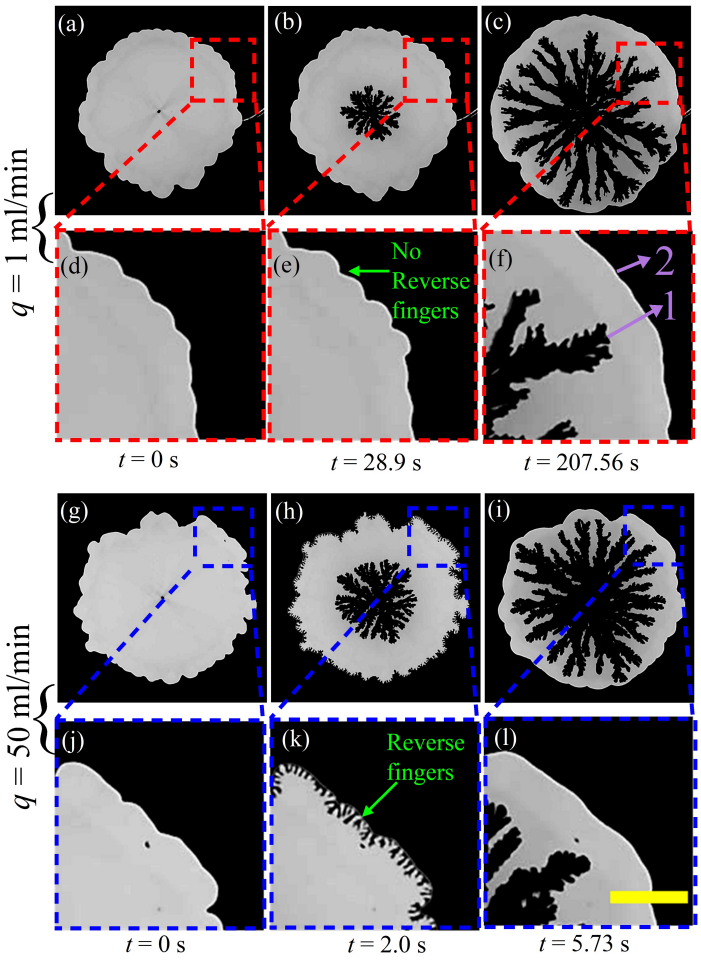



**Fig. 4.4: (a-c)** Patterns in grayscale formed during the displacement of a 40 wt.% cornstarch suspension (displaced fluid) by water (inner fluid) at injection flow rate $q = 1$ ml/min at different times of their growth. **(d-f)** Zoomed images of the patterns within the red-coloured boxes in (a-c) are displayed. The inner interface between water and cornstarch suspension, and the outer interface between cornstarch suspension and air (outermost fluid) are indicated by numbers 1 and 2 respectively in (f). **(g-i)** Patterns in grayscale for injection flow rate $q = 50$ ml/min. **(j-l)** Zoomed images of the patterns within the blue-coloured boxes in (g-i) are displayed. The scale bar is 3 cm. The HS cell gap is 170 $\mu$m.

different injection flow rate experiments (Fig. 4.3). The estimated values of $\dot{\gamma}$ vary from $6.01 \pm 0.95$ s$^{-1}$ to $230.35 \pm 52.72$ s$^{-1}$ for the displacement of a dense 40 wt.% CS suspension and lie above the critical shear rate $\dot{\gamma}_c = 1.33$ s$^{-1}$ required for the onset of shear-thickening behaviour (shaded region in Fig. 4.1(c)).

## 4.3 Results & Discussions

Figures 4.4(a-c) display grayscale images showing the temporal evolution of interfacial patterns during the displacement of an aqueous 40 wt.% cornstarch (CS) suspension (displaced fluid) by water (inner fluid) at a low injection flow rate $q$ = 1 ml/min for a HS cell gap $b = 170$ $\mu$m. The magnified images of the interfacial regions enclosed in red boxes in Figs. 4.4(a-c) are shown in Figs. 4.4(d-f). In this work, we simultaneously explore the growth of two interfaces: the inner interface between water and the CS suspension (inner interface labelled as 1 in Fig. 4.4(f)) and the outer interface between CS suspension and air (outer interface labelled as 2 in Fig. 4.4(f)). The growth of the inner interface due to outward displacement of the CS suspension involves the appearance of fingers undergoing multiple tip-splitting events, as seen in Figs. 4.4(b-c). Figures 4.4(g-i) show grayscale images of the temporal evolution of interfacial patterns during the displacement of a 40 wt.% CS suspension by water at a very high injection flow rate $q = 50$ ml/min. Interestingly, we note the transient withdrawal of the CS suspension during its displacement at high injection flow rates (Fig. 4.4(h)). This withdrawal process results in the invasion of air (outermost fluid) into the cornstarch suspension and the development of reverse fingers at the outer interface (Fig. 4.4(h)) between the CS suspension and air. Magnified images of the regions enclosed in blue boxes in Figs. 4.4(g-i) are displayed in Figs. 4.4(j-l). The reverse fingers appear for a very short time, and the outer interface eventually becomes smooth at later stages regardless of the applied injection flow rate (Fig. 4.4(l)).

We next quantify the morphologies and growth of the inner and outer interfaces (Fig. 4.5). It is seen from Fig. 4.5(a) that the perimeter of the inner interface, $P_{in}$, increases monotonically with time (Fig. 4.5(a)) showing very rapid initial growth, followed by a significant slowing down at later times. The perimeter of the outer interface is defined as $\Delta P_{out} = P_{out}(t) - P_{out}(0)$ where $P_{out}(t)$ and $P_{out}(0)$ are perimeters of the outer interface at times $t$ and $t = 0$ s respectively, with $t = 0$ s corresponding

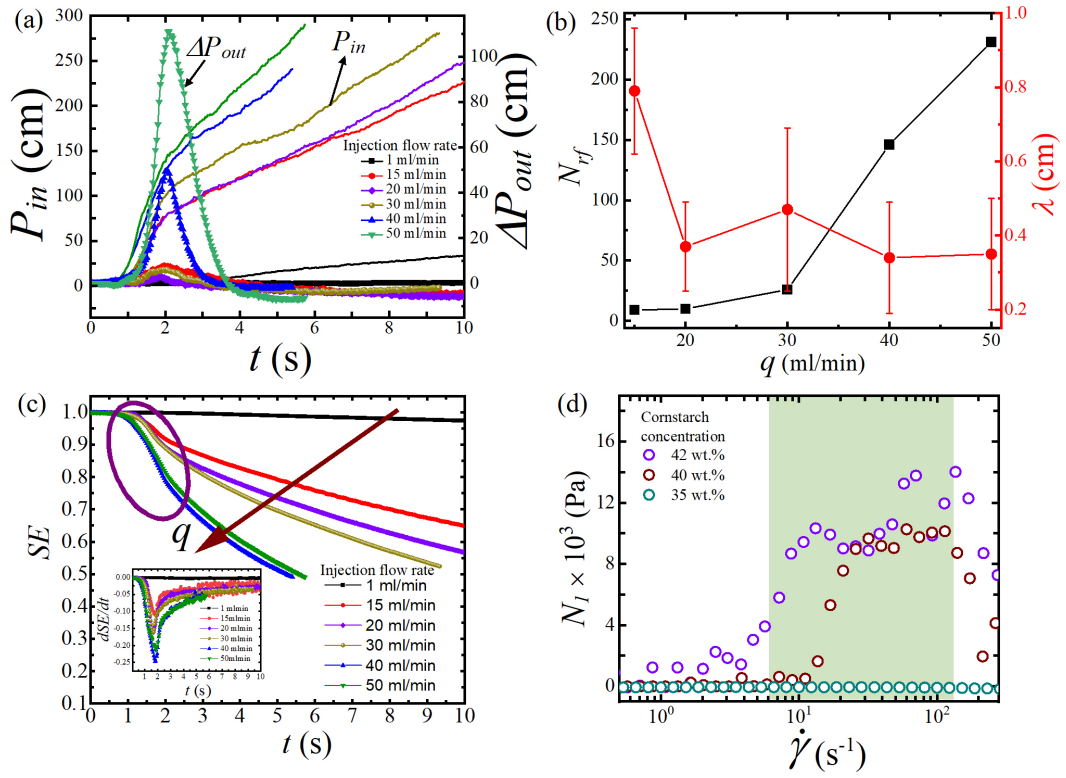



**Fig. 4.5:** **(a)** Perimeters of inner interfaces $P_{in}$ (solid lines) and outer interfaces $\Delta P_{out} = P_{out}(t) - P_{out}(0)$ (filled symbols connected by solid lines) vs. time $t$ where $P_{out}(t)$ and $P_{out}(0)$ are perimeters at times $t$ and $t = 0$ s respectively at various injection flow rates, with $t = 0$ s corresponding to the time of injection of the inner fluid (water). **(b)** Number of reverse fingers $N_{rf}$ (■) and average reverse finger spacing $\lambda$ (●) as a function of injection flow rate $q$. **(c)** Sweep efficiency $SE$ vs. time $t$ for different injection flow rates of the inner fluid. A purple ellipse highlights the sharp decrease in $SE$ due to the generation of reverse fingers. Inset shows $dSE/dt$ vs. time. **(d)** First normal stress difference $N_1$ vs. applied shear rate for cornstarch suspensions of different concentrations measured in a stress-controlled rheometer at a plate separation of 300 $\mu$m in a parallel plate experimental geometry. The shear rates imposed by the inner fluid in the HS cell experiments at various injection flow rates, estimated as described in section 4.2.1, lie in the region highlighted in green.

to the time of injection of water (inner fluid). While $\Delta P_{out}$ does not change appreciably for low injection flow rates of water, we note that it shows a non-monotonic variation with time for high injection flow rates. The initial rapid increase in $\Delta P_{out}$ for high injection flow rates is due to the formation of reverse fingers at the outer interface between the cornstarch suspension and air. After reaching a maximum, the subsequent decrease in $\Delta P_{out}$ is attributed to the fading of reverse fingers at

later times. We note from Fig. 4.5(a) that changes in the slopes of $P_{in}$ and $\Delta P_{out}$ occur at almost the same time, thereby indicating a strong correlation in the growth kinetics of the inner and outer interfaces. The variations in the time derivatives of $P_{in}$ and $\Delta P_{out}$, *i.e.* in the growth rates of the inner and outer interfaces, further confirm this correlation (Fig. 4.6). Such close correlation between the dynamics of the interfaces 1 and 2 (Fig. 4.4(f)) suggests that the stresses generated within the dense cornstarch suspension during its displacement by the inner fluid are also transmitted to the outer interface between the CS suspension and air.

We note that reverse fingers only appear for injection flow rates $q$ larger than 1 ml/min. The global features of the outer interface are next quantified by computing the number of reverse fingers, $N_{rf}$, and the average spacing between reverse fingers, $\lambda$, for different injection flow rates of water (15 ml/min $\leq q \leq$ 50 ml/min, Fig. 4.5(b)). The number of reverse fingers is estimated by identifying all the tips of the reverse fingering pattern at the outer interface when the transient reverse fingers reach their maximum lengths. Since the occurrence of reverse fingers is pronounced for high injection flow rates, therefore $N_{rf}$ increases with an increase in injection flow rate (Fig. 4.5(b)). The average spacing between the reverse fingers

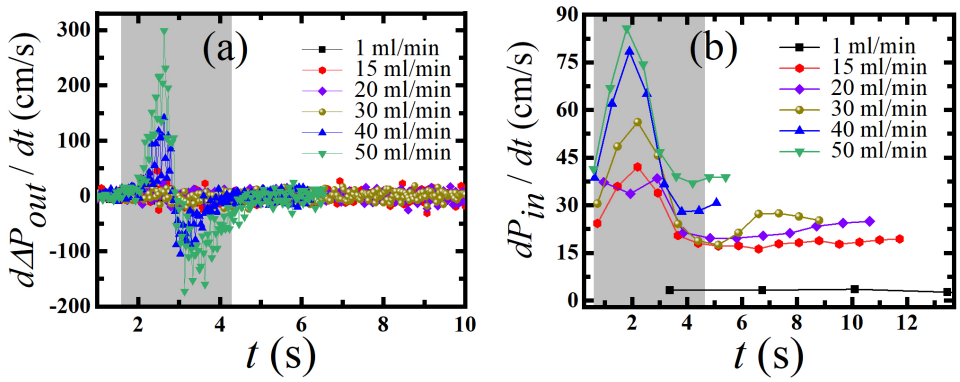



**Fig. 4.6:** **(a)** $d\Delta P_{out}/dt$ vs. $t$ for various injection flow rates $q$. **(b)** $dP_{in}/dt$ vs. $t$ for various injection flow rates. The changes in the slopes of $d\Delta P_{out}/dt$ and $dP_{in}/dt$ occur during the same time interval (shown by grey shaded regions) and represent the underlying correlation in the growth kinetics of the inner and outer interfacial patterns. The HS cell gap in these experiments is kept fixed at $b = 170$ $\mu$m and the concentration of the CS suspension is 40 wt.%.

is estimated as $\lambda = < \sqrt{(r_1)^2 + (r_2)^2 + 2r_1 r_2 \cos(\theta_1 - \theta_2)} >_{N_{rf}-1}$, where $r$ and $\theta$ are polar coordinates corresponding to the tips of the reverse fingers and $< ... >_{N_{rf}-1}$ denotes an average over the estimated spacings between all the adjacent reverse finger-tips (Fig. 4.5(b)). The average reverse finger spacing $\lambda$ does not show any significant dependence on the injection flow rates explored in our experiments. The calculations of $N_{rf}$ and $\lambda$ are shown in Fig. 4.7.

Sweep efficiency ($SE$) is a non-dimensional parameter often used to determine how effectively one fluid displaces another [14, 18]. By following the protocols adopted in chapter 3 (section 3.2.1), we estimate $SE$ of the displaced cornstarch suspension by computing the ratio of the area contacted by the inner fluid (water; black area in Fig. 4.1(a)) and the total area occupied by the inner and displaced fluids (sum of the black and white areas in Fig. 4.1(a)). Figure 4.5(c) shows the variation in sweep efficiency with time for all the injection flow rates $q$ used in our experiments. Before the onset of pattern growth at the inner interface at the earliest times, we observe that $SE$ is close to unity for all $q$ values. This is followed by a decrease in $SE$ for the higher flow rates as the interfacial patterns evolve at later times. The initial sharp drops of $SE$ values occur at the same times when reverse fingers are observed (highlighted by a purple ellipse in Fig. 4.5(c)). This is also evident from the slopes of the $SE$ vs. $t$, $dSE/dt$ shown in the inset of Fig. 4.5(c), thereby confirming that the presence of reverse fingers significantly affects sweep efficiency during displacement of the highly sheared cornstarch suspension.

It has been predicted in non-linear simulations that non-zero normal stresses in a viscoelastic fluid lead to significantly higher stress asymmetries along the flow direction when compared to the normal direction [18]. These stress asymmetries result in an effective drag force along the flow direction. Figure 4.5(d) displays the rapid increase in the first normal stress difference $N_1$ with shear rate for the higher cornstarch suspension concentrations. The observed decrease in $N_1$ at very high shear rates can be attributed to slip [7, 19, 20] between the extremely dense CS suspension and the rheometer plates due to the imposition of large tangential strains.

It is important to note that such slippage-induced decreases in $N_1$ (Fig. 4.5(d)) and $\eta_{out}$ (Fig. 4.1(c)) are observed at comparable shear rates. However, as confirmed

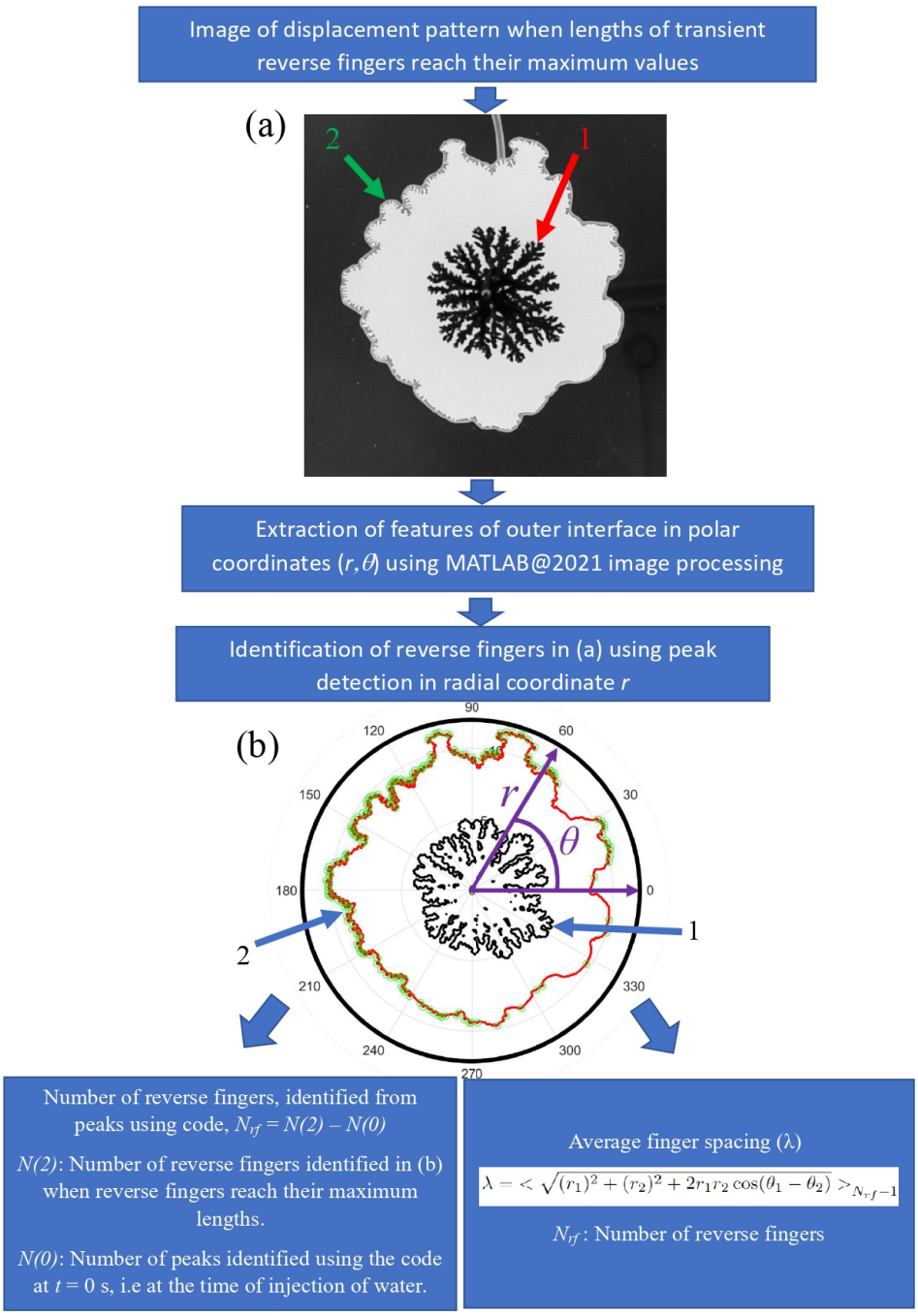



**Fig. 4.7:** Flow chart illustrating the procedure for calculation of the number of reverse fingers $N_{rf}$ and the average spacing $\lambda$ between them. Label 1 in (a-b) represents the inner interface between water and cornstarch suspension. Label 2 in (a-b) represents the outer interface between cornstarch suspension and air.

from the temporal variations of the perimeters ($P_{in}$ and $\Delta P_{out}$) of the interfaces (Fig. 4.5(a)), we do not observe any intermittent changes in growth profiles of the inner and outer interfaces in the HS cell. We therefore expect minimal or no slippage between the suspension and HS glass plates in our displacement experiments. It was reported earlier that the sign of $N_1$ depends on the details of the particle-particle interactions in shear-thickened suspensions of colloidal silica [8] and granular cornstarch [9, 21]. While negative values of $N_1$ represent hydrodynamic or lubrication effects, positive values of $N_1$ reflect the dominant influence of inter-particle friction [8]. In our experiments, the measured values of $N_1$ (Fig. 4.5(d)) at the imposed shear rates are always positive, indicating that inter-particle friction at the microscopic scale determines the rheology of granular cornstarch suspensions. We therefore believe that stress anisotropies in our system arise due to the formation of anisotropic force chains [22–24] supported by inter-particle friction in the sheared granular cornstarch suspension. This results in the large positive values of $N_1$ observed here [9, 21]. Therefore, the large buildup of normal stresses in CS suspensions under high shear rates causes an effective drag in the flow direction and results in the formation of reverse fingers in our displacement experiments. A recent study reported a characteristic time of a few seconds for the applied stresses to propagate across highly sheared cornstarch suspensions undergoing discontinuous shear-thickening [25]. These stresses are anisotropically transmitted via particle-particle contacts in sheared forced networks that form and break under large shear rates. We therefore note that the observed maximum growth of transient reverse fingers at timescales $\approx$ a few seconds for appropriately high injection flow rates (as seen from the peak positions of $\Delta P_{out}$ in Fig. 4.5(a)) coincides approximately with the expected time interval for the propagation of stresses through force networks in the suspension. The subsequent rearrangement of these force networks at later times results in the disappearance of the observed reverse fingers.

As seen in Fig. 4.8(a), the occurrence of reverse fingers is not always axisymmetric at the outer interface between the cornstarch suspension and air. We further analyse

the reverse fingering patterns for high injection flow rates by dividing each image into eight octants, with each octant labelled by a unique number between 1 and 8 as shown in Fig. 4.8(a). For each octant, the number of reverse fingers, $n_{rf}$, at the outer interface and the longest finger length, $R$, of the inner pattern are estimated. The longest finger length in the inner pattern, $R$, varies appreciably in the different octants and is approximately inversely proportional to $n_{rf}$ as seen in Fig. 4.8(b). This indicates that growth of the inner pattern is comparatively slower in the interfacial sections having more reverse fingers $n_{rf}$. While we may expect a decrease in the finger spacing $\lambda$ with an increasing number of equally distributed reverse fingers, we note that the constant value of $\lambda$ with changing $q$ as seen in Fig. 4.5(b) also indirectly indicates that the reverse fingers are not necessarily axisymmetric (Fig. 4.8(a)). It seems reasonable to conclude that the anisotropic build-up of normal stresses [22–24] in the displaced cornstarch suspension causes unequal drag forces in the sample. These drag forces lead to the observed slower growth of the propagating finger-tips of the inner pattern in certain sections, an

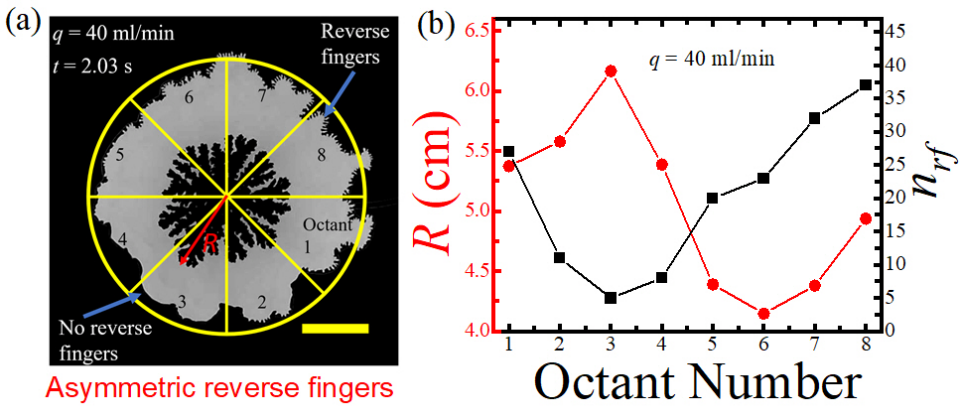



**Fig. 4.8:** **(a)** Interfacial pattern obtained during the radial displacement of a cornstarch suspension (40 wt.%) by water at $q = 40$ ml/min for HS cell gap $b = 170$ $\mu$m. The scale bar is 5 cm. Formation of reverse fingers is not axisymmetric in the different interfacial sections. Yellow lines divide the pattern into octants, which are labelled from numbers 1 to 8. $R$ is the length of the longest finger of the inner pattern between the cornstarch suspension and water and $n_{rf}$ is the number of reverse fingers in an octant. **(b)** The longest finger length $R$ and the number of reverse fingers $n_{rf}$ in each octant of the pattern displayed in (a) vs. octant number.

effective withdrawal of the cornstarch suspension, and the generation of pronounced reverse fingers at the outer interface.

We next investigate the effect of confinement on the reverse fingering patterns when a dense cornstarch suspension (40 wt.%) is displaced by water at a fixed injection flow rate $q = 50$ ml/min in a Hele-Shaw cell with gaps $b$ varying between 170 $\mu$m to 500 $\mu$m (Figs. 4.9(a-c)). We see the formation of reverse fingers for the lower HS cell gaps (HS cell gap $b = 170$ and 300 $\mu$m, Figs. 4.9(a-b)), but observe only a slight withdrawal of the outer interface and the absence of reverse finger formation at $b = 500$ $\mu$m (Fig. 4.9(c)). When $b$ is increased to 800 $\mu$m, we note that water, the inner fluid, spreads over the cornstarch suspension rather than displacing it. We next quantify the effects of confinement on the onset and growth of the patterns at the inner and outer interfaces by estimating the pattern perimeters $P_{in}$

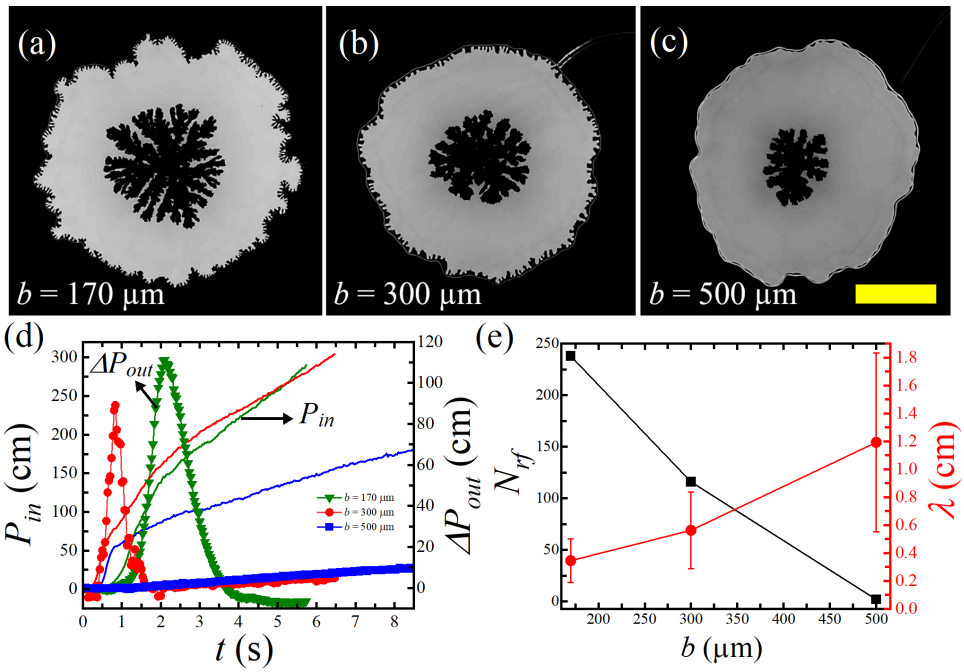



**Fig. 4.9:** Interfacial patterns obtained during the displacement of a 40 wt.% cornstarch suspension by water at $q = 50$ ml/min for different gaps $b$ of the Hele-Shaw (HS) cell: **(a)** $b = 170$ $\mu$m, **(b)** $b = 300$ $\mu$m and **(c)** $b = 500$ $\mu$m. The scale bar is 5 cm. **(d)** Perimeters of inner interfaces $P_{in}$ (solid lines) and outer interfaces $\Delta P_{out}$ (filled symbols connected by solid lines) for different gaps $b$. **(e)** Number of reverse fingers $N_{rf}$ (■) and average reverse finger spacing $\lambda$ (●) at the outer interface as a function of $b$.

and $\Delta P_{out}$, number of reverse fingers $N_{rf}$ and average reverse finger spacing $\lambda$ for different values of $b$. As reported by us for pattern formation at a fixed HS cell gap and different injection flow rates (Fig. 4.5(a)), $P_{in}$ increases monotonically with time and shows a change in slope at intermediate times while $\Delta P_{out}$ shows non-monotonic time-dependence (Fig. 4.9(d)) for the smaller HS cell gaps. Decrease in the peak values of $\Delta P_{out}$ with $b$ (Fig. 4.9(d)) is a consequence of a decrease in the number of reverse fingers $N_{rf}$ (Fig. 4.9(e)) with the removal of confinement. Simultaneously, $\lambda$ is seen to increase with $b$ (Fig. 4.9(e)). As demonstrated earlier, the formation of reverse fingers is sensitively dependent on the first normal stress difference $N_1$. Our rheometric measurements reveal that $N_1$ decreases steadily with increasing gap thickness of the rheometer plates (Fig. 4.10). This is consistent with previous work that highlighted the increasingly strong shear-thickening rheology of cornstarch suspensions with decreasing plate separations [16]. The large values of $N_1$ at low rheometer plate separations indicate that confined geometries are necessary for the generation of reverse fingers.

We therefore conclude that the formation of reverse fingers at the outer interface requires the build-up of large normal stresses in the cornstarch suspension and can be achieved either by increasing the injection flow rate of the inner fluid or by decreasing the gap of the HS cell. The important role of the first normal stress difference in the generation of reverse fingers is further confirmed by increasing the concentration and therefore the elasticity [14] of the displaced cornstarch suspension. Figures 4.11(a-c) display grayscale images of the interfacial patterns formed when water injected at an injection flow rate $q = 50$ ml/min displaces cornstarch suspensions of different concentrations in a Hele-Shaw cell of gap $b = 170$ $\mu$m. While reverse fingering is observed when cornstarch suspensions of higher concentrations are displaced by water, it is absent when a cornstarch suspension of a lower concentration (35 wt.%) is displaced at the same injection flow rate. The higher peak value of the outer perimeter $\Delta P_{out}$ and its non-monotonic evolution with time at the highest concentration (42 wt.%; Fig. 4.11(d)) indicates the enhanced formation

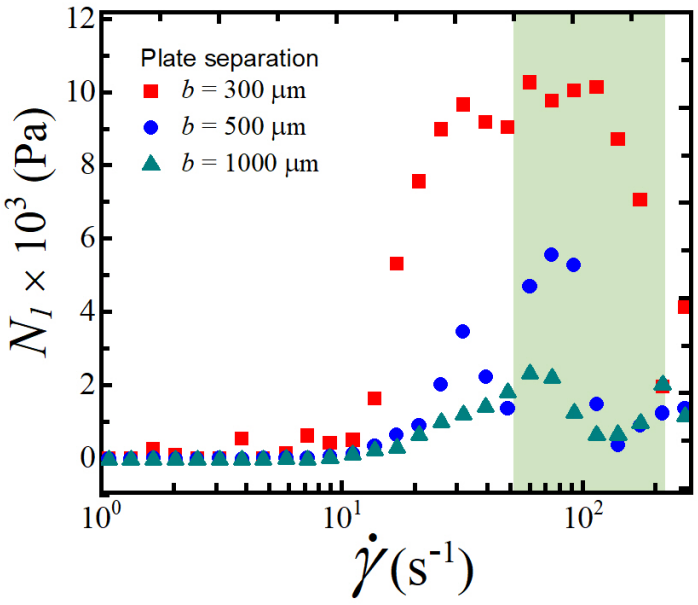



**Fig. 4.10:** First normal stress difference $N_1$ vs. shear rate for a 40 wt.% cornstarch suspension measured for different plate separations in the rheometer. The highlighted region indicates the shear rate range explored in the displacement experiments for various gaps of the HS cell.

of reverse fingers at the outer interface. The variations in the time derivatives of $P_{in}$ and $\Delta P_{out}$ (Fig. 4.11(e-f)), *i.e.* in the growth rates of the inner and outer interfaces, indicate correlation in the growth kinetics of the inner and outer interfaces. We conclude by noting that the time-evolutions of $P_{in}$ and $\Delta P_{out}$ qualitatively follow the same trend regardless of whether cornstarch suspensions of increasing concentrations are displaced at a fixed injection flow rate (Fig. 4.11(d)) or a cornstarch suspension of fixed concentration is displaced at increasing injection flow rates (Fig. 4.5(a)).

## 4.4 Conclusions

Dense aqueous granular cornstarch (CS) suspensions display shear-thinning and shear-thickening flows when externally applied shear stresses and particle concentrations are varied appropriately [1]. It is now well-known that hydrodynamic lubrication forces and the formation of anisotropic force chain networks govern the

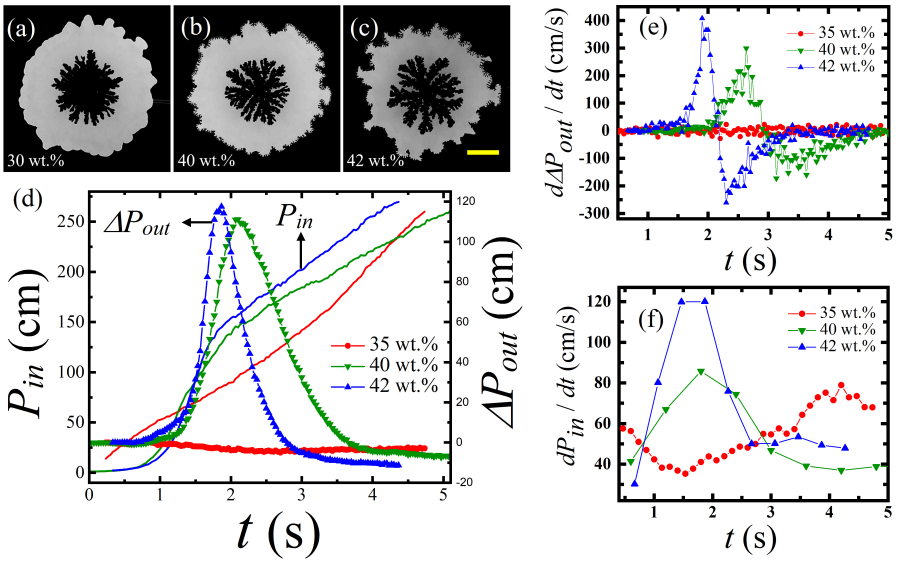



**Fig. 4.11:** Interfacial patterns formed by the displacement of cornstarch suspensions of various concentrations: (a) 35 wt.% (b) 40 wt.% (c) 42 wt.% at time $t = 2$ s after injection of water at $q = 50$ ml/min in the HS cell of gap $b = 170$ $\mu$m. The scale bar is 5 cm. (d) Perimeters of the inner interfaces $P_{in}$ (solid lines) and outer interfaces $\Delta P_{out}$ (filled symbols connected by solid lines) vs. time $t$ for the above cornstarch suspensions. (e) $d\Delta P_{out}/dt$ vs. $t$ and (f) $dP_{in}/dt$ vs. $t$.

unique rheology of cornstarch suspensions [1, 2, 23, 24, 26]. The spatially anisotropic stresses arising from the formation of force chain networks [22, 23, 26] at large shear rates should influence the displacement efficiency [18] of a dense shear-thickening cornstarch suspension in a Hele-Shaw (HS) cell. In this work, we investigate miscible displacements of confined shear-thickening cornstarch (CS) suspensions (displaced fluid) when the shear rates imposed on the suspension are greater than the critical shear rate $\dot{\gamma}_c$ required for the onset of shear-thickening. Displacement of dense CS suspensions at large shear rates are achieved by systematically varying injection flow rate of the displacing inner fluid (water) and gap of the HS cell. We note that previous literature focussed exclusively on the propagation of the inner fluid front at the inner fluid-fluid interface [13, 14, 27–32]. Besides monitoring the generation of viscous fingers at the inner interface between water and the CS suspension, we report here an unexpected growth of transient reverse fingers at the outer interface between the CS suspension and air (outermost fluid) at sufficiently high injection flow rates.

Our observation of an inverse relation between the number of reverse fingers at the outer interface and the growth of the inner pattern establishes the presence of a strong correlation between the growth kinetics of the two interfaces. Our rheometric measurements of large positive values of the first normal stress difference in dense cornstarch suspensions at large applied shear rates ($\dot{\gamma} \geq \dot{\gamma}_c$) indicate inter-particle frictional interactions [5, 8] and the generation of shear-induced anisotropic force chain networks [22, 23, 26]. We believe that the anisotropic stress profiles that are generated in the highly-sheared CS suspension are responsible for the observed emergence of reverse fingers at the outer interface. We also note the enhanced formation of reverse fingers for low gap widths of the HS cell and high concentrations of the CS suspensions. Since our rheology experiments clearly demonstrate that normal stresses in the CS suspension increase with decreasing gap of the HS cell [16] and increasing suspension concentration [8], our results verify the important contribution of normal stresses in pattern formation during the displacement of viscoelastic suspensions in confined geometries. The magnitude of the normal stresses generated in viscoelastic fluids such as in emulsions [33] and polymeric solutions [34] are strongly dependent on their individual internal microstructures. In order to thoroughly investigate the relation between normal stresses, sample microstructures and morphologies of interfacial displacement patterns, it would be interesting to systematically perform displacement experiments with different materials and externally imposed shear profiles.

We report the first experimental observation of reverse fingers at the outer interface between a highly sheared CS suspension and air during miscible displacement of the suspension by water. Since displacement efficiency [18] depends on the morphologies of the inner and outer interfaces, we observe a sharp decrease in sweep efficiency due to the generation of reverse fingers at the outer interface. The role of shear-dependent rheology in determining the morphologies of interfacial patterns formed during the displacement of a more viscous fluid by a less viscous one is of fundamental and practical interest. Besides being fascinating from a fluid mechanics

point of view, the understanding of interfacial instabilities can be useful in many areas such as hydrology [35], oil recovery by water flooding [36], in enhancing the mixing of fluids [37, 38], while fabricating structured soft materials [39] and in the control of dendritic growth morphologies in rechargeable batteries [40]. The present work can also have useful implications in cementing processes involving the removal of drilling mud and its substitution with cement slurries [41].

# References


[1] I. R. Peters, S. Majumdar, H. M. Jaeger, Direct observation of dynamic shear jamming in dense suspensions, Nature 532 (7598) (2016) 214–217. doi:10.1038/nature17167.

[2] N. J. Wagner, J. F. Brady, Shear thickening in colloidal dispersions, Physics Today 62 (10) (2009) 27–32. doi:10.1063/1.3248476.

[3] X. Cheng, J. H. McCoy, J. N. Israelachvili, I. Cohen, Imaging the microscopic structure of shear thinning and thickening colloidal suspensions, Science 333 (6047) (2011) 1276–1279. doi:10.1126/science.1207032.

[4] N. C. Crawford, L. B. Popp, K. E. Johns, L. M. Caire, B. N. Peterson, M. W. Liberatore, Shear thickening of corn starch suspensions: Does concentration matter?, Journal of Colloid and Interface Science 396 (2013) 83–89. doi:https://doi.org/10.1016/j.jcis.2013.01.024.

[5] R. Seto, R. Mari, J. F. Morris, M. M. Denn, Discontinuous shear thickening of frictional hard-sphere suspensions, Phys. Rev. Lett. 111 (2013) 218301. doi:10.1103/PhysRevLett.111.218301.

[6] M. Wyart, M. E. Cates, Discontinuous Shear Thickening without Inertia in Dense Non-Brownian Suspensions, Phys. Rev. Lett. 112 (2014) 098302. doi:10.1103/PhysRevLett.112.098302.

[7] C. W. Macosko, Rheology: Principles, Measurements, and Applications, VCH Publishes, New York, 1994.

[8] M. M. Denn, J. F. Morris, D. Bonn, Shear thickening in concentrated suspensions of smooth spheres in Newtonian suspending fluids, Soft Matter 14 (2018) 170–184. doi:10.1039/c7sm00761b.

[9] S. Jamali, E. Del Gado, J. F. Morris, Rheology discussions: The physics of dense suspensions, Journal of Rheology 64 (6) (2020) 1501–1524. doi:10.1122/8.0000174.

[10] M. Kawaguchi, Viscous Fingering of Silica Suspensions Dispersed in Polymer Fluids. In: Pojman J.A., Tran-Cong-Miyata Q., editors., Nonlinear Dynamics in Polymeric Systems, American Chemical Society; Washington, DC. 869 (2003) 250–261. doi:10.1016/j.heliyon.2021.e07614.

[11] D. Bonn, H. Kellay, M. Ben Amar, J. Meunier, Viscous finger widening with surfactants and polymers, Phys. Rev. Lett. 75 (1995) 2132–2135. doi:10.1103/PhysRevLett.75.2132.

[12] N. Kagei, D. Kanie, M. Kawaguchi, Viscous fingering in shear thickening silica suspensions, Phys. Fluids 17 (5) (2005) 054103. doi:10.1063/1.1894407.

[13] D. Ozturk, M. L. Morgan, B. Sandnes, Flow-to-fracture transition and pattern formation in a discontinuous shear thickening fluid, Communications Physics 3 (1) (2020) 1–9. doi:10.1038/s42005-020-0382-7.

[14] Palak, R. Sathyanath, S. K. Kalpathy, R. Bandyopadhyay, Emergent patterns and stable interfaces during radial displacement of a viscoelastic fluid, Colloids Surf. A Physicochem. Eng. Asp. 629 (2021) 127405. doi:https://doi.org/10.1016/j.colsurfa.2021.127405.

[15] B. Sandnes, E. Flekkøy, H. Knudsen, K. Måløy, H. See, Patterns and flow in frictional fluid dynamics, Nature communications 2 (1) (2011) 1–8. doi:10.1038/ncomms1289.

[16] A. Fall, F. Bertrand, G. Ovarlez, D. Bonn, Shear thickening of cornstarch suspensions, Journal of Rheology 56 (3) (2012) 575–591. doi:10.1122/1.3696875.

[17] Y. Nagatsu, K. Matsuda, Y. Kato, Y. Tada, Experimental study on miscible viscous fingering involving viscosity changes induced by variations in chemical species concentrations due to chemical reactions, J. Fluid Mech. 571 (2007) 475–493. doi:10.1017/S0022112006003636.

[18] H. Shokri, M. H. Kayhani, M. Norouzi, Nonlinear simulation and linear stability analysis of viscous fingering instability of viscoelastic liquids, Physics of Fluids 29 (3) (2017) 033101. doi:10.1063/1.4977443.

[19] R. Buscall, Letter to the editor: Wall slip in dispersion rheometry, Journal of Rheology 54 (6) 1177–1183. doi:10.1122/1.3495981.

[20] R. Bandyopadhyay, P. H. Mohan, Y. M. Joshi, Stress relaxation in aging soft colloidal glasses, Soft Matter 6 (2010) 1462–1466. doi:10.1039/B916342E.

[21] P. Bourrianne, V. Niggel, G. Polly, T. Divoux, G. H. McKinley, Tuning the shear thickening of suspensions through surface roughness and physicochemical interactions, Phys. Rev. Research 4 (2022) 033062. doi:10.1103/PhysRevResearch.4.033062.

[22] T. S. Majmudar, R. P. Behringer, Contact force measurements and stress-induced anisotropy in granular materials, Nature 435 (7045) (2005) 1079–1082. doi:10.1038/nature03805.

[23] V. Rathee, J. Miller, D. L. Blair, J. S. Urbach, Structure of propagating high-stress fronts in a shear-thickening suspension, Proceedings of the National Academy of Sciences 119 (32) (2022) e2203795119. doi:10.1073/pnas.2203795119.

[24] V. Rathee, D. L. Blair, J. S. Urbach, Localized stress fluctuations drive shear thickening in dense suspensions, Proceedings of the National Academy of Sciences 114 (33) (2017) 8740–8745. doi:10.1073/pnas.1703871114.

[25] R. Maharjan, E. O'Reilly, T. Postiglione, N. Klimenko, E. Brown, Relation between dilation and stress fluctuations in discontinuous shear thickening suspensions, Phys. Rev. E 103 (2021) 012603. doi:10.1103/PhysRevE.103.012603.

[26] M. Nabizadeh, A. Singh, S. Jamali, Structure and dynamics of force clusters and networks in shear thickening suspensions, Phys. Rev. Lett. 129 (2022) 068001. doi:10.1103/PhysRevLett.129.068001.

[27] P. G. Saffman, G. I. Taylor, The penetration of a fluid into a porous medium or Hele-Shaw cell containing a more viscous liquid, Proceedings of the Royal Society of London. Series A. Mathematical and Physical Sciences 245 (1242) (1958) 312–329. doi:10.1098/rspa.1958.0085.

[28] G. M. Homsy, Viscous fingering in porous media, Annual Review of Fluid Mechanics 19 (1) (1987) 271–311. doi:10.1146/annurev.fl.19.010187.001415.

[29] A. Pinilla, M. Asuaje, N. Ratkovich, Experimental and computational advances on the study of Viscous Fingering: An umbrella review, Heliyon 7 (7) (2021) e07614. doi:https://doi.org/10.1016/j.heliyon.2021.e07614.

[30] Palak, V. R. S. Parmar, D. Saha, R. Bandyopadhyay, Pattern selection in radial displacements of a confined aging viscoelastic fluid, JCIS Open 6 (2022) 100047. doi:https://doi.org/10.1016/j.jciso.2022.100047.

[31] A. Lindner, D. Bonn, J. Meunier, Viscous fingering in a shear-thinning fluid, Physics of Fluids 12 (2) (2000) 256–261. doi:10.1063/1.870303.

[32] Q. Zhang, R. Zhang, B. Ge, Z. Yaqoob, P. T. C. So, I. Bischofberger, Structures and topological defects in pressure-driven lyotropic chromonic liquid crystals,

Proceedings of the National Academy of Sciences 118 (35) (2021) e2108361118. doi:10.1073/pnas.2108361118.

[33] V. Labiausse, R. Höhler, S. Cohen-Addad, Shear induced normal stress differences in aqueous foams, Journal of Rheology 51 (3) (2007) 479–492. doi:10.1122/1.2715392.

[34] H. Laun, Normal stresses in extremely shear thickening polymer dispersions, Journal of Non-Newtonian Fluid Mechanics 54 (1994) 87–108. doi:10.1039/C7SM00167C.

[35] D. Bensimon, L. Kadanoff, S. Liang, B. Shraiman, C. Tang, Viscous flows in two dimensions, Reviews of Modern Physics 58 (4) (1986) 977–999. doi:10.1103/REVMODPHYS.58.977.

[36] S. B. Gorell, G. M. Homsy, A theory of the optimal policy of oil recovery by secondary displacement processes, SIAM Journal on Applied Mathematics 43 (1) (1983) 79–98. doi:10.1137/0143007.

[37] B. Jha, L. Cueto-Felgueroso, R. Juanes, Fluid mixing from viscous fingering, Phys. Rev. Lett. 106 (2011) 194502. doi:10.1103/PhysRevLett.106.194502.

[38] M. R. Soltanian, M. A. Amooie, N. Gershenzon, Z. Dai, R. Ritzi, F. Xiong, D. Cole, J. Moortgat, Dissolution trapping of carbon dioxide in heterogeneous aquifers, Environmental Science & Technology 51 (13) (2017) 7732–7741. doi:10.1021/acs.est.7b01540.

[39] J. Marthelot, E. F. Strong, P. M. Reis, P. T. Brun, Designing soft materials with interfacial instabilities in liquid films, Nat. Comm. 9 (1) (2018) 4477. doi:10.1038/s41467-018-06984-7.

[40] W. Xu, J. Wang, F. Ding, X. Chen, E. Nasybulin, Y. Zhang, J.-G. Zhang, Lithium metal anodes for rechargeable batteries, Energy Environ. Sci. 7 (2014) 513–537. doi:10.1039/C3EE40795K.

[41] H. K. Foroushan, E. M. Ozbayoglu, S. Z. Miska, M. Yu, P. J. Gomes, On the Instability of the Cement/Fluid Interface and Fluid Mixing, SPE Drilling & Completion 33 (01) (2018) 63–76. doi:10.2118/180322-MS.

# Chapter 5

# Pattern selection in radial displacements of a confined aging viscoelastic fluid

## 5.1 Introduction

The morphology of an interfacial pattern formed during the displacement of one fluid by another depends on surface tension gradients [1, 2], viscoelasticities of the fluids [3–9],the driving pressures imposed during their injection [10], etc. The radial displacement of Bentonite clay suspensions by water resulted in viscoelastic fracturing when the stored elastic energy of the displaced suspension exceeded the energy required for fracture onset [6]. Given the vital roles that clay suspensions play in the formation of river networks [11] and drilling applications [12], a systematic study of their displacements is of paramount importance. Laponite® clay particles are disk-shaped with diameters 25-30 nm and thickness $\approx$ 1 nm. As discussed in the section 1.6 of chapter 1, Laponite particles acquire negative charge on their faces and positive charge on their rims when dispersed in water. This results in a time-dependent inter-particle electrostatic potential, such that the heterogeneously charged Laponite particles gradually self-assemble to form fragile microstructures composed of over-

lapping coins and house of cards (HoC) aggregates [13]. The percolation of these microstructures throughout the sample contributes to a spontaneous temporal increase in sample rigidity in a phenomenon identified as physical aging [14]. Further details about the aging dynamics of Laponite suspensions are discussed in the section 1.6 of chapter 1.

Rheological measurements such as in Fig. 5.1(a) can be employed to monitor the spontaneous evolution of the mechanical moduli of an aging viscoelastic clay suspension with aging time $t_w$; here $t_w$ is the time duration between sample loading and measurement. Additional details about rheological measurements are provided in section 5.2. We see from the photographs in the insets of Fig. 5.1(a) that while a clay suspension at an early age shows liquid-like rheology (top-left inset), the same suspension, when aged considerably, behaves like a solid and supports its own weight

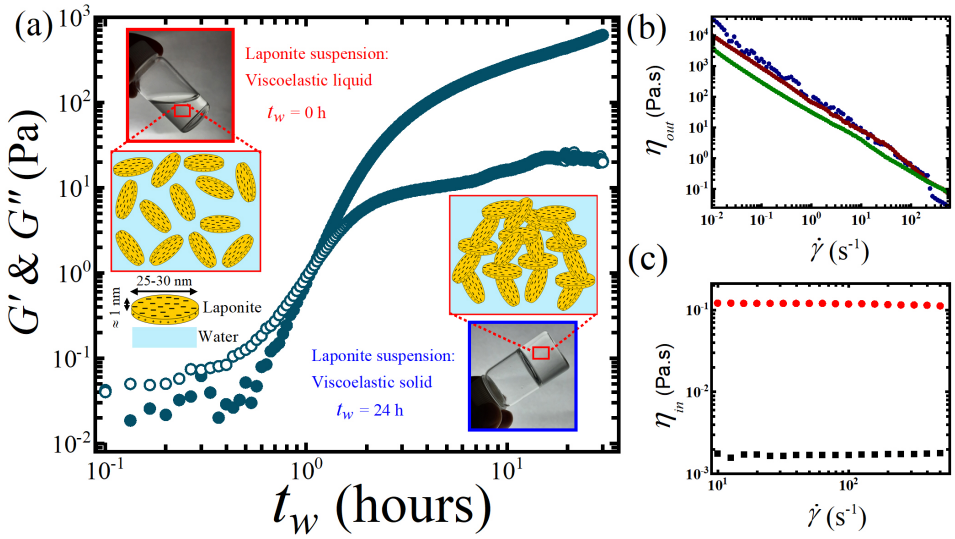



**Fig. 5.1:** **(a)** Evolution of elastic modulus $G'$ (●) and viscous modulus $G''$ (○) for a 3.25% w/v Laponite suspension with increasing aging time $t_w$. The inset on the top-left shows a photograph of a freshly prepared aqueous clay suspension in a glass vial and a schematic illustration of well dispersed Laponite clay particles. The inset on the bottom-right shows a photograph of the same sample, acquired after $t_w = 24$ h, and a schematic representation of the house of cards (HoC) suspension microstructures formed by self-assembly of Laponite clay particles. **(b)** Viscosity *vs.* shear rate ($\dot{\gamma}$) flow curves for 3.25% w/v Laponite suspensions at aging times $t_w = 1$ h (●), 5 h (●) and 24 h (●) show shear-thinning rheology. **(c)** Viscosity *vs.* shear rate ($\dot{\gamma}$) curves for water (■) and mineral oil (●) display Newtonian flow.

against gravity (bottom-right inset). Schematic illustrations of the arrangement of Laponite particles in the aqueous suspension medium are also displayed. While the platelets are well-dispersed in the medium at low suspension ages (top-left inset), the clay particles self-assemble to form fragile percolating microstructures at higher ages (bottom-right inset). Investigations into the phase behavior of Laponite suspensions have reported phase separation below a concentration of 1 % w/v [15], structural buildup and aging, presumably through Laponite house of cards (HoC) associations, between 1 % w/v and 2 % w/v [16, 17] and formation of a colloidal glassy phase above 2 % w/v [18].

We identify and analyze a wide range of interfacial patterns obtained by the displacement of an aging viscoelastic Laponite clay suspension by a Newtonian fluid in a radial Hele-Shaw cell. We study both miscible and immiscible displacements by using water and mineral oil as the displacing Newtonian fluids. As seen in Fig. 5.1(b), Laponite suspensions are strongly shear-thinning. In contrast, as shown in Fig. 5.1(c), water and mineral oil show Newtonian flow and their viscosities are independent of the imposed shear rates. We report three distinct interfacial pattern morphologies: dense viscous patterns (DVP), dendritic patterns (DP) and viscoelastic fractures (VEF) when aqueous clay suspensions of increasing $t_w$, and therefore having progressively larger elasticities, are displaced by water, a miscible solvent. In contrast, flower patterns (FP) transform to irregularly-shaped jagged patterns (JP) when an aqueous clay suspension of increasing $t_w$ is displaced by immiscible mineral oil. We note that the observed pattern morphologies are determined by the spontaneous aging and shear-thinning rheology of the displaced clay suspension, and the interfacial tension between the fluid pair. We quantify all the observed interfacial patterns by computing their average branch frequencies and average branch widths. Finally, we propose a new parameter, an areal ratio $A_p/A$, which we define as the area of the fully developed interfacial pattern, $A_p$, divided by the area of the smallest circle enclosing it, $A$. Estimation of $\ln(A_p/A)$ allows us to segregate all the distinct morphologies in a three-dimensional nonequilibrium phase diagram spanned by the

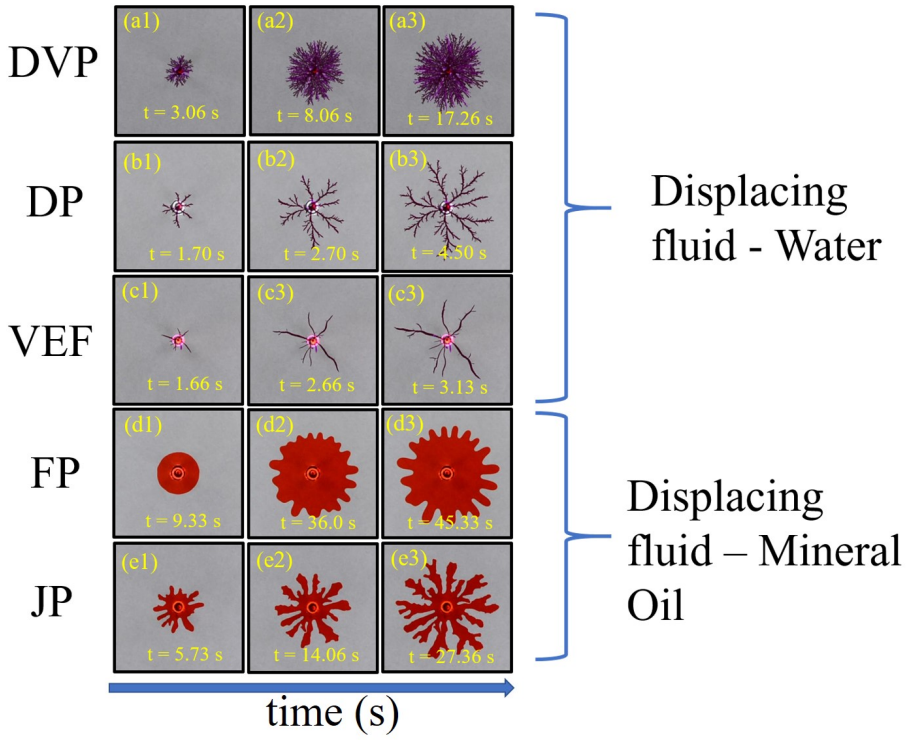



**Fig. 5.2:** Raw RGB images illustrating distinct morphologies of interfacial patterns obtained during the miscible and immiscible displacements of aging Laponite® suspensions at constant flow rate $q = 5$ ml/min. (a1-a3) Temporal evolution of dense viscous pattern (DVP) at $t_w = 1$ h for an interfacial tension $\sigma = 0$. (b1-b3) Temporal evolution of dendritic pattern (DP) for $t_w = 3$ h and $\sigma = 0$. (c1-c3) Temporal evolution of viscoelastic fracture (VEF) at $t_w = 24$ h and $\sigma = 0$. (d1-d3) Temporal evolution of flower pattern (FP) at $t_w = 1$ h and $\sigma \neq 0$. (e1-e3) Temporal evolution of jagged pattern (JP) at $t_w = 24$ h and $\sigma \neq 0$.

aging time ($t_w$) of the displaced clay suspension, the flow rate ($q$) of the displacing Newtonian fluid and the interfacial tension ($\sigma$).

## 5.2 Materials and Methods

The freshly prepared Laponite clay suspension (section 2.2.2 of chapter 2) was first loaded in a radial Hele-Shaw cell (section 2.3.2 in chapter 2) at a gap of 170 $\mu m$, with a syringe pump (NE-8000, New Era Pump Systems, USA) through a 3 mm central hole drilled on the top plate (Fig. 2.6). The aging time $t_w = 0$ corresponds to the time when the loading of the clay suspension was completed. Milli-Q water

and mineral oil (Acros Organics) were used as the miscible and immiscible displacing fluids respectively in two different sets of experiments. These Newtonian fluids were injected with flow rate $q$ through the same central hole of the Hele-Shaw cell after allowing the clay suspension to age to a pre-determined aging time $t_w$. The displacement an aging clay suspension by a Newtonian fluid resulted in interfacial patterns whose evolutions were recorded. Raw images of representative interfacial patterns are shown in Fig. 5.2. The stack of images obtained from the videos was converted to grayscale format (Fig. 4.1(b)) and analyzed using the MATLAB@2018 image processing toolbox. The procedure for binarization of raw images is provided in Fig. 5.3. The sample preparation protocol for the rheological measurements was identical to that for the Hele-Shaw experiments. A stress controlled Anton Paar MCR 501 rheometer was used for all rheology measurements reported here. For these measurements, the sample temperature was maintained at room temperature (25°C) using a Peltier temperature control device (C/PPTD 180/MD). We loaded the freshly prepared Laponite suspension in the concentric cylinder geometry and shear melted it at a high shear rate of 500 $s^{-1}$ to remove any memory of the sample loading process. The time at which shear application was stopped and the sample was allowed to evolve spontaneously in the rheological experiments was noted as aging time $t_w = 0$. The elastic and viscous moduli ($G'$ and $G''$) of Laponite suspensions as a function of $t_w$ were recorded at an applied strain amplitude 0.5 % and angular frequency 1 rad/s. A cone and plate geometry was used to measure flow curves of shear-thinning Laponite suspensions. All the experiments were performed at room temperature (25°C).

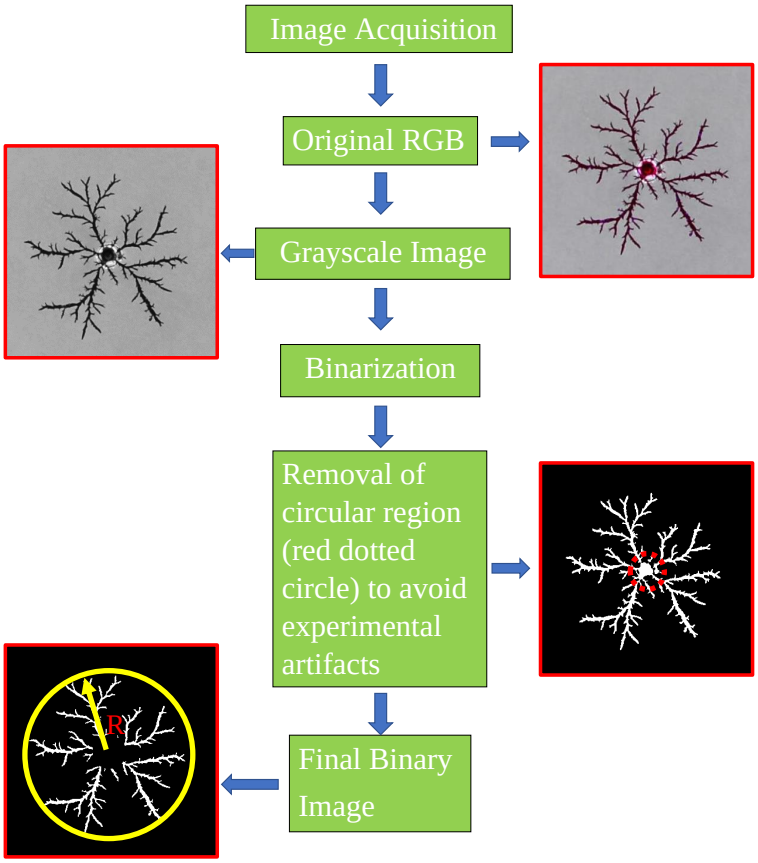



**Fig. 5.3:** Flow chart illustrating the binarization of RGB images. $R$ is the longest finger length of the pattern such that a circle of radius $R$ encloses the entire pattern.

## 5.3 Results and Discussion

### 5.3.1 Aging time of the displaced suspension determines interfacial pattern morphology

Figures 5.4(a1-g1, a2-g2) show representative interfacial patterns formed during the radial displacement of an aqueous clay suspension of increasing ages, $t_w$, by miscible and immiscible Newtonian displacing fluids at a constant flow rate $q = 5$ ml/min. All the interfacial patterns correspond to a fixed longest finger length $R = 7.01 \pm 0.01$ cm ($R$ is defined in Fig. 5.3). We note three distinct morphologies for miscible displacements by water (interfacial tension $\sigma = 0$) as the elasticity of the displaced

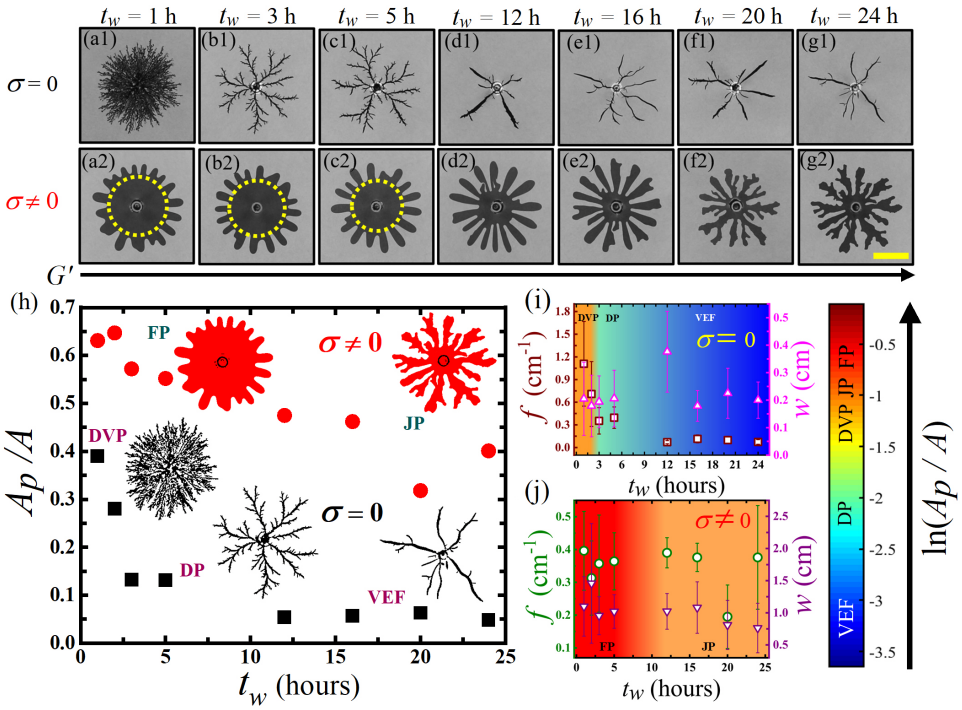



**Fig. 5.4:** Miscible (interfacial tension $\sigma = 0$) displacement patterns in grayscale obtained by the displacement of a 3.25% w/v aqueous clay suspension by water at constant flow rate $q = 5$ ml/min and for different suspension aging times $t_w$: **(a1)** dense viscous patterns (DVP), **(b1-c1)** dendritic patterns (DP) and **(d1-g1)** viscoelastic fractures (VEF). Immiscible ($\sigma \neq 0$ ) displacement patterns obtained by the displacement of an aging clay suspension at the same $t_w$ values and $q = 5$ ml/min: **(a2-c2)** flower patterns (FP). Yellow dotted circles illustrate the central dark stable region. **(d2-g2)** jagged patterns (JP). All the patterns correspond to a fixed longest finger length $R = 7.01 \pm 0.01$ cm. The scale bar is 4 cm. **(h)** The areal ratio $A_p/A$ of the patterns vs. $t_w$ for miscible (■) and immiscible (●) displacements. Here, $A_p$ is the area of the fully developed pattern and $A = \pi R^2$ is the area of the smallest circle enclosing the entire pattern. **(i)** Average branch frequency ($f$, □) and average width ($w$, △) of the fingers as a function of $t_w$ for miscible ($\sigma = 0$) displacement patterns. **(j)** $f$ (○) and $w$ (▽) vs. $t_w$ for immiscible ($\sigma \neq 0$) displacement patterns. Error bars in $f$ and $w$ represent the standard deviations in measurements of multiple branches. The vertical colorbar on the right maps the distinct morphological patterns to the natural logarithms of their areal ratios: $\ln(A_p/A)$.

clay suspension increases due to aging (Figs. 5.4(a1-g1)). For a clay suspension of low age ($t_w = 1$ h), we observe the frequent merging of neighboring fingers during pattern evolution, resulting in a pattern without well-defined boundaries (Fig. 5.4(a1)). We designate this pattern, characterized by narrow fingers and side branches, as a dense viscous pattern (DVP). At intermediate $t_w$, we observe dendritic patterns (DP, shown in Figs. 5.4(b1,c1)) with considerable side-branching and well-defined

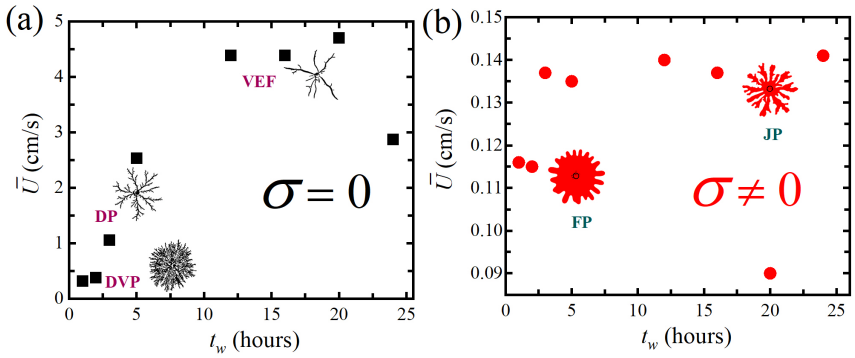



**Fig. 5.5:** The time-averaged finger-tip velocities vs. aging time $t_w$ for **(a)** miscible (●) and **(b)** immiscible (●) displacements of Laponite suspensions by Newtonian fluids (water and oil respectively) at constant flow rate $q = 5$ ml/min. DVP, DP, VEF, FP and JP refer to the experimentally observed dense viscous patterns, dendritic patterns, viscoelastic fractures, flower patterns and jagged patterns, respectively.

interfacial boundaries. For highly aged suspensions characterized by large $t_w$ values, viscoelastic fractures (VEF) emerge (Figs. 5.4(d1-g1)) and propagate rapidly. The VEF patterns display sharp finger-tips and perpendicular offshoots from the primary cracks, and are morphologically very dissimilar to DVP and DP. The observed side-branching in DVP and DP occurs due to flow-induced anisotropies [19] arising from shear-thinning of the increasingly elastic displaced clay suspension.

Interestingly, nonlinear simulations [3] revealed that a competition between enhanced finger-tip velocity due to shear-thinning of a displaced viscoelastic fluid and simultaneous finger-tip broadening due to imposed driving pressures can result in the formation of side branches. Here, we estimate the finger-tip velocity of each pattern by recording the evolution of the longest finger of length $R$ with time. With the transition of the patterns from DVP to VEF, the time-averaged values of finger-tip velocities ($\bar{U}$, Fig. 5.5) increase. These velocity values are used to calculate the shear rates ($\dot{\gamma} = 2\bar{U}/b$ where $b$ is the Hele-Shaw cell gap [20]) imposed by the displacing fluid. The estimated values of shear rates at the finger-tips ($36.47\ \text{s}^{-1} \leq \dot{\gamma} \leq 552.94\ \text{s}^{-1}$) increase due to enhanced shear-thinning of the displaced clay suspension as its age, $t_w$, increases. This leads to the increased shedding of side branches. However, for clay suspensions having large $t_w$, elastic effects dom-

inate over shear-thinning, resulting in the emergence of VEF patterns. Viscoelastic fractures were reported in earlier experiments involving miscible displacements of elastic Bentonite clay suspensions [6]. Such patterns were also seen when elastic agar gel suspensions [21] and shear-jammed cornstarch suspensions [7] were displaced by immiscible air under large driving pressures. In our experiments with the highly aged clay suspension, the system-wide percolation of suspension microstructures causes the buildup of elastic stresses. Local yielding events in the jammed clay suspension during its displacement by water lead to the rapid release of elastic stresses and the observed emergence of viscoelastic fractures (VEF).

Since the formation of sharp tips costs more energy when the interfacial tension is non-zero, immiscible displacement patterns preferentially preserve smooth and rounded finger-tips. The stabilizing effect of interfacial tension results in considerably lower finger-tip velocities $\bar{U}$ (Fig. 5.5(b)) and shear rates ($12.94\ s^{-1} \leq \dot{\gamma} \leq 16.47\ s^{-1}$) than in miscible displacement experiments (Fig. 5.5(a)). Furthermore, for immiscible displacements, $\bar{U}$ does not show a significant dependence on the age of the displaced clay suspension. We note that immiscible displacement patterns (Figs. 5.4(a2-g2)) have very distinct morphologies when compared to their miscible counterparts at identical suspension ages and displacing fluid flow rates. Flower patterns (FP) with round finger-tips and a dark central region (yellow dotted circles in Figs. 5.4(a2-c2)) are observed when suspensions of low to intermediate ages are displaced by mineral oil. This dark central region results from a delay in onset of instability at non-zero interfacial tension and resembles the observations in previous experiments involving Newtonian fluid pairs [2, 22]. Displacement of a highly aged clay suspension having large $t_w$ requires disruption of the fragile suspension microstructures by a process that costs substantial energy and leads to a transition to more ramified jagged patterns (JP, shown in Figs. 5.4(d2-g2)). It is to be noted that the observed jagged patterns closely resemble those seen during the immiscible displacement of shaving foam, a non-zero yield stress material, by air [4].

We quantify the morphologies of the interfacial patterns (Figs. 5.4(a1-g1, a2-g2))

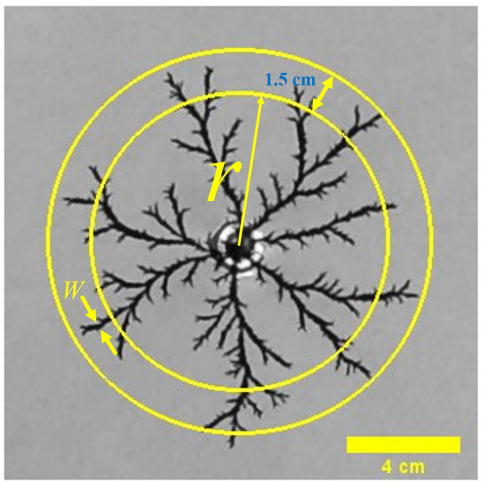



**Fig. 5.6:** A representative interfacial pattern showing the annular region of width 1.5 cm, used in the calculations of average branch frequencies ($f$) and branch widths ($w$). The average branch frequency, $f$, is estimated as $f = \frac{1}{m}\sum_{j=1}^{m}\frac{N_j}{2\pi r_j}$ over $m = 32$ circles within the annular region. Here, $N_j$ is the number of branches intersecting a circle of radius $r_j$, such that 5.2 cm $\leq r_j \leq$ 6.7 cm. The average branch width, $w$, of an interfacial patterns is estimated as $w = \frac{1}{m}\sum_{j=1}^{m} < W >_{r_j}$ where $< W >_{r_j}$ denotes the average width of the branches intersecting a circle of radius $r_j$ in the same annular region of interest.

by estimating their areal ratios ($A_p/A$), average branch frequencies ($f$) and average branch widths ($w$). Figure 5.4(h) shows the areal ratios, defined as the area of the fully developed pattern ($A_p$) normalized by the area of the smallest circle enclosing it ($A = \pi R^2$, Fig. 5.3, bottom left figure), as a function of aging time $t_w$. As a result of the wide branching morphologies of the immiscible patterns (Figs. 5.4(a2-g2)), we note that their areal ratios $A_p/A$ are always greater than for the miscible ones at the same suspension age. The measurements of average branch frequencies are performed by analyzing a narrow annular region close to the outermost boundary of the fully developed interfacial patterns, as displayed in Fig. 5.6. The average branch frequency is defined as $f = < N/2\pi r >_r$, where $N$ is the number of branches intersecting a circle of radius $r$ and $<>_r$ denotes the average over circles of different radii in the annulus of interest. As seen in Fig. 5.4(i), viscoelastic fractures (VEF) display smaller branch frequencies when compared to dendritic patterns (DP) and dense viscous patterns (DVP). The average finger width is also estimated from measurements within the same annulus. We note that the thick, uniform fingers

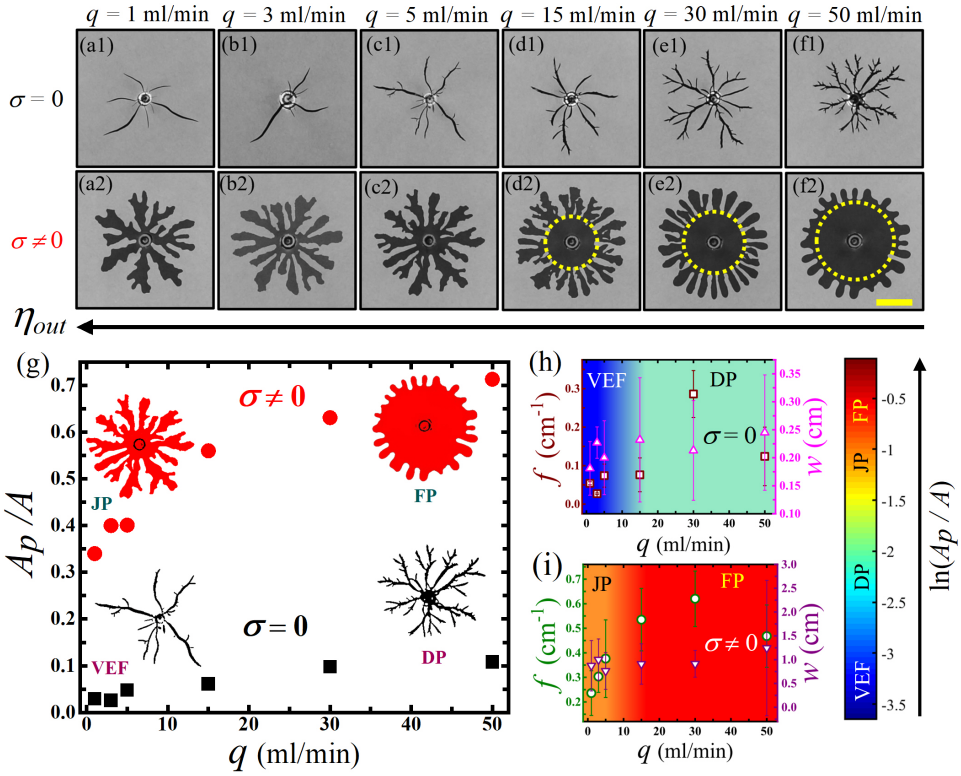



**Fig. 5.7:** Miscible displacement patterns in grayscale, obtained by the displacement of a 3.25% w/v aqueous clay suspension of $t_w = 24$ h by water at various flow rates $q$: **(a1-c1)** viscoelastic fractures (VEF) and **(d1-f1)** dendritic patterns (DP). Immiscible displacement patterns at the same flow rates as in (a1-f1): **(a2-c2)** jagged patterns (JP) and **(d2-f2)** flower patterns (FP). All the patterns have a fixed longest finger length $R = 7.01 \pm 0.01$ cm. The scale bar is 4 cm. **(g)** $A_p/A$ as a function of flow rates for miscible (■) and immiscible (●) displacements. **(h)** Average branch frequency ($f$, □) and average width ($w$, △) of the fingers as a function of $q$ for miscible ($\sigma = 0$) displacement patterns. **(i)** $f$ (○) and $w$ (▽) vs. $q$ for immiscible ($\sigma \neq 0$) displacement patterns. The distinct morphological regimes are mapped on a colorbar using the natural logarithms of their areal ratios: $\ln(A_p/A)$.

that form in immiscible displacement experiments (Fig. 5.4(j)) point to the critical role that surface tension plays in stabilizing flow instabilities. We conclude that the interfacial tension between the fluid pair and the aging time of the displaced suspension are reliable control parameters in determining elasticity-induced changes in the morphological features of miscible and immiscible displacement patterns.

### 5.3.2 Pattern morphology can be tuned by controlling the shear-thinning rheology of the displaced suspension

The viscous modulus of a 3.25% w/v aqueous clay suspension plateaus at $t_w \approx 24$ h, while its elastic modulus continues to evolve (Fig. 5.1(a)). We next explore the radial displacement of a sufficiently elastic suspension of age $t_w = 24$ h in the Hele-Shaw cell due to the injection of Newtonian displacing fluids at different flow rates $q$. Viscoelastic fractures (VEF) with perpendicular offshoots are observed when water displaces the elastic clay suspension at low flow rates (Figs. 5.7(a1-c1)). The low driving pressures cause minimal shear-thinning of the displaced clay suspension such that fractures propagate rapidly due to the release of elastic stresses. On increasing the flow rate, VEF are replaced by more ramified dendritic patterns (DP) with pointed tips that display multiple splitting events during their growth (Figs. 5.7(d1-f1)). The average finger-tip velocities ($\bar{U}$) increase with increasing flow rates of the displacing fluid (Fig. 5.8(a)). The shear rates ($158.82\ \text{s}^{-1} \leq \dot{\gamma} \leq 1907.05\ \text{s}^{-1}$) imposed at the finger-tip by the displacing fluid, estimated using $2\bar{U}/b$ [20] as discussed earlier, therefore also increase with increasing flow rates, resulting in considerable shear-thinning of the displaced clay suspension. At high flow rates of the displacing fluid, the fragile microstructures formed by the self-assembling Laponite particles rupture irreversibly. This reduces suspension elasticity and results in the observed change in interfacial pattern morphology from VEF to DP.

The immiscible displacement of a clay suspension with mineral oil leads to a transition from jagged patterns (JP) to flower patterns (FP) as the flow rate of the displacing mineral oil is increased (Figs. 5.7(a2-f2)). The finger-tip velocities ($\bar{U}$) and the corresponding shear rates ($4.70\ \text{s}^{-1} \leq \dot{\gamma} \leq 82.35\ \text{s}^{-1}$) imposed by the mineral oil increase with increasing flow rate but are always less than those noted in miscible displacement experiments (Figs. 5.8(a,b)). In order to understand the observed flow stabilization against viscous fingering instabilities at increasing flow rates, we estimate the viscosity ratios of the fluid pair $\eta_{in}/\eta_{out}$, where $\eta_{in}$ is the

viscosity of the displacing Newtonian fluid and $\eta_{out}$ is the shear-dependent viscosity of the displaced clay suspension at different flow rates $q$. The shear-thinning of the displaced clay suspension at high shear rates leads to an increase in the viscosity ratio of the fluid pair (Fig. 5.8(c)). This reduces the destabilizing action of viscous forces and results in increasingly stable interfaces at high injection flow rates. Such suppression of viscous instabilities has been noted in previous work involving Newtonian-Newtonian [23, 24] and Newtonian-non-Newtonian displacements [5]. Since mineral oil is more viscous than water (Figs. 5.1(c)), the increase in viscosity ratio with increasing $q$ is more pronounced in immiscible displacements when compared to the miscible cases. This causes the observed flow stabilization and the transition from JP to FP when $q$ is increased (Figs. 5.7(a2-f2)). At the highest viscosity ratio (Fig. 5.8(c)), we observe a stable pattern (SP, Fig. 5.9(b)) with a circularly growing interface at all times during the immiscible displacement of a clay suspension of low age ($t_w$ = 1 h) at a high flow rate ($q$ = 50 ml/min). We conclude from the data presented in Fig. 5.7 that shear-thinning effects dominate as the injection flow rate is increased, and the flow stabilizes due to two factors, *viz.*, an increase in the viscosity ratio of the fluid pair and the presence of a non-zero interfacial tension. Pattern morphologies at a radial quasi-two-dimensional interface

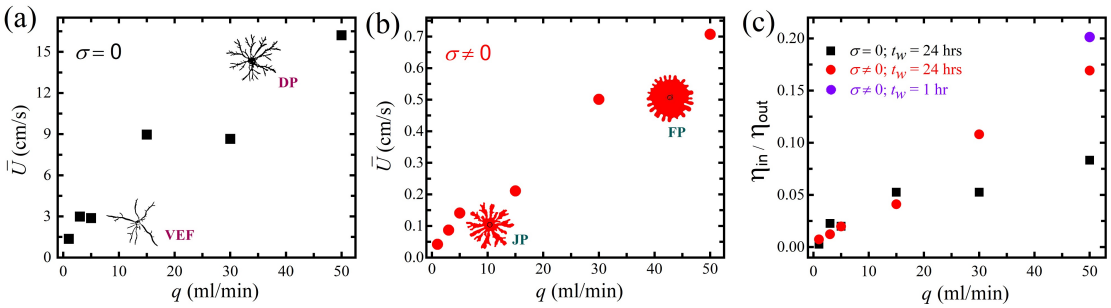



**Fig. 5.8:** The time-averaged finger-tip velocities $\bar{U}$ vs. $q$ for **(a)** miscible (●) and **(b)** immiscible (●) displacements of Laponite suspensions at age $t_w$ = 24 hrs. **(c)** Viscosity ratios $\eta_{in}/\eta_{out}$ vs. $q$, where $\eta_{in}$ is the viscosity of the displacing Newtonian fluids and $\eta_{out}$ is the shear-dependent viscosity of the displaced Laponite suspension. The viscosity ratio corresponding to a stable pattern observed during displacement of a Laponite suspension of $t_w$ = 1 h by mineral oil at $q$ = 50 ml/min (●) is also included.

can therefore also be effectively tuned by controlling the flow rate of the displacing fluid.

We next quantify the morphologies of the observed interfacial patterns in terms of their areal ratios ($A_p/A$), average branch frequencies ($f$) and average branch widths ($w$). As in our earlier experiments in which we displaced a clay suspension at predetermined aging times, $t_w$ (Fig. 5.4(h)), $A_p/A$ is larger for immiscible displacement patterns when compared to the miscible ones at a fixed flow rate of the displacing fluid (Fig. 5.7(g)). Dendritic patterns (DP) obtained at high $q$ during miscible displacements display larger branch frequencies when compared to viscoelastic frac-

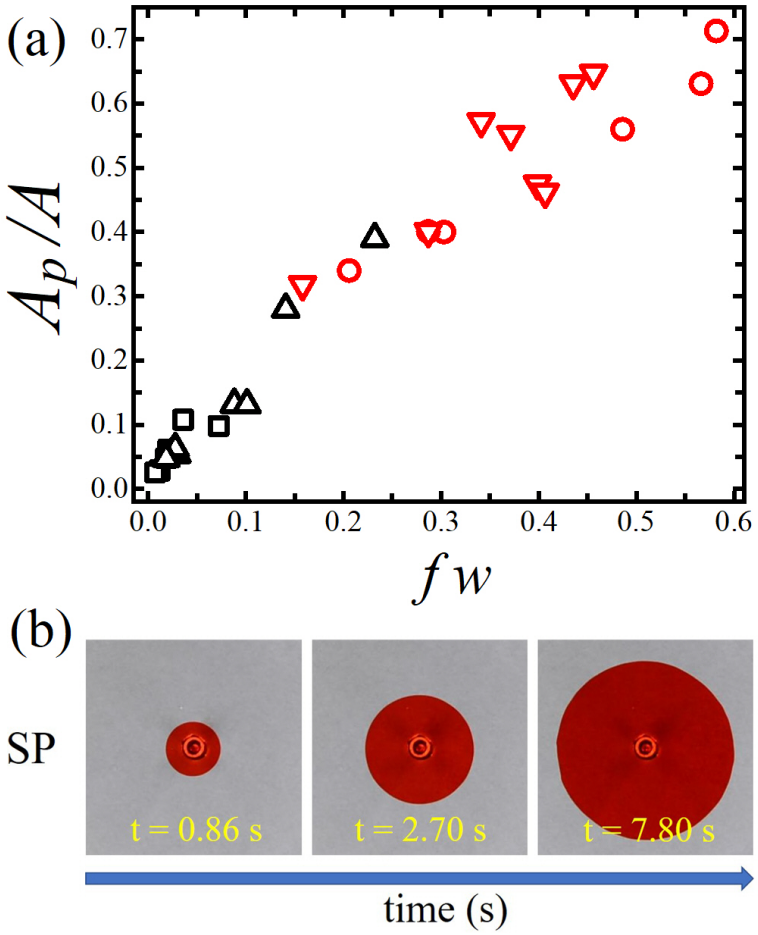



**Fig. 5.9:** **(a)** $A_p/A$ vs. $fw$ for miscible (△ for variable $t_w$, □ for variable $q$ ) and immiscible (▽ for variable $t_w$, ○ for variable $q$) displacements. **(b)** Temporal evolution of stable patterns (SP) at $t_w = 1$ h, $q = 50$ ml/min and $\sigma \neq 0$ in RGB format.

tures (VEF). The presence of non-zero interfacial tension results in larger average branch widths $w$ in the immiscible displacement patterns (Fig. 5.7(i)) when compared to their miscible counterparts (Fig. 5.7(h)). The interfacial patterns obtained at different ages $t_w$ of the displaced clay suspensions (displayed in Figs. 5.4(a1-g1,a2-g2)) can therefore be recovered by keeping $t_w$ fixed while appropriately changing the flow rates $q$ of the displacing fluids (Figs. 5.7(a1-f2,a2-f2)). Interestingly therefore, displacing a clay suspension of increasing age at a fixed flow rate generates the same sequence of patterns as seen during the displacement of the suspension at a fixed age while lowering the flow rates of the displacing fluid.

Regardless of whether the interfacial patterns were generated while changing the flow rate of the displacing fluid or the aging time of the displaced clay suspension, we see from Fig. 5.9(a) that their areal ratios ($A_p/A$) are linearly correlated with the products of their average branch frequencies ($f$) and widths ($w$). As noted earlier, we observe a stable pattern (SP) during the immiscible displacement of a clay suspension of low age ($t_w = 1$ h) at a high flow rate ($q = 50$ ml/min, Fig. 5.8(c) and Fig. 5.9(b)). Since it is not feasible to estimate the branch frequency and finger width of a stable pattern, we compute the natural logarithms of the areal ratios, $\ln(A_p/A)$, of all the patterns and segregate them in a three-dimensional nonequilibrium phase diagram (Fig. 5.10) spanned by the aging time ($t_w$) of the displaced clay suspension, the flow rate ($q$) of the displacing fluid and the interfacial tension ($\sigma$). All the interfacial patterns obtained in our experiments are represented on the phase diagram in Fig. 5.10 by symbols of distinct colors that are mapped to their respective $\ln(A_p/A)$ values, as defined in the colorbar. We therefore identify the natural logarithm of areal ratio $\ln(A_p/A)$, as a single parameter that can be employed to effectively distinguish the wide range of quasi-two-dimensional interfacial patterns formed in our Newtonian-non-Newtonian displacement experiments.

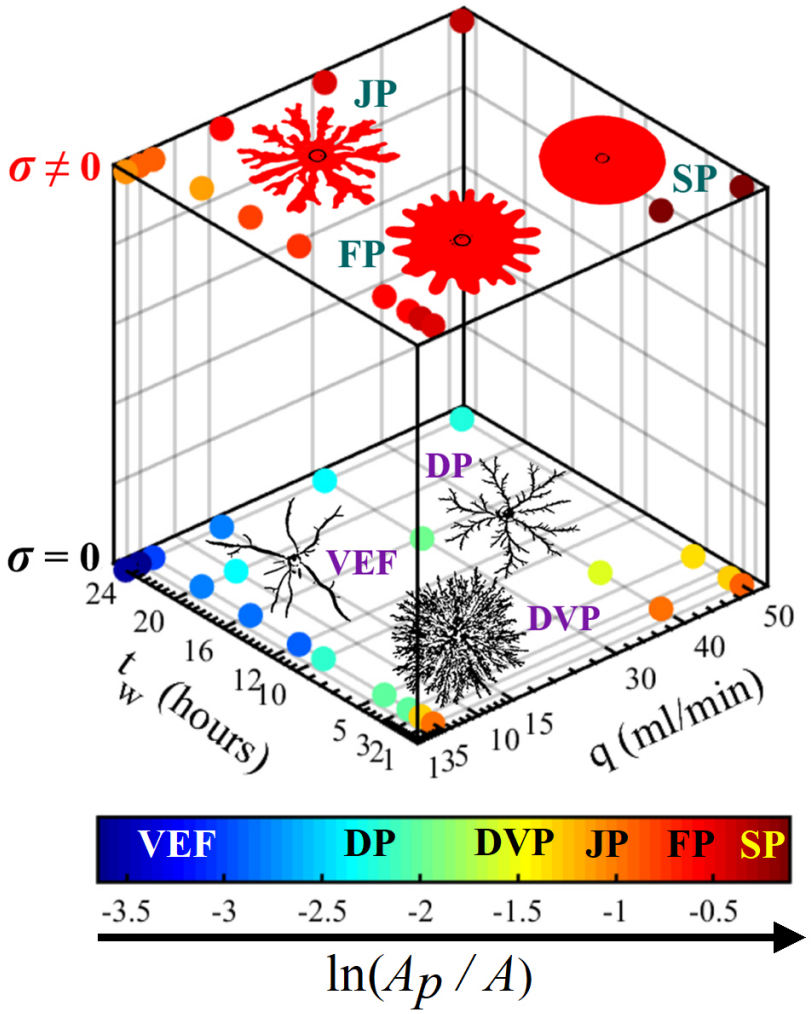



**Fig. 5.10:** Phase diagram relating the suspension aging time $t_w$, the displacing fluid flow rate $q$, and the interfacial tension $\sigma$: bottom plane shows miscible ($\sigma = 0$) displacements with three different pattern morphologies: dense viscous patterns (DVP), dendritic patterns (DP) and viscoelastic fractures (VEF). Top plane shows immiscible ($\sigma \neq 0$) displacement patterns with three different morphologies: flower patterns (FP), jagged patterns (JP) and stable patterns (SP). The colored solid circles represent all the distinct interfacial patterns observed experimentally. The colors of these circles, defined in the colorbar at the bottom, have one-to-one mapping with the natural logarithms of the pattern areal ratios: $\ln(A_p/A)$.

## 5.4 Conclusions

Since a colloidal clay suspension is viscoelastic and shows spontaneous aging, its time-dependent elastic modulus and shear-thinning rheology should lead to the generation of a wide range of patterns when it is displaced at different flow rates by

Newtonian fluids of contrasting miscibilities. In this chapter, we systematically study the selection of interfacial patterns by radially displacing an aging soft glassy aqueous clay suspension with miscible and immiscible Newtonian fluids in a confined geometry. We observe and analyze the wide variety of interfacial morphologies that are generated in these controlled experiments. We note that the observed patterns strongly depend on the elasticity of the displaced suspension, parameterized in terms of the suspension aging time, the injection flow rate of the displaced Newtonian fluid, and the miscibility of the fluid pair. For both miscible and immiscible displacements, we understand the transitions between the observed interfacial patterns by considering the competition between interfacial, elastic and viscous forces in the aging and shear-thinning clay suspension. We note that instabilities driven by viscous forces result in interfacial patterns characterized by tip-splitting, side branches, and thick protrusions resembling flower petals. In contrast, if elastic forces dominate due to the spontaneous formation of suspension microstructures [13, 14, 25], we observe viscoelastic fracturing or jagged interfaces. In both scenarios, the presence of a non-zero interfacial tension leads to enhanced flow stabilization. Our work supplements the existing experimental literature on clay suspension displacements [6, 26, 27] by identifying the suspension aging time $t_w$, which is closely correlated with suspension elasticity, as a new control parameter that reliably determines interfacial pattern morphologies. Besides extending our fundamental knowledge of viscoelastic flows in confined environments, the present study has important implications in understanding geophysical phenomena such as river delta formation [11], and in controlling the displacements of viscoelastic materials such as mud and cement slurries [28].

The control of instabilities at the interface between a pair of fluids is crucial in material transport. Interfacial instabilities are essential in designing and optimizing several processes such as filtration and flow in porous media [29]. However, they are undesirable in certain scenarios, such as in the formation of dendrites at the anode-electrolyte interface in rechargeable lithium batteries [30] and the emergence of viscous fingers at the water-oil interface in enhanced oil recovery [31]. Therefore,

systematic suppression or enhancement of the interfacial instabilities is important, and different strategies to control these instabilities were reported earlier [5, 32–35]. To the best of our knowledge, the research presented here is the first report of the sensitive dependence of the interfacial pattern morphology on the age of the displaced suspension. Our demonstration that the natural logarithms of the areal ratios can effectively distinguish pattern morphologies on a three-dimensional phase diagram can have far-reaching ramifications in controlling and predicting pattern morphologies between a fluid pair with well-characterized physicochemical properties.

Interparticle electrostatic interactions, and therefore the aging dynamics of a charged colloidal clay suspension, can be altered by varying clay concentration, temperature, and by incorporating dissociating additives such as salts and acids [36–38]. It would be of interest to systematically study the roles of diverse physicochemical conditions in the formation of interfacial patterns during the displacement of a clay suspension by miscible and immiscible Newtonian fluids. A possible extension of this study could involve the addition of non-dissociating molecules (kosmotropes such as glucose that enhance water structure [39], or chaotropes such as N,N-Dimethylformamide that disrupt hydrogen bonding in water [40]) to the aqueous medium during preparation of the clay suspension [41]. The presence of additives is expected to alter the aging dynamics and rheology of the suspension, which would strongly influence the interfacial pattern morphologies generated when the latter is displaced.

# References


[1] J.-D. Chen, Growth of radial viscous fingers in a Hele-Shaw cell, J. Fluid Mech. 201 (1989) 223–242. doi:10.1017/S0022112089000911.

[2] I. Bischofberger, R. Ramachandran, S. R. Nagel, An island of stability in a sea of fingers: emergent global features of the viscous-flow instability, Soft Matter 11 (2015) 7428–7432. doi:10.1039/C5SM00943J.

[3] L. Kondic, M. J. Shelley, P. Palffy-Muhoray, Non-Newtonian Hele-Shaw Flow and the Saffman-Taylor Instability, Phys. Rev. Lett. 80 (1998) 1433–1436. doi:10.1103/PhysRevLett.80.1433.

[4] S. S. Park, D. J. Durian, Viscous and elastic fingering instabilities in foam, Phys. Rev. Lett. 72 (1994) 3347–3350. doi:10.1103/PhysRevLett.72.3347.

[5] Palak, R. Sathyanath, S. K. Kalpathy, R. Bandyopadhyay, Emergent patterns and stable interfaces during radial displacement of a viscoelastic fluid, Colloids Surf. A Physicochem. Eng. Asp. 629 (2021) 127405. doi:https://doi.org/10.1016/j.colsurfa.2021.127405.

[6] E. Lemaire, P. Levitz, G. Daccord, H. Van Damme, From viscous fingering to viscoelastic fracturing in colloidal fluids, Phys. Rev. Lett. 67 (1991) 2009–2012. doi:10.1103/PhysRevLett.67.2009.

[7] D. Ozturk, M. L. Morgan, B. Sandnes, Flow-to-fracture transition and pattern formation in a discontinuous shear thickening fluid, Commun. Phys. 3 (1) (2020) 1–9. doi:10.1038/s42005-020-0382-7.

[8] T. V. Ball, N. J. Balmforth, A. P. Dufresne, Viscoplastic fingers and fractures in a Hele-Shaw cell, J. Non-Newton. Fluid Mech. 289 (2021) 104492. doi:https://doi.org/10.1016/j.jnnfm.2021.104492.

[9] K. Osei-Bonsu, N. Shokri, P. Grassia, Fundamental investigation of foam flow in a liquid-filled Hele-Shaw cell, J. Colloid Interface Sci. 462 (2016) 288–296. doi:https://doi.org/10.1016/j.jcis.2015.10.017.

[10] O. Praud, H. L. Swinney, Fractal dimension and unscreened angles measured for radial viscous fingering, Phys. Rev. E 72 (2005) 011406. doi:10.1103/PhysRevE.72.011406.

[11] S. Roy, S. Tarafdar, Patterns in the variable Hele-Shaw cell for different viscosity ratios: Similarity to river network geometry, Phys. Rev. E 54 (1996) 6495–6499. doi:10.1103/PhysRevE.54.6495.

[12] X.-B. Huang, J.-S. Sun, Y. Huang, B.-C. Yan, X.-D. Dong, F. Liu, R. Wang, Laponite: a promising nanomaterial to formulate high-performance water-based drilling fluids, Pet. Sci. 18 (2) (2021) 579–590. doi:10.1007/s12182-020-00516-z.

[13] M. Delhorme, B. Jönsson, C. Labbez, Monte Carlo simulations of a clay inspired model suspension: the role of rim charge, Soft Matter 8 (2012) 9691–9704. doi:10.1039/C2SM25731A.

[14] S. Ali, R. Bandyopadhyay, Effect of electrolytes on the microstructure and yielding of aqueous dispersions of colloidal clay, Soft Matter 12 (2016) 414–421. doi:10.1039/C5SM01700A.

[15] B. Ruzicka, E. Zaccarelli, A fresh look at the Laponite phase diagram, Soft Matter 7 (4) (2011) 1268–1286. doi:10.1039/C0SM00590H.

[16] S. Jabbari-Farouji, H. Tanaka, G. H. Wegdam, D. Bonn, Multiple nonergodic disordered states in Laponite suspensions: A phase diagram, Phys. Rev. E 78 (2008) 061405. doi:10.1103/PhysRevE.78.061405.

[17] T. Nicolai, S. Cocard, Dynamic Light-Scattering Study of Aggregating and Gelling Colloidal Disks, J. Colloid Interface Sci. 244 (1) (2001) 51–57. doi:10.1006/jcis.2001.7930.

[18] R. Angelini, E. Zaccarelli, F. A. de Melo Marques, M. Sztucki, A. Fluerasu, G. Ruocco, B. Ruzicka, Glass–glass transition during aging of a colloidal clay, Nat. Commun. 5 (1) (2014) 4049. doi:10.1038/ncomms5049.

[19] E. Ben-Jacob, R. Godbey, N. D. Goldenfeld, J. Koplik, H. Levine, T. Mueller, L. M. Sander, Experimental Demonstration of the Role of Anisotropy in Interfacial Pattern Formation, Phys. Rev. Lett. 55 (1985) 1315–1318. doi:10.1103/PhysRevLett.55.1315.

[20] Y. Nagatsu, K. Matsuda, Y. Kato, Y. Tada, Experimental study on miscible viscous fingering involving viscosity changes induced by variations in chemical species concentrations due to chemical reactions, J. Fluid Mech. 571 (2007) 475–493. doi:10.1017/S0022112006003636.

[21] T. Hirata, Fracturing due to fluid intrusion into viscoelastic materials, Phys. Rev. E 57 (1998) 1772–1779. doi:10.1103/PhysRevE.57.1772.

[22] L. Paterson, Radial fingering in a Hele Shaw cell, J. Fluid Mech. 113 (1981) 513–529. doi:10.1017/S0022112081003613.

[23] I. Bischofberger, R. Ramachandran, S. R. Nagel, Fingering versus stability in the limit of zero interfacial tension, Nat. Commun. 5 (1) (2014) 1–6. doi:10.1038/ncomms6265.

[24] E. Lajeunesse, J. Martin, N. Rakotomalala, D. Salin, 3D instability of miscible displacements in a Hele-Shaw cell, Phys. Rev. Lett. 79 (1997) 5254–5257. doi:10.1103/PhysRevLett.79.5254.

[25] R. Bandyopadhyay, D. Liang, H. Yardimci, D. A. Sessoms, M. A. Borthwick, S. G. J. Mochrie, J. L. Harden, R. L. Leheny, Evolution of Particle-Scale Dynamics in an Aging Clay Suspension, Phys. Rev. Lett. 93 (2004) 228302. doi:10.1103/PhysRevLett.93.228302.

[26] H. Van Damme, F. Obrecht, P. Levitz, L. Gatineau, C. Laroche, Fractal viscous fingering in clay slurries, Nature 320 (6064) (1986) 731–733. doi:10.1038/320731a0.

[27] H. V. Damme, E. Lemaire, From Flow to Fracture and Fragmentation in Colloidal Media, In: J.C. Charmet, S. Roux, E. Guyon (Eds.), Disorder and Fracture., Springer, Boston, MA, 1990, pp. 83–104. doi:10.1007/978-1-4615-6864-3_6.

[28] S. H. Bittleston, J. Ferguson, I. A. Frigaard, Mud removal and cement placement during primary cementing of an oil well – Laminar non-Newtonian displacements in an eccentric annular Hele-Shaw cell, J. Eng. Math. 43 (2) (2002) 229–253. doi:10.1023/A:1020370417367.

[29] L. Paterson, Diffusion-Limited Aggregation and Two-Fluid Displacements in Porous Media, Phys. Rev. Lett. 52 (1984) 1621–1624. doi:10.1103/PhysRevLett.52.1621.

[30] W. Xu, J. Wang, F. Ding, X. Chen, E. Nasybulin, Y. Zhang, J.-G. Zhang, Lithium metal anodes for rechargeable batteries, Energy Environ. Sci. 7 (2014) 513–537. doi:10.1039/C3EE40795K.

[31] S. B. Gorell, G. Homsy, A theory of the optimal policy of oil recovery by secondary displacement processes, SIAM J. Appl. Math. 43 (1) (1983) 79–98. doi:10.1137/0143007.

[32] T. Gao, M. Mirzadeh, P. Bai, K. M. Conforti, M. Z. Bazant, Active control of viscous fingering using electric fields, Nat. Commun. 10 (1) (2019) 4002. doi:10.1038/s41467-019-11939-7.

[33] S. Li, J. S. Lowengrub, J. Fontana, P. Palffy-Muhoray, Control of Viscous Fingering Patterns in a Radial Hele-Shaw Cell, Phys. Rev. Lett. 102 (2009) 174501. doi:10.1103/PhysRevLett.102.174501.

[34] Z. Zheng, H. Kim, H. A. Stone, Controlling Viscous Fingering Using Time-Dependent Strategies, Phys. Rev. Lett. 115 (2015) 174501. doi:10.1103/PhysRevLett.115.174501.

[35] O. Borgman, T. Darwent, E. Segre, L. Goehring, R. Holtzman, Immiscible fluid displacement in porous media with spatially correlated particle sizes, Adv. Water Resour. 128 (2019) 158–167. doi:10.1016/j.advwatres.2019.04.015.

[36] D. Saha, R. Bandyopadhyay, Y. M. Joshi, Dynamic Light Scattering Study and DLVO Analysis of Physicochemical Interactions in Colloidal Suspensions of Charged Disks, Langmuir 31 (10) (2015) 3012–3020. doi:10.1021/acs.langmuir.5b00291.

[37] V. Thrithamara Ranganathan, R. Bandyopadhyay, Effects of aging on the yielding behaviour of acid and salt induced Laponite gels, Colloids Surf. A Physicochem. Eng. Asp. 522 (2017) 304–309. doi:10.1016/j.colsurfa.2017.03.006.

[38] A. Shahin, Y. M. Joshi, Physicochemical Effects in Aging Aqueous Laponite Suspensions, Langmuir 28 (44) (2012) 15674–15686. doi:10.1021/la302544y.

[39] C. Talon, L. J. Smith, J. W. Brady, B. A. Lewis, J. R. Copley, D. L. Price, M.-L. Saboungi, Dynamics of Water Molecules in Glucose Solutions, J. Phys. Chem. B 108 (16) (2004) 5120–5126. doi:10.1021/jp035161e.

[40] Y. Lei, H. Li, H. Pan, S. Han, Structures and Hydrogen Bonding Analysis of N,N-Dimethylformamide and N,N-Dimethylformamide – Water Mixtures by Molecular Dynamics Simulations, J. Phys. Chem. A 107 (10) (2003) 1574–1583. doi:10.1021/jp026638+.

[41] C. Misra, V. T. Ranganathan, R. Bandyopadhyay, Influence of medium structure on the physicochemical properties of aging colloidal dispersions investigated using the synthetic clay Laponite®, Soft Matter 17 (2021) 9387–9398. doi:10.1039/D1SM00987G.

# Chapter 6

# Growth kinetics of interfacial patterns formed by the radial displacement of an aging viscoelastic suspension

## 6.1 Introduction

Non-Newtonian viscoelastic fluids exhibit nonlinear rheological responses such as shear-thinning, shear-thickening, and non-zero yield stresses. The mechanical properties of viscoelastic fluids can have a significant effect on the growth kinetics of interfacial patterns generated during their displacement. It has been shown that repeated splitting of the evolving fingers can give rise to ramified structures with dense branching morphologies due to diffusion-controlled interfacial growth [1]. Evolution of patterns with suppressed tip-splitting can be accompanied by an enhancement in the side shedding of branches [2]. The displacement of carboxymethyl cellulose (CMC) solutions by liquid paraffin oil results in a transition from a tip-splitting interfacial pattern to a dendritic pattern as the concentration of the CMC solution is increased [3]. It was reported in this work that shear-thinning effects are maximal

only at the early stages of the displacement process. The observed suppression of instabilities with increase in CMC concentrations was understood by considering the reduction in interfacial tension and the accompanying increase in viscous forces. The displacement of a shear-thinning fluid is driven by a competition between the increased velocity at the tip of the finger and simultaneous finger broadening due to large driving pressures [4]. A study of the displacement of polymeric hydroxypropyl methyl cellulose (HPMC) solutions by air reported a deviation in the finger-tip velocity from the prediction of Darcy's law due to enhanced solution shear-thinning [5]. We have previously proposed that increasing the viscosity ratio of the displacing and displaced fluids and the elasticity of the latter are efficient means of controlling instabilities during displacement of a dense shear-thinning granular cornstarch suspension by a glycerol-water mixture [6]. Despite the low interfacial tension between the two fluids, the patterns displayed limited branching and features such as finger coalescence and proportionate growth during their temporal evolution. Previous studies reported that if the stored elastic energy in the displaced viscoelastic fluids exceeds the fracture energy, then viscoelastic fractures with pointed tips emerge and propagate faster than dendritic patterns [7–10]. The growth and morphologies of interfacial patterns in Hele-Shaw cell geometries are therefore extremely sensitive to the bulk properties of the displaced complex fluid.

In Chapter 5, we showed that the aging time of the displaced colloidal clay suspension, flow rate of the displacing Newtonian fluid and miscibility of the fluid pair are reliable control parameters in the prediction of the global features of the observed interfacial patterns [7]. In addition to the striking structural features of fully-developed patterns, the growth of interfaces is driven by distinct mechanisms that need to be studied systematically [11, 12]. The objective of the present chapter is to characterize the growth kinetics of the distinct morphologies observed at the interface between a Newtonian fluid (displacing fluid) and an aqueous soft glassy colloidal suspension of Laponite clay (displaced suspension) in a radial Hele-Shaw geometry. Our experiments reveal the significant role of interfacial dynamics in de-

termining the distinct morphologies of the fully-developed patterns. The shear and time-dependent rheology of the displaced soft glassy Laponite clay suspension and the wetting property of the displacing Newtonian fluid drive the formation of interfacial patterns with complex spatio-temporal features such as interacting fingers, side branch shedding, fracture propagation, development of interfaces characterized by flower petal-like and jagged shapes, etc. Interestingly, each of the above-mentioned morphologies grows differently. We show here that all the observed morphologies can be uniquely characterized by the time-dependent growth of their areal ratios and the velocities of the tips of the longest fingers. Such predictability of pattern morphologies based on their growth kinetics provides novel opportunities for understanding the formation of complex structures such as river networks [13], dendrites in rechargeable batteries [14]and spherulites [15].

## 6.2 Materials and Methods

The freshly prepared Laponite clay suspension (section 2.2.2 of chapter 2) was first loaded in a radial Hele-Shaw cell (section 2.3.2 in chapter 2) at a gap of 170 $\mu m$, with a syringe pump (NE-8000, New Era Pump Systems, USA) through a 3 mm central hole drilled on the top plate. As described in chapter 5, the aging time $t_w = 0$ corresponds to the time when the loading of the clay suspension was completed. Milli-Q water and mineral oil (Acros Organics) were used as the miscible and immiscible displacing fluids respectively in two different sets of experiments. Further details about experimental and the data analysis protocols can be found in chapter 5.

## 6.3 Results and Discussion

We investigate the growth of interfacial patterns when aqueous Laponite suspensions of concentration 3.25% w/v and at predetermined aging times, 1 h $\leq t_w \leq$ 24 h,

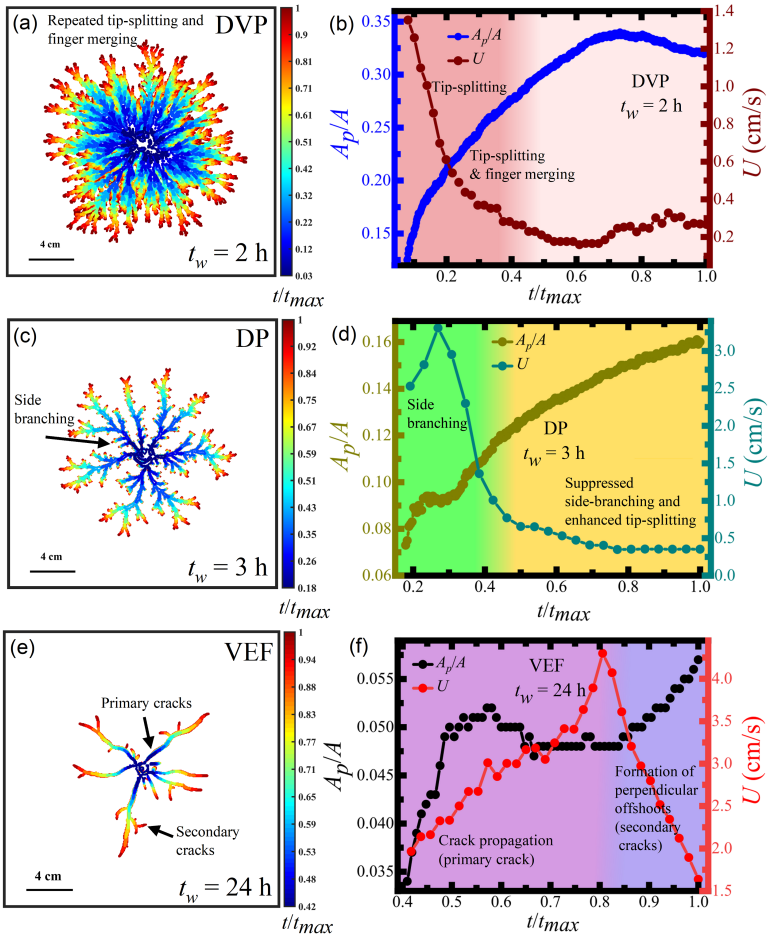



**Fig. 6.1: Temporal evolution of miscible displacement patterns at different suspension aging times.** The miscible (interfacial tension $\sigma = 0$) displacement of 3.25% w/v aqueous Laponite suspensions of different ages by water at a fixed flow rate $q$ = 5ml/min: **(a)** Dense viscous patterns (DVP) at $t_w = 2$ h. The colors in the interfacial pattern in (a), defined by the colorbar on the right, have a one-to-one mapping with the pattern propagation time, normalized by the total experimental time $t_{max}$. **(b)** Areal ratio $A_p/A$ and instantaneous finger-tip velocity $U = dR/dt$ as a function of normalized time $t/t_{max}$ for the DVP displayed in (a). Here, $A_p$ is the area of the fully-developed pattern and $A = \pi R^2$ is the area of the smallest circle enclosing the entire pattern. Instantaneous velocity, $U$, is obtained by measuring the time-rate of propagation of the longest finger of length $R$. Transitions in the mechanisms driving the growth of the DVP in (a) are highlighted by different background colors in (b). **(c)** dendritic pattern (DP) at $t_w = 3$ h. **(d)** $A_p/A$ and $U$ vs. $t/t_{max}$ for DP in (c). **(e)** Viscoelastic fractures (VEF) at $t_w = 24$h. **(f)** $A_p/A$ and $U$ vs. $t/t_{max}$ for VEF in (e).

are displaced by miscible and immiscible fluids (water and mineral oil respectively) at various flow rates, $q$. Temporal evolutions of interfacial patterns when Laponite suspensions of various $t_w$ are displaced by miscible water (interfacial tension $\sigma$ =

0) are shown in Fig. 6.1. When a Laponite suspension of low age, $t_w = 2$ h, is displaced by water, we observe that a very large number of fingers propagate radially outward with repeated tip-splitting at initial times, followed by frequent merging with neighboring fingers at later times, as shown in Fig. 6.1(a). The resulting fully grown pattern morphology is identified as a dense viscous pattern (DVP). The colors in the interfacial patterns in Figs. 6.1(a,c,e) have a one-to-one mapping with the time of evolution of the pattern, normalized by the total experimental duration $t_{max}$, as indicated by the colorbars on the right of the figures. Since the Laponite suspension is liquid-like at low ages (Fig. 5.1(b)), the velocity at the base of the finger is large enough to ensure the effective displacement of the suspension, which results in the merging of neighboring fingers. Due to such merging events during the formation of DVP, we observe many tiny irregularly-shaped regions wherein the displaced suspension is trapped. Consequently, a defining feature of DVP is the absence of well-defined interfacial boundaries. Several different interaction mechanisms between fingers, generated by the immiscible displacement of fluids having a significant viscosity contrast, were reported by Jackson *et al.* [16] *via* numerical simulations. We see from our experiments that finger interactions are commonplace even for miscible displacement of a viscoelastic clay suspension at low sample ages. The left y-axis data in Fig. 6.1(b) quantifies the growth of interfacial patterns in terms of the development of their areal ratios $A_p/A$, defined as the area of the fully-developed pattern ($A_p$) normalized by the area of the smallest circle enclosing it ($A = \pi R^2$), and is estimated by following the protocols adopted in the previous chapter 5. The tip-splitting events and the frequent merging of neighboring fingers cause an increase in $A_p/A$ with time, with $A_p/A$ reaching a constant value due to a balance between tip-splitting and finger merging at later times. We also track the propagation of the longest finger-tip of length $R$ and estimate its instantaneous velocity $U = dR/dt$ (Fig. 6.1(b), right y-axis). The plateauing of finger velocity $U$ at later times, as seen in Fig. 6.1(b), reflects steady pattern growth due to a dynamic equilibrium between finger-tip-splitting and merging events. The transition of the

DVP growth kinetics from tip-splitting to a combination of side-branch shedding and tip-splitting, and eventually to steady growth at later times is highlighted by different colors in Fig. 6.1(b).

The merging between neighbouring fingers is suppressed during the displacement of Laponite suspensions of intermediate ages ($t_w$ = 3 h, 5 h). We note the emergence of side-branching as a dominant propagation mechanism under these conditions. In contrast to DVP, the number of propagating fingers is far smaller in the dendritic pattern (DP) displayed in Fig. 6.1(c). DP growth is characterized by frequent side-branching at early times. This is in agreement with previous experiments on the displacement of shear-thinning carboxymethyl cellulose (CMC) solution by liquid paraffin oil. In this work, it was demonstrated that the local shear rates at the finger-tips achieved a constant magnitude after a certain time, such that shear-thinning of the displaced fluid affects pattern growth only during the early stages of pattern formation [3]. Furthermore, nonlinear simulations [4] showed that local shear-thinning of the displaced fluid at the propagating finger-tips and the simultaneous broadening of the finger behind the tips due to the imposition of high driving pressures contribute to the formation of side branches. We note from Figs. 6.1(c-d) that shear-thinning-induced side-branching of the DP morphology is suppressed at later times and pattern formation is characterized by some tip-splitting events and an eventual steady growth. Figure 6.1(d) shows an abrupt rise in $A_p/A$ at initial times, followed by a comparatively slower increase. This, in combination with the constant finger-tip velocity $U$ at later times during the growth of DP, indicates that side-branching is prominent only during the beginning of the experiment, with steady growth taking over thereafter. On further increasing the aging time of the Laponite suspension to $t_w$ = 24 h, we note that the emergent elasticity of the suspension dominates the development of the growing interface during its displacement. When the driving pressure is large enough that the stored elastic energy is exceeded by the fracture energy, viscoelastic fractures (VEF, Fig. 6.1(e)) emerge. We observe that multiple tip-splitting is absent during the growth of VEF and the total number

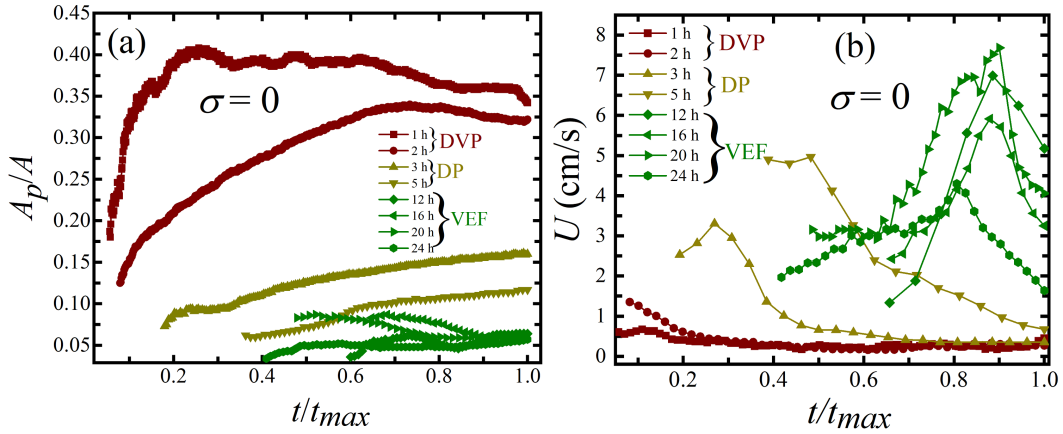



**Fig. 6.2: Areal ratios and instantaneous velocities of miscible patterns with suspension aging time $t_w$ as a control parameter.** **(a)** $A_p/A$ as a function of pattern propagation time $t$, normalized by the total experimental time $t_{max}$, for miscible (interfacial tension $\sigma = 0$) patterns observed during the displacement of 3.25% w/v aqueous Laponite suspensions of different ages by water at a fixed flow rate $q = 5$ml/min. Here, $A_p$ is the area of the fully-developed pattern and $A = \pi R^2$ is the area of the smallest circle enclosing the entire pattern. **(b)** Instantaneous velocity $U$ vs. $t/t_{max}$ for different aging times $t_w$.

of fingers is minimal when compared to DVP and DP (Figs. 6.1(a-d)). VEF emerge with primary cracks at initial times, followed by the formation of secondary cracks at later times due to the release of large tensile stresses. The secondary cracks form approximately perpendicular to the primary cracks, which is a defining characteristic feature of a viscoelastic fracture [8]. Unlike DVP and DP, $A_p/A$ and $U$ for VEF show an initial sharp increase due to primary cracking (Fig. 6.1(e)). At later times, the occurrence of secondary cracks results in a second sharp increase in $A_p/A$, which is accompanied by a rapid decrease in $U$. Despite an identical flow rate of the displacing fluid in all the experiments discussed so far, VEF propagate faster in comparison to DVP and DP (Figs. 6.1(b,d)) and do not show steady growth at any stage of the experiment (Fig. 6.1(f)). $A_p/A$ and $U$ for miscible displacement experiments at several different aging times are shown in Fig. 6.2. These studies confirm that the morphological features and spatio-temporal growth regimes of the interfacial patterns formed by displacement of aging clay suspensions are robustly dependent on the aging time, $t_w$, of the suspension.

We next study the effects of interfacial tension on the immiscible displacement of aging Laponite suspensions by changing the displacing Newtonian fluid from miscible water to immiscible mineral oil ($\sigma \neq 0$, Fig. 6.3). The inclusion of interfacial tension induces flow stabilization by reducing the occurrence of tip-splitting events. At a low suspension aging time, $t_w = 1$ h, we observe that the interface between the Laponite suspension and mineral oil is stable at an early stage of pattern growth, with interfacial perturbations appearing in the form of thick finger-like protrusions only at later times. Since these patterns, such as the one displayed in Fig. 6.3(a), bear a resemblance to flower petals, we call them flower patterns (FP). The sta-

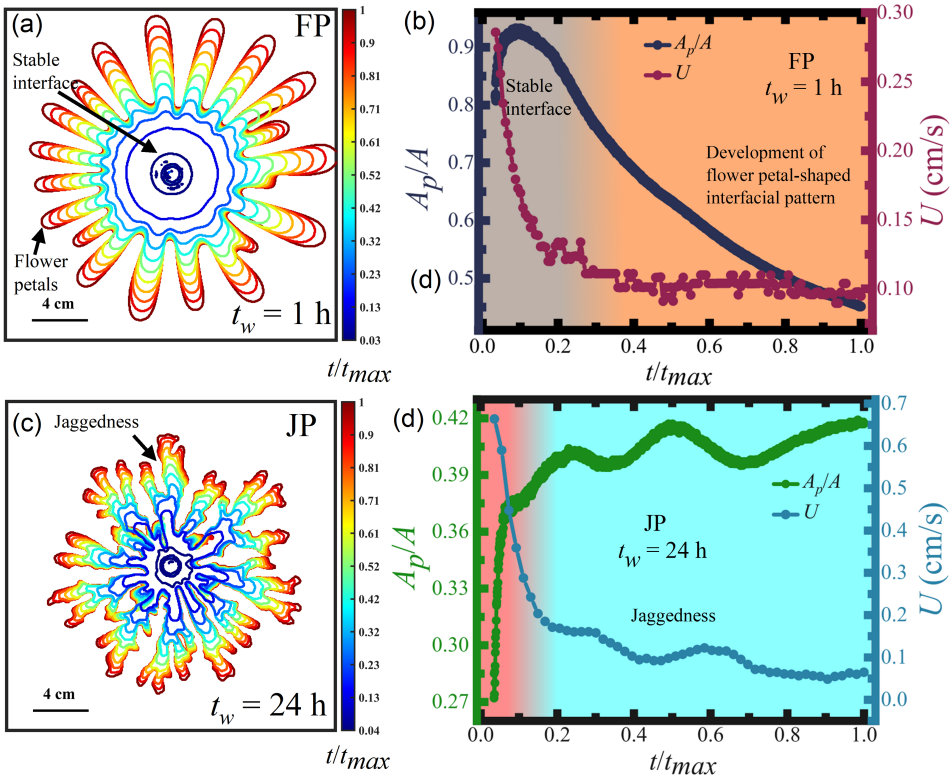



**Fig. 6.3: Temporal evolution of immiscible displacement patterns at various suspension aging times.** The immiscible (interfacial tension $\sigma \neq 0$) displacement of 3.25% w/v aqueous Laponite suspensions of different ages by mineral oil at a fixed flow rate $q = 5$ml/min. **(a)** Flower pattern (FP) at $t_w = 1$ h. The colors in the interfacial pattern in (a), defined by the colorbar on the right, have a one-to-one mapping with the pattern propagation time, normalized by the total experimental time $t_{max}$. **(b)** $A_p/A$ and instantaneous velocity of the longest finger-tip, $U = dR/dt$, as a function of normalized time $t/t_{max}$ for FP in (a). Different colors in (b) indicate transitions in the growth profile of FP. **(c)** Jagged pattern (JP) at $t_w = 24$ h. **(d)** $A_p/A$ and $U$ vs. $t/t_{max}$ for JP in (c).

ble circular interface at the initial stage of pattern growth results from a delay in onset of instability due to non-zero interfacial tension and resembles observations in previous experiments involving Newtonian fluid pairs [17, 18] and oil-clay suspension interfaces [7]. We note from Fig. 6.3(b) that $A_p/A$ values for FP decrease with time due to the emergence of thick protrusions without tip-splitting. Interestingly, the steady growth of the longest finger-shaped perturbation is evident from the approximately constant values of $U$ during much of the experimental duration. In contrast, when we displace a highly aged Laponite suspension ($t_w = 24$ h) with mineral oil, the evolving patterns are characterized by many more fingers than seen at earlier ages, while even displaying occasional tip-splitting events. The competition between shear-thinning and growth in elasticity of the displaced suspension at high $t_w$ results in jagged patterns (JP, Fig. 6.3(c)). We see from Fig. 6.3(c) that the fingers have unique wavy profiles along the azimuthal direction (shown by a black arrow), which gives rise to jaggedness in the morphology of the evolving pattern. In contrast to flower patterns, $A_p/A$ for the jagged pattern increases due to tip-splitting events during its growth. The instantaneous finger-tip velocity $U$ for JP decreases with time, but shows a striking oscillatory behavior during the later stages of pattern evolution. We believe that the observed waviness in $U$ and $A_p/A$ for the JP arises due to disruption and subsequent reformation [19] of the percolating fragile elastic microstructures in the highly aged displaced clay suspension. Such interfacial jaggedness was first observed during the displacement of foam, an yield stress fluid, by immiscible air, and was believed to arise from the elastic rearrangements of bubbles [20]. $A_p/A$ and $U$ for immiscible patterns, obtained by displacing aging aqueous Laponite suspension at several different aging times, are shown in Fig. 6.4. In summary, the morphologies and growth regimes of interfacial patterns can be completely transformed by tuning the mechanical properties of the displaced suspension and the interfacial tension of the fluid pair.

Figure 6.5 summarizes and segregates the distinct growth mechanisms of the observed pattern morphologies in terms of $U$, the instantaneous velocity of the tip of

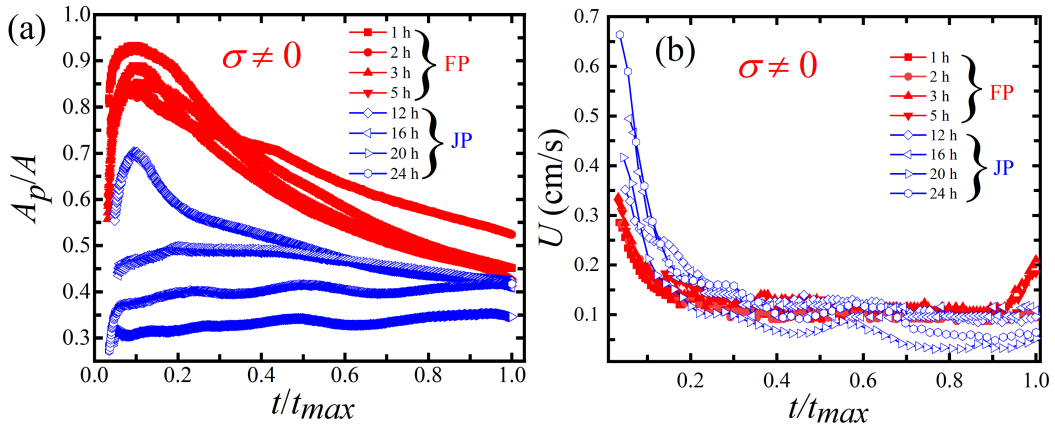



**Fig. 6.4: Areal ratios and instantaneous velocities of immiscible patterns with suspension aging time $t_w$ as a control parameter.** **(a)** $A_p/A$ as a function of pattern evolution time $t$, normalized by with total experimental time $t_{max}$, for immiscible (interfacial tension $\sigma = 0$) patterns observed during the displacement of 3.25% w/v aqueous Laponite suspensions of different ages by mineral oil at a fixed flow rate $q$ = 5ml/min. **(b)** Instantaneous velocity $U$ vs. $t/t_{max}$ for different aging times $t_w$.

the longest finger. Interfacial tension stabilizes the interface and results in patterns that propagate at very low velocities, while developing petal-like and, subsequently, jagged morphologies as the displaced Laponite suspension becomes more elastic with age (Fig. 6.3). In the absence of interfacial tension, the formation of sharp tips costs less energy. Depending on the elasticity, and therefore the aging time, $t_w$, of the displaced clay suspension, we note the growth of miscible patterns characterized by tip-splitting, frequent merging between fingers, side-branching and cracking. Despite the fact that the flow rate of the displacing fluid was kept constant in the above experiments, cracks are seen to propagate the fastest when compared to all other interfacial pattern morphologies. The flow properties of aging Laponite suspensions change dramatically when sheared, particularly at very high suspension aging times [7, 21, 22]. We have therefore also studied the temporal evolutions of interfacial patterns when a highly aged Laponite suspension of $t_w$ = 24 h, is displaced by a Newtonian fluid at various flow rates, $q$. We had previously shown in chapter 5 that the displacement of Laponite suspensions of progressively higher ages, $t_w$, and therefore of higher elasticities, $G'$, can produce the same sequence of

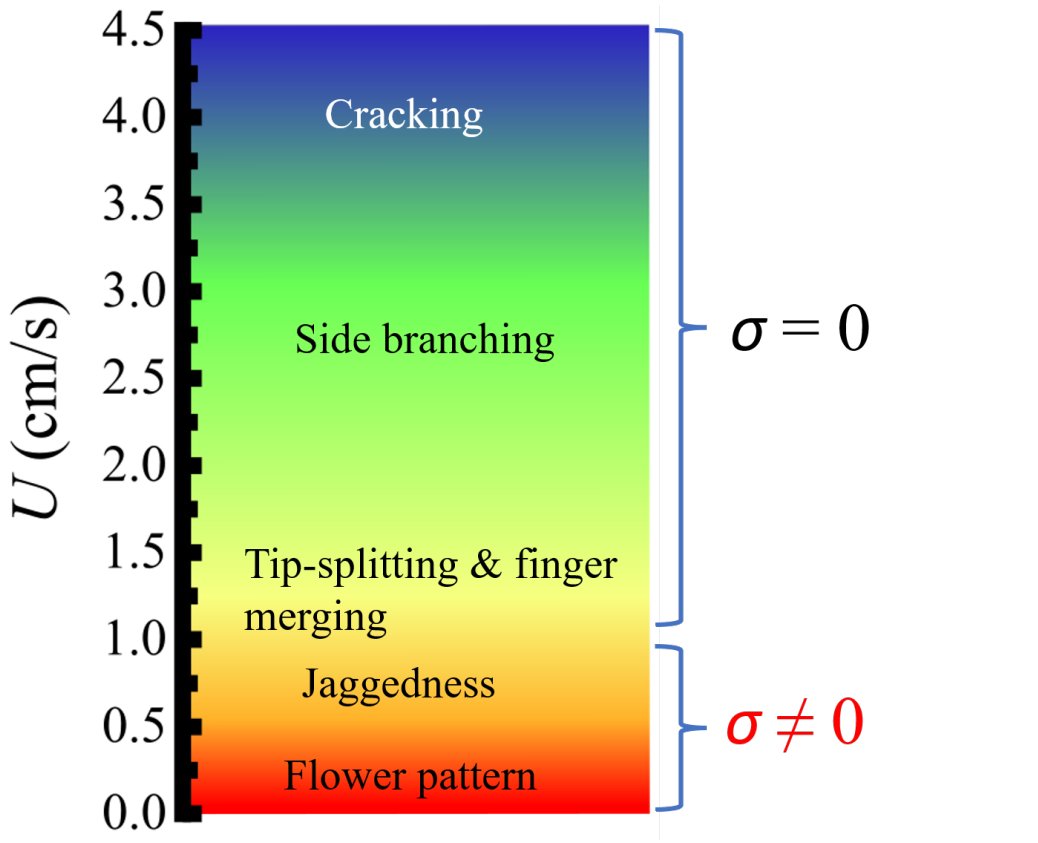



**Fig. 6.5: Distinct mechanisms of pattern evolution depend on the velocity of the longest finger-tip, $U$.** The different interfacial pattern morphologies can be characterized and segregated by considering only the interfacial tension $\sigma$ and $U$.

interfacial patterns that are obtained by decreasing the injection flow rate of the displacing fluid, $q$ [7].

Figure 6.6(a-c) shows the temporal evolution of interfacial patterns that form when an aqueous Laponite suspension of fixed age $t_w = 24$h is displaced by water at various flow rates $q$. For miscible displacement experiments at low flow rates, the pattern morphologies lie in viscoelastic fracturing (VEF) regime (Figs. 6.6(a-b)). As the flow rate is increased, pattern growth is dominated by multiple tip-splitting events, and dendritic patterns (DP, Fig. 6.6(c)) are seen to evolve resembling those seen in Fig. 6.1(c). As in these experiments, we note that even for immiscible displacements, increasing injection flow rates of the displacing fluid results in the same pattern morphologies (Figs. 6.6(d-f)) that are observed by displacing Laponite

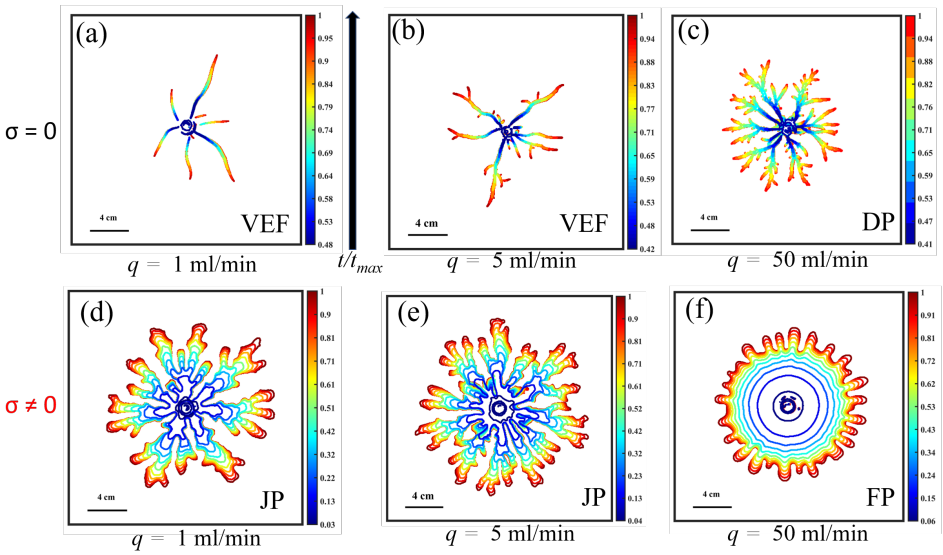



**Fig. 6.6: Temporal evolution of interfacial patterns for different flow rates $q$ of the displacing Newtonian fluid.** Miscible (interfacial tension $\sigma = 0$) displacement of 3.25 % w/v aqueous Laponite suspensions ($t_w = 24$ h) by water at different flow rates: **(a,b)** Viscoelastic fractures (VEF) and **(c)** dendritic pattern (DP). The colorbars map the normalized times $t/t_{max}$, where $t_{max}$ is the total experimental time. Immiscible ($\sigma \neq 0$) displacement of an aqueous Laponite suspension ($t_w = 24$ h) of concentration 3.25% w/v by mineral oil under similar conditions: **(d,e)** jagged pattern (JP) and **(f)** flower pattern (FP).

suspensions of lower $t_w$ at a fixed flow rate (Figs. 6.3(a,c)).

The pattern growth is quantified in terms of the pattern areal ratio $A_p/A$ and longest finger-tip velocity $U$. The variations in $A_p/A$ (Fig. 6.7(a)) of miscible displacement patterns are similar to the earlier experiments at different suspension aging times, $t_w$ (Fig. 6.2(a)). The simple inverse correlation between $t_w$ of the displaced suspension and $q$ of the displacing fluid is further confirmed by comparing the similar variations in the instantaneous finger-tip velocities, $U$, in Fig. 6.7(b) and 6.2(b). The non-monotonic variation in the finger-tip velocity of DP reflects the dominance of shear-thinning effects over elastic effects at high flow rates. We also note that the immiscible jagged patterns (JP) and flower patterns (FP) obtained by increasing $q$ show the same variations in $A_p/A$ (Fig. 6.7(c)) and $U$ (Fig. 6.7(d)) as seen when aqueous Laponite suspensions of lower $t_w$ were displaced by oil (Figs. 6.3(b,d)). The waviness in $U$ of the JP persists even for the experiments with varying flow rates

(Fig. 6.7(d)). Our experiments indicate that desired growth of pattern morphologies can be attained either by changing the aging time, $t_w$, of the Laponite suspensions, the flow rate, $q$, of the displacing Newtonian fluid, or the interfacial tension of the fluid pair. We show here, therefore, that besides controlling the morphological features of fully-developed patterns at the interface between a Newtonian fluid and an aging clay suspension [7], the aging time of the displaced suspension, $t_w$, the shear rate exerted by the displacing fluid, quantified in terms of its flow rate $q$, and the interfacial tension can also reliably predict the temporal evolution of interfacial

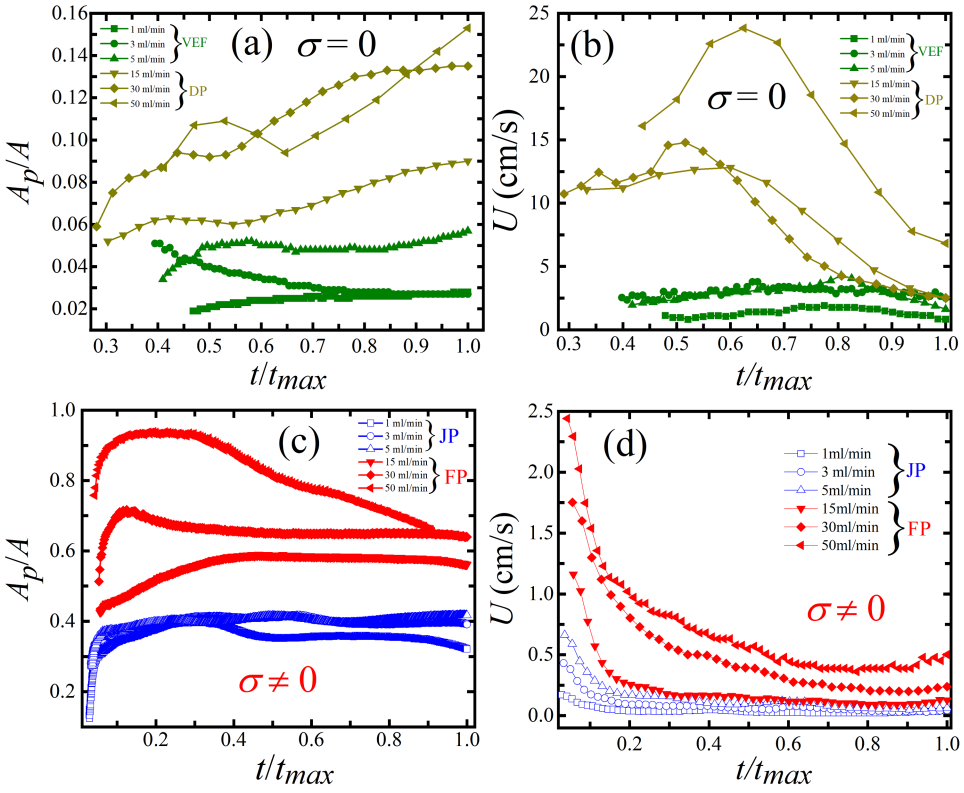



**Fig. 6.7: Areal ratios and finger-tip velocities for miscible (interfacial tension $\sigma = 0$) and immiscible ($\sigma \neq 0$) patterns with flow rate of the displacing fluid, $q$, as a control parameter. (a)** $A_p/A$ as a function of pattern evolution time, normalized with total experimental time $t_{max}$, for miscible (interfacial tension $\sigma = 0$) patterns for different $q$ of the displacing fluid. **(b)** Instantaneous velocity $U$ of the finger-tip of miscible ($\sigma = 0$) interfacial pattern is plotted against normalized time $t/t_{max}$ for different $q$. **(c)** $A_p/A$ as a function of normalized time $t/t_{max}$ for immiscible (interfacial tension $\sigma \neq 0$) displacement patterns for different $q$. **(d)** Instantaneous velocity $U$ vs. time $t/t_{max}$ for immiscible ($\sigma \neq 0$) displacements.

instabilities.

## 6.4 Conclusions

Aging colloidal clay suspensions show spontaneous aging due to the formation of system-percolating fragile microstructures driven by the evolution of electrostatic interactions between the constituent particles [23–25]. In this chapter, we systematically study the growth kinetics of the distinct morphologies observed at the interface between a Newtonian fluid (displacing fluid) and an aqueous soft glassy colloidal suspension (displaced suspension). Dense viscous patterns (DVP) with repeated splitting of the evolving fingers and resembling diffusion-controlled interfacial growth [1], are observed for miscible displacements of clay suspensions of low ages. With increasing age of the displaced clay suspension, patterns with enhanced side shedding of branches are recorded and identified as dendritic patterns (DP) [2–4]. This is followed by emergence of viscoelastic fractures (VEF) for the highest suspension ages [8–10]. We note the development of complex kinetic features during the growth of miscible interfacial patterns, such as repeated tip-splitting and merging of fingers in DVP, side-branching in DP, and crack propagation in VEF. We effectively quantify and distinguish the spatio-temporal growth of the distinct pattern morphologies in terms of their areal ratios and the instantaneous velocities of the tips of the longest propagating fingers. For displacement experiments at non-zero interfacial tension, we observe a delay in onset of instability and an initial stable region in the interfacial pattern when the age of the displaced Laponite suspension is low. This is followed by the emergence of thick protrusions, such that the instability takes the shape of flower petals. This result is reminiscent of earlier experiments involving Newtonian fluid pairs [17, 18]. Furthermore, we observe a jagged interfacial pattern when the elasticity of the displaced suspension is very high. Jaggedness at the interface was also previously observed during the immiscible displacement of an yield stress material (foam) by air [20]. The evolution of the stable central

region in flower patterns and finger-tip-splitting in jagged patterns are reflected in the temporal variations of the tip velocities of the longest fingers and the pattern areal ratios.

To the best of our knowledge, this is the first study that characterizes a wide variety of fully-developed pattern morphologies, generated using miscible and immiscible fluid pairs, in terms of pattern growth kinetics. By systematically measuring and analyzing the evolutions of areal ratios and tip velocities of the longest propagating fingers, we show here that all the distinct interfacial pattern morphologies can be segregated on the basis of their temporal growth. The ability to distinguish interfacial patterns, whether through identification of their fully-developed morphologies, or by the range of growth mechanisms uncovered here, can provide novel opportunities to control the growth of unstable interfaces [26].

To summarise, we show here that it is possible to predict fully-developed interfacial pattern morphologies by studying the different stages of pattern growth. An extension of this work could be a systematic study of interfacial instabilities obtained by displacing a variety of non-Newtonian materials with distinct underlying medium structures and under different physicochemical conditions. Interparticle interactions in charged colloidal clay suspensions, for example, can be altered by changing clay concentration and medium temperature, and by incorporating additives such as salts and acids [27–29]. Such interventions are known to alter the time-dependent rheology of soft glassy clay suspensions [22, 28]. Given the importance of interfaces in fundamental fluid mechanics and in materials processing, for example in the displacement of mud and cement slurries, we believe strongly that our work will trigger further research on the onset and growth of complex interfacial patterns.

# References


[1] E. Ben-Jacob, G. Deutscher, P. Garik, N. D. Goldenfeld, Y. Lareah, Formation of a dense branching morphology in interfacial growth, Phys. Rev. Lett. 57 (1986) 1903–1906. doi:10.1103/PhysRevLett.57.1903.

[2] J. S. Langer, Dendrites, viscous fingers, and the theory of pattern formation, Science 243 (4895) (1989) 1150–1156. doi:10.1126/science.243.4895.1150.

[3] S. Malekian, M. Ahmadlouydarab, R. Najjar, Effects of zero-shear rate viscosity and interfacial tension on immiscible Newtonian-non-Newtonian fluids morphology in radial displacement inside the Hele-Shaw cell, Journal of the Taiwan Institute of Chemical Engineers 127 (2021) 46–55.

[4] L. Kondic, M. J. Shelley, P. Palffy-Muhoray, Non-Newtonian Hele-Shaw Flow and the Saffman-Taylor Instability, Phys. Rev. Lett. 80 (1998) 1433–1436. doi:10.1103/PhysRevLett.80.1433.

[5] M. Kawaguchi, K. Makino, T. Kato, Comparison of viscous fingering patterns in polymer and Newtonian solutions, Physica D: Nonlinear Phenomena 105 (1) (1997) 121–129. doi:https://doi.org/10.1016/S0167-2789(96)00291-6.

[6] Palak, R. Sathyanath, S. K. Kalpathy, R. Bandyopadhyay, Emergent patterns and stable interfaces during radial displacement of a viscoelastic fluid, Colloids Surf. A Physicochem. Eng. Asp. 629 (2021) 127405. doi:https://doi.org/10.1016/j.colsurfa.2021.127405.

[7] Palak, V. R. S. Parmar, D. Saha, R. Bandyopadhyay, Pattern selection in radial displacements of a confined aging viscoelastic fluid, JCIS Open 6 (2022) 100047. doi:https://doi.org/10.1016/j.jciso.2022.100047.

[8] E. Lemaire, P. Levitz, G. Daccord, H. Van Damme, From viscous fingering to viscoelastic fracturing in colloidal fluids, Phys. Rev. Lett. 67 (1991) 2009–2012. doi:10.1103/PhysRevLett.67.2009.

[9] T. Hirata, Fracturing due to fluid intrusion into viscoelastic materials, Phys. Rev. E 57 (1998) 1772–1779. doi:10.1103/PhysRevE.57.1772.

[10] D. Ozturk, M. L. Morgan, B. Sandnes, Flow-to-fracture transition and pattern formation in a discontinuous shear thickening fluid, Commun. Phys. 3 (1) (2020) 1–9. doi:10.1038/s42005-020-0382-7.

[11] X. Cheng, L. Xu, A. Patterson, H. Jaeger, S. Nagel, Towards the zero-surface-tension limit in granular fingering instability, Nat. Phys. 4 (3) (2008) 234–237. doi:10.1038/nphys834.

[12] F. Gallaire, P.-T. Brun, Fluid dynamic instabilities: theory and application to pattern forming in complex media, Philosophical Transactions of the Royal Society A: Mathematical, Physical and Engineering Sciences 375 (2093) (2017) 20160155. doi:10.1098/rsta.2016.0155.

[13] S. Roy, S. Tarafdar, Patterns in the variable Hele-Shaw cell for different viscosity ratios: Similarity to river network geometry, Phys. Rev. E 54 (1996) 6495–6499. doi:10.1103/PhysRevE.54.6495.

[14] W. Xu, J. Wang, F. Ding, X. Chen, E. Nasybulin, Y. Zhang, J.-G. Zhang, Lithium metal anodes for rechargeable batteries, Energy Environ. Sci. 7 (2014) 513–537. doi:10.1039/C3EE40795K.

[15] L. Gránásy, T. Pusztai, G. Tegze, J. A. Warren, J. F. Douglas, Growth and form of spherulites, Phys. Rev. E 72 (2005) 011605. doi:10.1103/PhysRevE.72.011605.

[16] S. J. Jackson, D. Stevens, H. Power, D. Giddings, A boundary element method for the solution of finite mobility ratio immiscible displacement in a Hele-Shaw cell, International Journal for Numerical Methods in Fluids 78 (9) (2015) 521–551. doi:https://doi.org/10.1002/fld.4028.

[17] L. Paterson, Radial fingering in a Hele Shaw cell, J. Fluid Mech. 113 (1981) 513–529. doi:10.1017/S0022112081003613.

[18] I. Bischofberger, R. Ramachandran, S. R. Nagel, An island of stability in a sea of fingers: emergent global features of the viscous-flow instability, Soft Matter 11 (2015) 7428–7432. doi:10.1039/C5SM00943J.

[19] R. Biswas, D. Saha, R. Bandyopadhyay, Quantifying the destructuring of a thixotropic colloidal suspension using falling ball viscometry, Physics of Fluids 33 (1) (2021) 013103. doi:10.1063/5.0035093.

[20] S. S. Park, D. J. Durian, Viscous and elastic fingering instabilities in foam, Phys. Rev. Lett. 72 (1994) 3347–3350. doi:10.1103/PhysRevLett.72.3347.

[21] B. Ruzicka, E. Zaccarelli, A fresh look at the Laponite phase diagram, Soft Matter 7 (4) (2011) 1268–1286. doi:10.1039/C0SM00590H.

[22] C. Misra, V. T. Ranganathan, R. Bandyopadhyay, Influence of medium structure on the physicochemical properties of aging colloidal dispersions investigated using the synthetic clay Laponite®, Soft Matter 17 (2021) 9387–9398. doi:10.1039/D1SM00987G.

[23] S. Ali, R. Bandyopadhyay, Effect of electrolytes on the microstructure and yielding of aqueous dispersions of colloidal clay, Soft Matter 12 (2016) 414–421. doi:10.1039/C5SM01700A.

[24] M. Delhorme, B. Jönsson, C. Labbez, Monte Carlo simulations of a clay inspired model suspension: the role of rim charge, Soft Matter 8 (2012) 9691–9704. doi:10.1039/C2SM25731A.

[25] R. Bandyopadhyay, D. Liang, H. Yardimci, D. A. Sessoms, M. A. Borthwick, S. G. J. Mochrie, J. L. Harden, R. L. Leheny, Evolution of Particle-Scale Dynamics in an Aging Clay Suspension, Phys. Rev. Lett. 93 (2004) 228302. doi:10.1103/PhysRevLett.93.228302.

[26] F. Gallaire, P.-T. Brun, Fluid dynamic instabilities: theory and application to pattern forming in complex media, Philosophical Transactions of the Royal Society A: Mathematical, Physical and Engineering Sciences 375 (2093) (2017) 20160155. doi:10.1098/rsta.2016.0155.

[27] D. Saha, R. Bandyopadhyay, Y. M. Joshi, Dynamic Light Scattering Study and DLVO Analysis of Physicochemical Interactions in Colloidal Suspensions of Charged Disks, Langmuir 31 (10) (2015) 3012–3020. doi:10.1021/acs.langmuir.5b00291.

[28] V. Thrithamara Ranganathan, R. Bandyopadhyay, Effects of aging on the yielding behaviour of acid and salt induced Laponite gels, Colloids Surf. A Physicochem. Eng. Asp. 522 (2017) 304–309. doi:10.1016/j.colsurfa.2017.03.006.

[29] A. Shahin, Y. M. Joshi, Physicochemical Effects in Aging Aqueous Laponite Suspensions, Langmuir 28 (44) (2012) 15674–15686. doi:10.1021/la302544y.

# Chapter 7

# Effects of activity on the dynamics of dense binary mixtures of passive particles

## 7.1 Introduction

Unlike Brownian particles, active particles self-propel by consuming energy from their surroundings and converting them into directed motion [1]. Janus particles are called as such as they have two distinct 'faces' that have distinct physical and chemical properties, for example, different charges, hydrophobicities, fluorescences, and electrical or mechanical properties [2–4]. Janus particles have potential applications as biomarkers, sensors, in the production of water-repellent textiles, in the stabilization of emulsions, etc [5–8]. The microscopic or nanoscopic Janus particles can self-propel with speeds upto a fraction of a millimeter per second [9]. During the last few decades, activity-controlled Janus particles have been increasingly synthesized at a laboratory scale and their dynamics in suspension been studied systematically [9, 10]. Unlike a passive system, a suspension of active particles shows self-clustering and local jamming of the constituent particles [11]. A transition from an aligned phase to a jammed phase of soft active disks with an increase in particle

density was reported in an earlier study [11].

A suspension of passive particles exhibits a kinetically arrested state near a critical volume fraction $\phi_g$ (as discussed in section 1.5). It has been reported that incorporating a small amount of active particles in a suspension of passive particles can result in the formation of dynamic clusters of passive particles surrounded by active particles which eventually melt the local crystalline structures [12]. Previous numerical studies of driven granular media and self-propelled hard sphere systems have reported a shift in the glass transition volume fraction $\phi_g$ to higher values with an increase in the activity [13, 14]. A theoretical study has shown cage breaking in a dense binary mixture of passive particles in the presence of self-propelling active particles [15]. Despite numerous theoretical and numerical studies on activity-induced fluidization of a crowded environment of particles, a systematic experimental study on the effect of activity on the dynamics of passive particles has not been done so far.

This chapter discusses experiments performed with chemically active half platinum coated polystyrene Janus particles which are synthesized in our laboratory. The active Janus particles are added in a controlled way to a dense binary mixture of passive particles. The dynamics of the passive particles are studied under a confocal microscope by increasing the fraction of active particles while keeping the total particle volume fraction constant. The mean square displacements of the passive particles, obtained by video tracking and analyzing passive particle trajectories, indicate fluidization of the kinetically arrested state of the passive particles with increasing activity in the system.

## 7.2 Sample preparation and experimental methods

Chemically active Janus particles are synthesized and the details of the synthesis protocols of these active microspheres are provided in section 2.2.3 of chapter 2.

A bright field microscope (section 2.3.3 in chapter 2) is used to characterize the synthesized Janus particles. A linear microchannel (Fig. 2.8 in chapter 2) is filled with a very dilute stock suspension of Janus PS microspheres using a pipette and is sealed with vacuum grease. The particles are tracked by selecting a disc kernel of equivalent radius in a video spot tracker software developed by Computer Integrated Systems for Microscopy and Manipulation (CISMM). The trajectories of passive and active particles are obtained from their position coordinates in subsequent frames which are analyzed to compute particle mean square displacements (MSD) for characterization of the synthesized active particles.

A binary mixture of passive fluorescent polystyrene (PS) particles ($\phi = 0.57$) is next prepared using small particles (dyed with flash red, Bangs Laboratories Inc.) of diameter $d_S = 2.07 \pm 0.15$ $\mu$m and large particles (dyed with envy green, Bangs Laboratories Inc.) of diameter $d_L = 3.87 \pm 0.15$ $\mu$m. As discussed in section 2.2.4 of chapter 2, a binary mixture of $\phi = 0.57$ is prepared by mixing large and small particles respectively of volumes $V_L = 125$ $\mu$L and $V_S = 25$ $\mu$L respectively. Some of the passive red particles ($d_S = 2.07 \pm 0.15$ $\mu$m) in the prepared binary mixture are replaced by active red particles to produce a hybrid binary mixture of active and passive particles. The volume of the small red particles in the binary mixture is defined as $V_S = V_{PR} + V_{AR}$, where $V_{PR}$ and $V_{AR}$ are the volumes of passive red particles and active red particles respectively. The number of active PS particles in the binary mixture is controlled by systematically changing $V_{AR}$. A 1:1 $D_2O : H_2O$ solution is used for density matching of the polystyrene particles in the mixture. The volume fraction of the binary mixtures is kept fixed for all the experiments. All the prepared binary mixtures are further mixed with 15 $\mu$L of 0.5% $H_2O_2$. These Pt-coated active PS particles in the suspension self-propel in the presence of hydrogen peroxide ($H_2O_2$) due to Pt-induced catalytic decomposition of $H_2O_2$ molecules into water and oxygen molecules [10]. Further details about the preparation of binary mixtures are provided in sections 2.2.4 and 2.2.5 of chapter 2. The prepared binary mixture is loaded in the linear microchannel (Fig. 2.8 in chapter 2) and high reso-

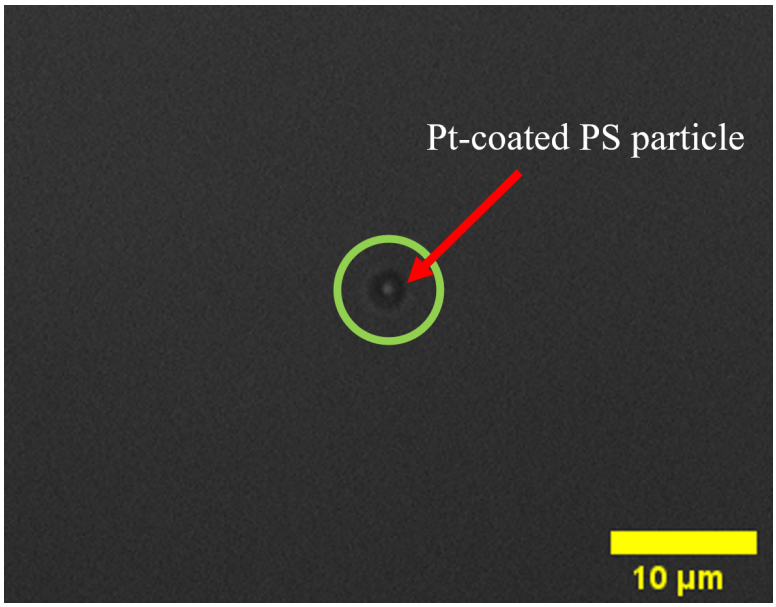



**Fig. 7.1:** A bright field microscopy image of a Pt-coated polystyrene (PS) particle of diameter 2.07 $\mu$m, inside the green circle marked above. The PS particle, suspended in an aqueous 0.5 % hydrogen peroxide ($H_2O_2$) solution, self-propels and shows active Brownian dynamics. The dynamics of the particle is analyzed by computing its mean square displacements (MSD) with time.

lution images are obtained using a confocal microscope (section 2.3.4 in chapter 2). The green (all passive) particles are tracked using CISMM software and mean square displacements (MSD) are estimated.

## 7.3 Results and discussions

Figure 7.1 shows the bright-field image of a single Janus microsphere of size 2.07 $\mu$m suspended in a 0.5 % hydrogen peroxide solution. We acquire high-resolution images using a 40X Leica dry lens (NA = 0.75) at a frame rate $\approx$ 20 fps for 30 s in a bright field microscope. In this work, the evolution of the dynamics of polystyrene particles is observed from their mean square displacements (MSD) which is calculated by tracking individual particle motion. MSD is estimated using the formula $< \Delta r^2(\Delta t) > = < \frac{1}{N} \sum_{i=1}^{N} (\Delta x_i^2(\Delta t) + \Delta y_i^2(\Delta t)) >$. Here, $x$ and $y$ are the position coordinates of the centroids of the particles, $\Delta x$ and $\Delta y$ are the $x$ and $y$ displace-

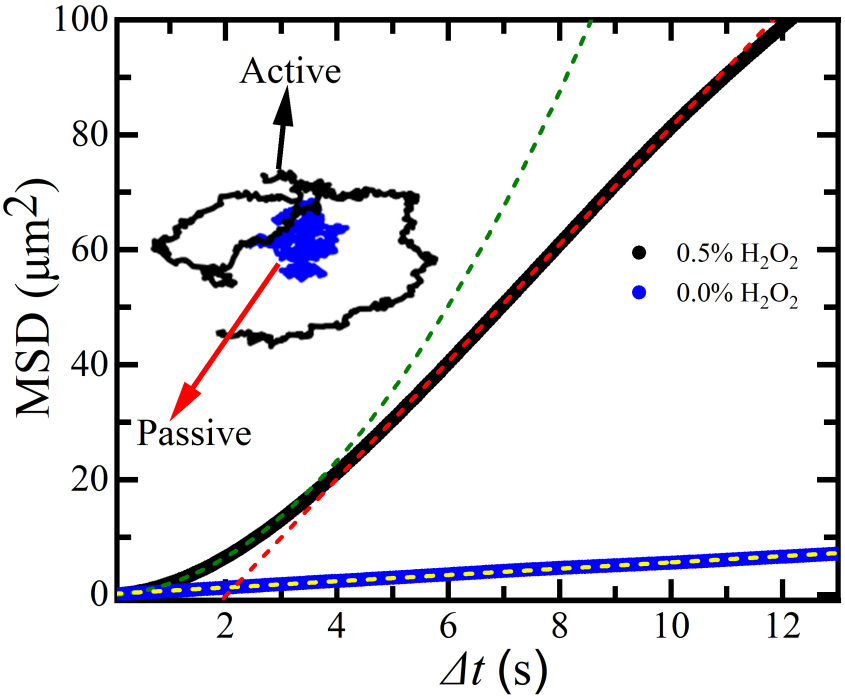



**Fig. 7.2:** MSD of a half-platinum coated PS particle is plotted against lag time $\Delta t$. The inset shows the trajectories obtained by video tracking the particle using a software developed by Computer Integrated Systems for Microscopy and Manipulation (CISMM). The particle suspended in $H_2O_2$ (fuel) self-propels and shows directed motion (shown in black) at early times when compared to the Brownian case (shown in blue) where the suspending medium is water. For the latter case (no fuel), the yellow dashed line is the fit to $\Delta L^2 = 4D\Delta t$ which gives $D = 0.13$ $\mu$m$^2$/s. In the presence of 0.5% fuel, the green dotted line is a fit to $\Delta L^2 = 4D\Delta t + V^2\Delta t^2$ for $\Delta t << \tau_r$ with $D = 0.17$ $\mu$m$^2$/s and $V = 1.13$ $\mu$m/s. The red line is a fit to $\Delta L^2 = (4D + V^2\tau_r)\ \Delta t$ for $\Delta t >> \tau_r$ and yields $D = 1.33$ $\mu$m$^2$/s, $V = 1.52$ $\mu$m/s and $\tau_r = 2.09$ s.

ments of the particles during their $i$ th step, $N$ is the total number of steps with stepping time $\Delta t$ (fixed by the frame rate of 20 fps) and <> is the average over all the particles in the field of view. Figure 7.2 shows the mean square displacement of the single Pt-coated active particle with increasing lag time $\Delta t$ that are obtained by tracking the particle under the bright field microscope over 10 independent videos of 30 s each. While a single Pt-coated polystyrene particle in the presence of $H_2O_2$ fuel exhibits directed motion, a single Pt-coated particle in water shows Brownian motion. The trajectories of the active and passive particles are plotted in black and

blue respectively in the inset of Fig. 7.2. We see from Fig. 7.2 that the MSD of the active particle is very significantly enhanced in the presence of fuel ($H_2O_2$) when compared to the passive (no fuel) case. The diffusion coefficient $D$ of the passive particle is estimated by fitting the MSD (blue circles in Fig. 7.2) with $\Delta L^2 = 4D\Delta t$ (the fit is shown by dashed yellow line) which gives $D = 0.13$ $\mu$m$^2$/s. By following the protocols adopted by Howse *et. al.* [10], the MSD of the active particle (black circles in Fig. 7.2) is fitted to $\Delta L^2 = 4D\Delta t + V^2\Delta t^2$ for $\Delta t << \tau_r$, as shown by green dashed line. The fit yields propulsion velocity, $V = 1.13$ $\mu$m/s and $D = 0.17$ $\mu$m$^2$/s. The red dashed line shows the fit $\Delta L^2 = (4D + V^2\tau_r)\Delta t$ for $\Delta t >> \tau_r$ to MSD and yields $D = 1.33$ $\mu$m$^2$/s, $V = 1.52$ $\mu$m/s and $\tau_r = 2.09$ s. The values of $V$, $D$ and $\tau_r$ are of similar order to the previously determined values for Pt-coated polystyrene microspheres of diameter $1.62 \pm 0.13$ $\mu$m in the presence of $H_2O_2$ [10].

We next measure the mean square displacement (MSD) of passive particles in a

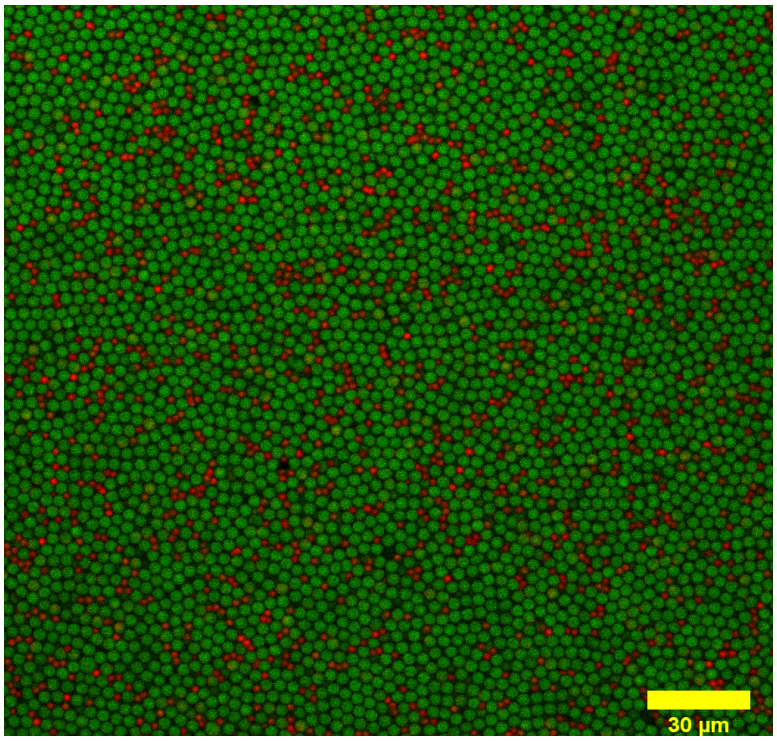



**Fig. 7.3:** A confocal microscopy image of a binary mixture of polystyrene (PS) particles at a volume fraction $\phi = 0.57$. Green circles are polystyrene (PS) particles of diameter $d_L = 3.87$ $\mu$m and red ones are PS particles of diameter $d_S = 2.07$ $\mu$m. All the particles are passive.

dense binary mixture of polystyrene particles. The linear microchannel (Fig. 2.8) is filled with a binary mixture of polystyrene (PS) particles with diameters 3.87 $\mu$m (green) and 2.07 $\mu$m (red) using a pipette and sealed with vacuum grease. A Leica TCS SP8 confocal microscope system with a 40X Leica dry objective (NA = 0.75) is used to acquire high-resolution images of the sample. The images are recorded with a frame rate of 0.68 fps for 300 s. Figure 7.3 shows an image, acquired using confocal microscopy, of a binary mixture of PS particles of total volume fraction $\phi = 0.57$. The volume of the small red particles in the binary mixture is defined as $V_S = V_{PR} + V_{AR}$, where $V_{PR}$ and $V_{AR}$ are the volumes of passive red particles and active red particles respectively. The number of active PS particles in the

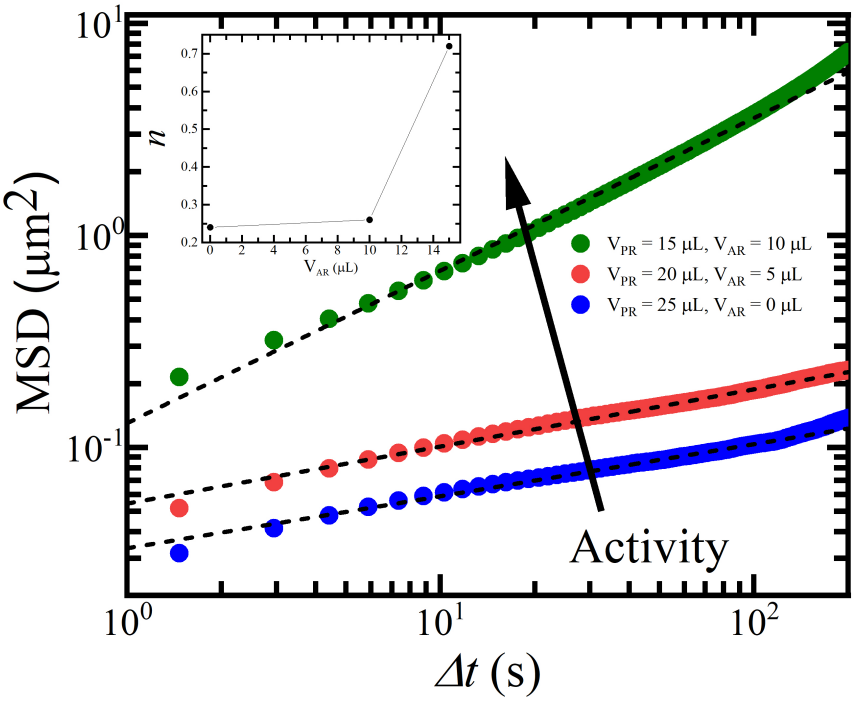



**Fig. 7.4:** MSDs of passive particles are plotted against lag time $\Delta t$. Activity of a suspension is changed by changing the volume of the included active particles, expressed in terms of $V_{AR}$. The volume of the passive particles ($V_{PR}$) is changed appropriately to keep the total volume fraction constant. The particles are suspended in a 1:1 $D_2O : H_2O$ solution with 0.5% $H_2O_2$ (fuel). Black dotted lines are fits of MSDs to a power law of the form $a(\Delta t)^n$. Inset shows the power law exponent $n$, obtained from the fitting.

binary mixture is controlled by systematically changing $V_{AR}$ while keeping the total particle volume fraction and the $H_2O_2$ concentration fixed (which serves as the fuel in driving active dynamics). Fig 7.4 shows the estimated MSDs, $<\Delta r^2(\Delta t)>$, of the passive green PS particles as a function of lag time $\Delta t$ for different $V_{AR}$ in the presence of 0.5% w/v $H_2O_2$, averaged over two different cross sections of the linear microchannel. Here, $V_{AR} = 0$ corresponds to a passive binary mixture wherein no red particle is active. The increase in activity with increasing $V_{AR}$ accelerates the dynamics of passive particles and enhances their MSDs, as shown in Fig 7.4. We increase the active particle concentration by increasing $V_{AR}$ and note that this results in an increase of the average kinetic energy per particle, as indicated by the observed enhancement in the MSD. Increasing $V_{AR}$ leads to increased collisions of the active particles with their neighboring passive particles which results in the breakup of the kinetically arrested state of the passive particles through a cage-breaking mechanism. Black dotted lines are fits of MSDs to a power law of the form $a(\Delta t)^n$. The enhancement in values of power exponent, $n$, with increasing activity reflects the faster dynamics of the passive particles in the presence of increased activity, as shown in the inset of Fig 7.4.

## 7.4 Conclusions

The chapter describes the activity-induced fluidization of a kinetically arrested state of a dense binary mixture of passive particles upon the introduction of enhanced activity. We synthesize chemically active Janus particles by coating platinum Pt on only one hemisphere of the particle. The Pt-coated particles become active in the presence of $H_2O_2$ due to the decomposition of the latter into hydrogen and oxygen molecules. In an active-passive hybrid mixture, we observe the breaking up of cages of passive particles by active particles due to increased collisions between active and passive particles. The mean square displacement of passive particles increases with an increase in the concentration of active particles, while keeping the total

particle volume fraction and the $H_2O_2$ concentration fixed (which serves as the fuel in driving active dynamics). It would be interesting to study the dynamics of passive particles by systematically varying the $H_2O_2$ strength and also by adopting different strategies to change the activity over a much wider range than was accessible in the present experiments. The activity-induced fluidization of a kinetically arrested state is very important from the point of view of biological systems, for example, in cells and tissues where the cytoplasm exhibits characteristic features of glass forming liquids but shows a transition to a liquid-like phase due to activity that is induced by cellular metabolism [16].

# References


[1] S. Ramaswamy, The mechanics and statistics of active matter, Annual Review of Condensed Matter Physics 1 (1) (2010) 323–345. doi:10.1146/annurev-conmatphys-070909-104101.

[2] R. Nakamura, M. Tokuda, T. Suzuki, H. Minami, Preparation of poly(ionic liquid) hollow particles with switchable permeability, Langmuir 32 (10) (2016) 2331–2337. doi:10.1021/acs.langmuir.6b00263.

[3] A. Ghosh, P. Fischer, Controlled propulsion of artificial magnetic nanostructured propellers, Nano Letters 9 (6) (2009) 2243–2245. doi:10.1021/nl900186w.

[4] D. Nishiguchi, M. Sano, Mesoscopic turbulence and local order in janus particles self-propelling under an ac electric field, Phys. Rev. E 92 (2015) 052309. doi:10.1103/PhysRevE.92.052309.

[5] S.-H. Hu, X. Gao, Nanocomposites with spatially separated functionalities for combined imaging and magnetolytic therapy, Journal of the American Chemical Society 132 (21) (2010) 7234–7237. doi:10.1021/ja102489q.

[6] M. Yoshida, K.-H. Roh, S. Mandal, S. Bhaskar, D. Lim, H. Nandivada, X. Deng, J. Lahann, Structurally controlled bio-hybrid materials based on unidirectional association of anisotropic microparticles with human endothelial cells, Advanced Materials 21 (48) 4920–4925. doi:https://doi.org/10.1002/adma.200901971.

[7] B. J. Nelson, I. K. Kaliakatsos, J. J. Abbott, Microrobots for minimally invasive medicine, Annual Review of Biomedical Engineering 12 (1) (2010) 55–85, pMID: 20415589. doi:10.1146/annurev-bioeng-010510-103409.

[8] A. Synytska, R. Khanum, L. Ionov, C. Cherif, C. Bellmann, Water-repellent textile via decorating fibers with amphiphilic janus particles, ACS Applied Materials & Interfaces 3 (4) (2011) 1216–1220. doi:10.1021/am200033u.

[9] C. Bechinger, R. Di Leonardo, H. Löwen, C. Reichhardt, G. Volpe, G. Volpe, Active particles in complex and crowded environments, Rev. Mod. Phys. 88 (2016) 045006. doi:10.1103/RevModPhys.88.045006.

[10] J. R. Howse, R. A. L. Jones, A. J. Ryan, T. Gough, R. Vafabakhsh, R. Golestanian, Self-motile colloidal particles: From directed propulsion to random walk, Phys. Rev. Lett. 99 (2007) 048102. doi:10.1103/PhysRevLett.99.048102.

[11] S. Henkes, Y. Fily, M. C. Marchetti, Active jamming: Self-propelled soft particles at high density, Phys. Rev. E 84 (2011) 040301. doi:10.1103/PhysRevE.84.040301.

[12] F. Kümmel, P. Shabestari, C. Lozano, G. Volpe, C. Bechinger, Formation, compression and surface melting of colloidal clusters by active particles, Soft Matter 11 (2015) 6187–6191. doi:10.1039/C5SM00827A.

[13] W. T. Kranz, M. Sperl, A. Zippelius, Glass transition for driven granular fluids, Phys. Rev. Lett. 104 (2010) 225701. doi:10.1103/PhysRevLett.104.225701.

[14] R. Ni, M. A. C. Stuart, M. Dijkstra, Pushing the glass transition towards random close packing using self-propelled hard spheres, Nature Communications 4 (1) (2013) 2704. doi:10.1038/ncomms3704.

[15] R. Mandal, P. J. Bhuyan, M. Rao, C. Dasgupta, Active fluidization in dense glassy systems, Soft Matter 12 (2016) 6268–6276. doi:10.1039/C5SM02950C.

[16] B. R. Parry, I. V. Surovtsev, M. T. Cabeen, C. S. O'Hern, E. R. Dufresne, C. Jacobs-Wagner, The bacterial cytoplasm has glass-like properties and is fluidized by metabolic activity, Cell 156 (1) (2014) 183–194. doi:10.1016/j.cell.2013.11.028.

# Chapter 8

# Summary and future directions

This chapter summarizes the results reported in the thesis and the scope for future research in this field. This thesis focuses on non-equilibrium flows of soft materials under confinement and in the presence of activity. The interface between two fluids becomes unstable when a more viscous fluid is displaced by a less viscous one, resulting in complex interfacial patterns [1–3]. Complex flow behavior of dense granular suspensions and colloidal suspensions, such as shear-thinning, shear-thickening and aging dynamics, govern the morphologies of interfacial displacement patterns [4–9]. The flow behavior of complex fluids is studied using a rheometer, while interfacial instabilities generated during their displacement are explored in a custom-made radial quasi two-dimensional Hele-Shaw cell. This thesis also describes the influence of activity on the dynamics of passive particles in a crowded environment. A confocal microscope is used to study the dynamics of fluorescent microspheres in the presence of activity.

Chapter 1 contains important background information required to understand the experimental results reported in this thesis. Granular suspensions and their distinct flow regimes are discussed. This is followed by a description of colloidal suspensions and the different interaction mechanisms between the suspended colloidal particles. This chapter also briefly discusses the colloidal glass transition. This is followed by a discussion on the aging dynamics of a soft glassy aqueous suspension

of Laponite clay particles. Next, the formation of interfacial instabilities is outlined. Finally, a short description on the effects of activity on the dynamics of passive particles is provided.

In chapter 2, all the experimental techniques, sample preparation and synthesis protocols used in the thesis are discussed in detail. The preparation of granular and colloidal suspensions is discussed. The synthesis of chemically active Janus particles is next described. Rheology, bright field microscopy, confocal microscopy and a custom-made radial Hele-Shaw cell, used in the thesis to probe the flows of the above mentioned suspensions, are described in this chapter.

Chapter 3 and chapter 4 describe the interfacial instabilities between a granular cornstarch (CS) suspension and miscible Newtonian fluids in the radial Hele-Shaw cell. Aqueous cornstarch suspensions exhibit shear-thinning and shear-thickening behaviors depending on the applied shear stress [10] and particle volume fraction [11]. Chapter 3 discusses the effects of viscosity mismatch between the fluid pair and elasticity of the displaced shear-thinning cornstarch suspension on the morphologies of the observed interfacial patterns. The research in this chapter also proposes methods to enhance the displacement efficiency of the outer fluid. This chapter relates the experimentally obtained average finger spacing to the most dominant wavelength at the onset of instability by performing a linear stability analysis of the interface, wherein the shear-thinning viscoelastic fluid is described by a simplified Carreau model [12]. Our study augments the literature by identifying viscosity and elasticity regimes over which fingering patterns, finger coalescence and stable interfaces will exist for displacement experiments involving Newtonian-non-Newtonian fluid pairs.

We next explore the effect of the shear-thickening behavior of a cornstarch suspension on its displacement by miscible water in chapter 4. Besides monitoring the generation of viscous fingers at the inner interface between water and the CS suspension, we observe an unexpected growth of transient reverse fingers at the outer interface between the CS suspension and air at sufficiently high injection flow rates.

We note that the emergence of elasticity and anisotropic force chain networks in the dense cornstarch suspension plays a significant role in determining interfacial growth in our displacement experiments. The anisotropic stress profiles that are generated in the shear-thickening CS suspension lead to the emergence of these reverse fingers at the outer interface. The formation of reverse fingers at the outer interface significantly decreases the displacement efficiency of material transport. We measure the first normal stress difference of the cornstarch suspension using a rheometer at a gap width that is comparable to that in the Hele-Shaw experiment. We report that the observed large normal stress values, believed to arise due to the formation of contact force chain networks in the suspension, are closely related to the occurrence of reverse fingers in our displacement experiments. Since our results verify the important contribution of normal stresses in pattern formation during the displacement of viscoelastic suspensions in confined geometries, it would be interesting to study displacements of complex fluids such as emulsions [13] and polymeric solutions [14], where magnitude of the normal stresses strongly depends on their individual internal microstructures. In future, a thorough investigation of the relation between normal stresses, sample microstructures and morphologies of interfacial displacement patterns can be performed with different materials and externally imposed shear profiles.

The role of shear and time-dependent rheology of a suspension in governing the interfacial pattern morphologies is discussed in chapters 5-6. Chapter 5 reports a systematic study of interfacial pattern selection by radially displacing an aging soft glassy aqueous clay suspension with miscible and immiscible Newtonian fluids in confined geometry. For both miscible and immiscible displacements, we understand the transitions between the observed interfacial patterns by considering the competition between interfacial, elastic and viscous forces in the aging and shear-thinning clay suspension. We note that instabilities driven by viscous forces result in interfacial patterns characterized by tip-splitting, side branches, and thick protrusions resembling flower petals. In contrast, if elastic forces dominate due to the

spontaneous formation of suspension microstructures [15–17], we observe viscoelastic fracturing or jagged interfaces. Our work supplements the existing experimental literature on clay suspension displacements [18–20] by identifying the suspension aging time $t_w$, which is closely correlated with suspension elasticity, as a new control parameter that reliably determines interfacial pattern morphologies. This work demonstrates that the natural logarithms of the areal ratios can effectively distinguish pattern morphologies on a three-dimensional phase diagram. This result can have far-reaching ramifications in controlling and predicting pattern morphologies between a fluid pair with well-characterized physicochemical properties.

In chapter 6, we systematically study the growth kinetics of distinct morphologies observed at the interface between a Newtonian fluid (displacing fluid) and an aqueous soft glassy colloidal clay suspension (displaced suspension). We quantify the spatio-temporal growth of all the observed patterns by calculating their areal ratios and the instantaneous velocities of the tips of the longest propagating fingers. Due to the complex growth features of the distinct pattern morphologies, such as repeated tip-splitting of evolving fingers and interaction between them in dense viscous patterns, side branching in dendritic patterns, and crack propagation in viscoelastic fractures, we can successfully classify these distinct morphologies on the basis of their temporal growth.

Interparticle electrostatic interactions and therefore the aging dynamics of a charged colloidal clay suspension can be altered in a controlled fashion and their influence on the growth and spatial features of interfacial pattern morphologies can be studied systematically. One research direction could involve the addition of non-dissociating molecules (for example, kosmotropes such as glucose that enhance water structure [21], or chaotropes such as N,N-Dimethylformamide that disrupt hydrogen bonding in water [22]) to the aqueous medium during the preparation of the clay suspension [23]. The presence of additives is expected to alter the aging dynamics and rheology of the suspension, which would strongly influence the interfacial pattern morphologies generated during suspension displacement. For future

research, it would be interesting to systematically study displacement of a variety of non-Newtonian materials with distinct underlying medium structures and under different physicochemical conditions.

Finally, the effects of activity on the dynamics of passive particles in a crowded environment is described in chapter 7. Half-platinum (Pt) coated Janus particles are synthesized. Pt serves as a catalyst when these particles are dispersed in an aqueous hydrogen peroxide $H_2O_2$ solution, decomposing $H_2O_2$ molecules into water and oxygen. The asymmetric distribution of the reaction products around the Janus particles results in their propulsion by the process of self-diffusiophoresis. A small amount of active particles is added in a dense binary mixture of passive particles such that the total volume fraction remains constant. An increase in the concentration of active particles fluidizes the kinetic arrested state of the binary mixture of passive particles. In the future, it would be interesting to study the dynamics of passive particles by systematically varying the $H_2O_2$ strength and also by using other strategies to impart activity to passive particles.

To conclude, this thesis present the non-equilibrium flows of dense suspensions under confinement and in the presence of activity. The influence of shear-dependent viscosities and aging dynamics of dense granular and colloidal suspensions on interfacial dynamics is highlighted using wide variety of experiments. We present different strategies to control the morphologies and growth of fully-developed interfacial patterns. Apart from extending our fundamental knowledge of viscoelastic flows in confined environments, we believe that the work presented in this thesis can also have useful implications in our ability to fine-tune pattern morphologies in non-Newtonian fluid displacements during materials processing. This thesis concludes by demonstrating that a kinetically arrested state of a binary colloidal mixture can be fluidized simply by increasing active particle concentration in the medium.

# References


[1] P. G. Saffman, G. I. Taylor, The penetration of a fluid into a porous medium or Hele-Shaw cell containing a more viscous liquid, Proc. R. Soc. A: Math. Phys. Eng. Sci. 245 (1242) (1958) 312–329. doi:10.1098/rspa.1958.0085.

[2] G. M. Homsy, Viscous Fingering in Porous Media, Annu. Rev. Fluid Mech. 19 (1) (1987) 271–311. doi:10.1146/annurev.fl.19.010187.001415.

[3] A. Pinilla, M. Asuaje, N. Ratkovich, Experimental and computational advances on the study of Viscous Fingering: An umbrella review, Heliyon 7 (7) (2021) e07614. doi:10.1016/j.heliyon.2021.e07614.

[4] N. Kagei, D. Kanie, M. Kawaguchi, Viscous fingering in shear thickening silica suspensions, Phys. Fluids 17 (5) (2005) 054103. doi:10.1063/1.1894407.

[5] P. R. Varges, P. E. Azevedo, B. S. Fonseca, P. R. de Souza Mendes, M. F. Naccache, A. L. Martins, Immiscible liquid-liquid displacement flows in a Hele-Shaw cell including shear thinning effects, Physics of Fluids 32 (1) (2020) 013105. doi:10.1063/1.5133054.

[6] L. Kondic, M. J. Shelley, P. Palffy-Muhoray, Non-Newtonian Hele-Shaw Flow and the Saffman-Taylor Instability, Phys. Rev. Lett. 80 (1998) 1433–1436. doi:10.1103/PhysRevLett.80.1433.

[7] Palak, R. Sathyanath, S. K. Kalpathy, R. Bandyopadhyay, Emergent patterns and stable interfaces during radial displacement of a viscoelastic fluid, Colloids

Surf. A Physicochem. Eng. Asp. 629 (2021) 127405. doi:10.1016/j.colsurfa.2021.127405.

[8] Palak, V. R. S. Parmar, D. Saha, R. Bandyopadhyay, Pattern selection in radial displacements of a confined aging viscoelastic fluid, JCIS Open 6 (2022) 100047. doi:10.1016/j.jciso.2022.100047.

[9] A. Lindner, D. Bonn, J. Meunier, Viscous fingering in a shear-thinning fluid, Phys. Fluids 12 (2) (2000) 256–261. doi:10.1063/1.870303.

[10] I. R. Peters, S. Majumdar, H. M. Jaeger, Direct observation of dynamic shear jamming in dense suspensions, Nature 532 (7598) (2016) 214–217. doi:10.1038/nature17167.

[11] N. J. Wagner, J. F. Brady, Shear thickening in colloidal dispersions, Phys. Today 62 (10) (2009) 27–32. doi:10.1063/1.3248476.

[12] R. B. Bird, C. F. Curtiss, R. C. Armstrong, O. Hassager, Dynamics of Polymeric Liquids, Vol. 2, Wiley, New York, 1987.

[13] V. Labiausse, R. Höhler, S. Cohen-Addad, Shear induced normal stress differences in aqueous foams, J. Rheol. 51 (3) (2007) 479–492. doi:10.1122/1.2715392.

[14] H. Laun, Normal stresses in extremely shear thickening polymer dispersions, J. Non-Newton. Fluid Mech. 54 (1994) 87–108. doi:10.1016/0377-0257(94)80016-2.

[15] S. Ali, R. Bandyopadhyay, Effect of electrolytes on the microstructure and yielding of aqueous dispersions of colloidal clay, Soft Matter 12 (2016) 414–421. doi:10.1039/C5SM01700A.

[16] M. Delhorme, B. Jönsson, C. Labbez, Monte Carlo simulations of a clay inspired model suspension: the role of rim charge, Soft Matter 8 (2012) 9691–9704. doi:10.1039/C2SM25731A.

[17] R. Bandyopadhyay, D. Liang, H. Yardimci, D. A. Sessoms, M. A. Borthwick, S. G. J. Mochrie, J. L. Harden, R. L. Leheny, Evolution of Particle-Scale Dynamics in an Aging Clay Suspension, Phys. Rev. Lett. 93 (2004) 228302. doi:10.1103/PhysRevLett.93.228302.

[18] E. Lemaire, P. Levitz, G. Daccord, H. Van Damme, From viscous fingering to viscoelastic fracturing in colloidal fluids, Phys. Rev. Lett. 67 (1991) 2009–2012. doi:10.1103/PhysRevLett.67.2009.

[19] H. Van Damme, F. Obrecht, P. Levitz, L. Gatineau, C. Laroche, Fractal viscous fingering in clay slurries, Nature 320 (6064) (1986) 731–733. doi:10.1038/320731a0.

[20] H. V. Damme, E. Lemaire, From Flow to Fracture and Fragmentation in Colloidal Media, In: J.C. Charmet, S. Roux, E. Guyon (Eds.), Disorder and Fracture., Springer, Boston, MA, 1990, pp. 83–104. doi:10.1007/978-1-4615-6864-3_6.

[21] C. Talon, L. J. Smith, J. W. Brady, B. A. Lewis, J. R. Copley, D. L. Price, M.-L. Saboungi, Dynamics of Water Molecules in Glucose Solutions, J. Phys. Chem. B 108 (16) (2004) 5120–5126. doi:10.1021/jp035161e.

[22] Y. Lei, H. Li, H. Pan, S. Han, Structures and Hydrogen Bonding Analysis of N,N-Dimethylformamide and N,N-Dimethylformamide – Water Mixtures by Molecular Dynamics Simulations, J. Phys. Chem. A 107 (10) (2003) 1574–1583. doi:10.1021/jp026638+.

[23] C. Misra, V. T. Ranganathan, R. Bandyopadhyay, Influence of medium structure on the physicochemical properties of aging colloidal dispersions investigated using the synthetic clay Laponite®, Soft Matter 17 (2021) 9387–9398. doi:10.1039/D1SM00987G.